SKIN FRICTION AND HEAT TRANSFER PREDICTIONS FOR HYPERSONIC TURBULENT FLOW OVER AN OGIVE-CYLINDER

THESIS

Richard H. Byers

Captain, USAF

AFIT/GAE/ENY/90D-4

DEPARTMENT OF THE AIR FORCE

AIR UNIVERSITY

AIR FORCE INSTITUTE OF TECHNOLOGY

Wright-Patterson Air Force Base, Ohio

AFIT/GAE/ENY/90D-4

SKIN FRICTION AND HEAT TRANSFER PREDICTIONS FOR HYPERSONIC TURBULENT FLOW OVER AN OGIVE-CYLINDER

THESIS

Richard H. Byers

Captain, USAF

AFIT/GAE/ENY/90D-4

AFIT/GAE/ENY/90D-4

SKIN FRICTION AND HEAT TRANSFER PREDICTIONS FOR HYPERSONIC TURBULENT FLOW OVER AN OGIVE-CYLINDER

THESIS

Richard H. Byers

Captain, USAF

AFIT/GAE/ENY/90D-4

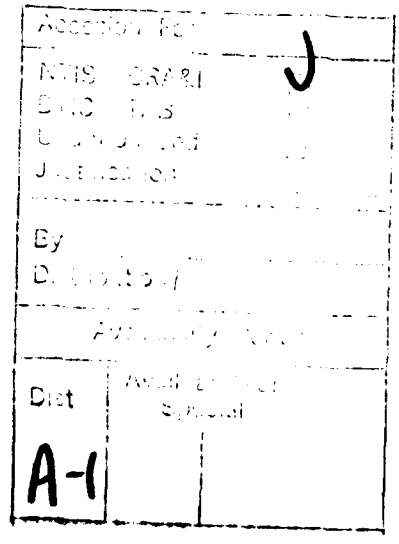

Approved for public release; distribution ulimited

AFIT/GAE/ENY/90D-4

SKIN FRICTION AND HEAT TRANSFER PREDICTIONS FOR HYPERSONIC TURBULENT FLOW OVER AN OGIVE-CYLINDER

THESIS

Presented to the Faculty of the School of Engineering

of the Air Force Institute of Technology

Air University

In Partial Fulfillment of the

Requirements for the Degree of

Master of Science in Aeronautical Engineering

Richard H. Byers, B.A.E.

Captain, USAF

December 1990

Acknowledgements

In the course of completing this thesis, I am indebted to several people for their assistance, encouragement and patience. I wish to thank my thesis advisor, LCol Gerald A. Hasen, for his support and encouragement throughout this effort. It was a joy and an honor to be his student. The success of this project was largely due to the folks in WRDC/FIMG. Capt Lello Galassi provided invaluable technical assistance and was a good friend. Jerry Patterson enthusiastically shared his knowledge of the PNS code with me and answered all of my dumb questions. Dr. Ed Brown-Edwards showed incredible patience as he taught me to use the code and understand my results.

I have personally dedicated my thesis to my friend, Capt Wayne Wilsdon. Although Wayne passed away this summer, he will not be forgotten. His memories will always remain in the minds and hearts of those he befriended, of those lives he touched.

I also owe a tremendous debt of gratitude to my loving wife Janet and my children, Kristi, Timothy and Seth, for their patience and understanding as I struggled through this endeavor. Finally, I wish to thank the Lord Jesus Christ, to whom I owe everything. He was my source of strength and understanding in times of distress. He was always faithful to me.

Richard H. Byers

TABLE OF CONTENTS

LIST OF FIGURES

LIST OF TABLES

LIST OF SYMBOLS

$A+$	effective sublayer thickness constant
C_{cp}	turbulence model constant
C_f	skin friction coefficient
C_{KLEB}	turbulence model constant
c_p	specific heat at constant pressure
C_{wk}	turbulence model constant
D	diameter of ogive-cylinder body
$\underline{E}$	convective flux vector; x-direction
e_t	total energy per unit volume
$\underline{F}$	convective flux vector; y-direction
F_{KLEB}	Klebanoff intermittency factor
F_{max}	maximum value of F(y); Eq (26)
$\underline{G}$	convective flux vector; z-direction
h	convective heat transfer coefficient
j	data plane index
J	transformation matrix Jacobian
k	thermal conductivity, or turbulent mixing length constant
K	Clauser turbulence constant
l	mixing length
L	length of ogive-cylinder body
M	Mach number
P	static pressure
$\underline{P}$	streamwise pressure vector
Pr	Prandtl number

q	heat flux
$\dot{q}$	heat transfer rate
Re	Reynolds number
S	Reynolds analogy factor
$\underline{S}$	viscous flux vector; y-direction
St	Stanton number
T	temperature
u	velocity component; x-direction
U	free-stream velocity
v	velocity component; y-direction
V	free-stream velocity
w	velocity component; z-direction
x	spatial coordinate; streamwise direction
y	spatial coordinate
y+	distance from wall in turbulent shear layer
z	spatial coordinate

Greek

γ	ratio of specific heats
δ	boundary layer thickness
δ^*	boundary layer displacement thickness
ζ	transformed coordinate (z)
η	transformed coordinate (y)
λ	viscosity coefficient
μ	viscosity coefficient
ξ	transformed coordinate; streamwise direction
ρ	density
σ	safety factor

τ	shear stress
ω	fraction of streamwise variable, or vorticity

Subscripts

e	edge of boundary layer
∞	free-stream condition
L	reference to total length
o	reference to stagnation condition
s	surface value
t	turbulent value
w	wall value
x	streamwise direction
ξ	streamwise direction; transformed coordinate

ABSTRACT

The WRDC/FIMG Parabolized Navier-Stokes (PNS) Code is used to numerically predict both laminar and turbulent hypersonic flows over an ogive-cylinder body at zero angle of attack. A parametric study is conducted to determine the effects of selected code input variables on heat transfer and skin friction predictions. Comparisons are made between the PNS predictions and experimental data from the WRDC/Mach 6 High Reynolds Number Test Facility.

Various problems encountered while obtaining PNS starting and marching solutions and corrective steps taken are discussed. A mesh resolution study indicates the minimum radial grid density sufficient for obtaining reasonable heat transfer results. As expected, surface property characteristics are shown to be sensitive to the placement of the first radial grid point away from the surface. Predicted values for surface pressure ratios, local Stanton numbers and local skin friction coefficients are compared with experimental data along the body for laminar through fully developed turbulent flows. Good agreement between the predictions and the experimental data is shown for all flow conditions.

SKIN FRICTION AND HEAT TRANSFER PREDICTIONS FOR HYPERSONIC TURBULENT FLOW OVER AN OGIVE-CYLINDER

I. INTRODUCTION

1.1 Background

Heat transfer and skin friction are two aspects of hypersonic aerodynamics that have a significant impact on the structural requirements and performance of hypersonic flight vehicles. The successful design and evaluation of a hypersonic flight vehicle requires an accurate knowledge of the physics behind heat transfer and skin friction. In the past, this knowledge was gained primarily from wind tunnel tests or captive flight tests. In recent years, however, computational methods have played an increasingly greater role in the investigation of hypersonic aerodynamics and, more specifically, the prediction of heat transfer and skin friction. It is now possible to accurately model the physics of a viscous, hypersonic flow field using a variety of computational methods. One method in particular, the Parabolized Navier-Stokes (PNS) method, has seen widespread use as an efficient tool in the design and evaluation of hypersonic vehicles (1:424).

PNS codes have been used to model supersonic and hypersonic flows over many different body shapes, including pointed cones, cone-cylinders, sphere-cones, blunt biconics, ogive-cylinder-boattails, delta wing configurations, the

Space Shuttle and finned configurations (8:1). The present work is directed towards modeling hypersonic flows over an ogive-cylinder body at zero angle of attack.

There were two primary reasons for conducting this research effort. The first reason was to validate the AFWAL PNS code for flow and geometry conditions similar to conditions anticipated for the National Aerospace Plane. These conditions included hypersonic, viscous flows in the presence of a favorable pressure gradient. The second reason was to show that if the PNS code could accurately predict heat transfer results for the flow conditions and geometry considered, then the predicted results for skin friction should also be accurate. This statement does not imply a Reynolds analogy, but instead asserts that the numerical formulations for heat transfer and skin friction represent good models of the physics involved.

A survey of current literature indicated that PNS codes had been used for ogive-cylinder and ogive-cylinder-boattail geometries in the past (16:4-5), (19:3-6). However, the flow conditions considered in References (16) and (19) were less demanding on the PNS code than the flow conditions required for this effort. The free stream Mach numbers were typically less than three and only Reynolds numbers in the laminar flow regime were considered. The flow conditions planned for this work were thought to pose a serious challenge for the AFWAL PNS code. Although the ogive nose shape is not practical for hypersonic, re-entry type

applications due to stagnation point heating problems, it can provide useful information for other applications. For instance, the ogive nose generates a favorable pressure gradient in the streamwise direction and the National Aerospace Plane will experience this type of flow in some areas over its surface. Also, the ogive nose shape is common to high speed, high performance missiles, such as the Advanced Medium Range Air-to-Air Missile. Current high speed missiles operate at various altitudes and often at speeds greater than Mach 4.

1.2 Objectives

The objectives of this research thesis are as follows:

(1) Obtain PNS solutions for hypersonic flow over the ogive-cylinder body at zero angle of attack. Using the modeling criteria discussed in Chapter 4, obtain the best possible heat transfer and skin friction results along the surface of the body for the range of test conditions considered and independent of the test data.

(2) Identify some of the key input variables and investigate the effects that the input variables have on heat transfer and skin friction results. Use these results to improve the heat transfer and skin friction computations obtained in part (1).

(3) Compare the results obtained from the PNS solutions to actual experimental data for surface pressures, local Stanton numbers and local skin friction coefficients.

The steps taken to meet these objectives are presented

in this research thesis. Throughout the thesis, reference is made to a set of laminar and turbulent flow conditions which are used for discussion of the PNS code results. These flow conditions correspond to test conditions #2 and #5, respectively, as defined in Chapter 5. Chapter 2 presents a discussion of the basic theory involved in the development of the parabolized Navier-Stokes equations, the viscous boundary layer and both heat transfer and skin friction relations. In addition, a discussion of the Baldwin-Lomax turbulence model is included. A general discussion of the AFWAL PNS code and its starting and marching solutions is given in Chapter 3. The discussion includes the definitions of most of the input variables used in the code. Chapter 4 contains the most important numerical results obtained from the nearly 350 starting and marching solutions attempted. Finally, the comparisons between the predicted values and the experimental data are presented in Chapter 5. Chapter 6 contains a summary of recommendations and conclusions with regards to the work performed during this research effort.

II. THEORY

The primary purposes of this section are to identify the governing equations used to solve the hypersonic, viscous flow field and to develop the particular relations necessary for determining heat transfer and skin friction. The full Navier-Stokes equations are simplified for this research effort, since the flow field is almost entirely supersonic and the ogive-cylinder body geometry creates a favorable pressure gradient along the surface of the body. The flow field parameters resulting from the solution of the parabolized Navier-Stokes equations are used to obtain heat transfer and skin friction results.

2.1 The Governing Equations

A simplified set of viscous flow equations, taken from the full Navier-Stokes equations, are identified for use in this effort. Many excellent references, including the texts by Schlichting, Reference 20, and by Anderson, Tannehill and Pletcher, Reference 1, provide a complete development of the full Navier-Stokes equations and the simplifying assumptions used to parabolize them. Parabolizing the Navier-Stokes equations results from 1) neglecting the streamwise viscous diffusion terms and the unsteady terms, and 2) modifying the streamwise convective flux vector to allow stable time-like marching in the streamwise direction. Neglecting the streamwise viscous diffusion terms is reasonable for high Reynolds number flows and situations where body-conforming

coordinates are used. Modification of the streamwise convective flux vector is necessary to render positive eigenvalues from the Jacobian transformation matrix (18:3). These "parabolized" Navier-Stokes equations, from Reference 18, are presented for completeness in a general three dimensional coordinate system, with the x coordinate being in the primary streamwise direction

Continuity:

$$\frac{\partial(\rho u)}{\partial x} + \frac{\partial(\rho v)}{\partial y} + \frac{\partial(\rho w)}{\partial z} = 0 \qquad (1)$$

x Momentum:

$$\rho u\frac{\partial u}{\partial x} + \rho v\frac{\partial u}{\partial y} + \rho w\frac{\partial u}{\partial z} = -\frac{\partial P}{\partial x} + \frac{\partial}{\partial y}\left(\mu\frac{\partial u}{\partial y}\right) + \frac{\partial}{\partial z}\left(\mu\frac{\partial u}{\partial z}\right) \qquad (2)$$

y Momentum:

$$\rho u\frac{\partial v}{\partial x} + \rho v\frac{\partial v}{\partial y} + \rho w\frac{\partial v}{\partial z} = -\frac{\partial P}{\partial y}$$

$$+ \frac{\partial}{\partial y}\left[(\lambda + 2\mu)\frac{\partial v}{\partial y} + \lambda\frac{\partial w}{\partial z}\right] + \frac{\partial}{\partial z}\left[\mu\left(\frac{\partial w}{\partial y} + \frac{\partial v}{\partial z}\right)\right] \qquad (3)$$

z Momentum:

$$\rho u\frac{\partial w}{\partial x} + \rho v\frac{\partial w}{\partial y} + \rho w\frac{\partial w}{\partial z} = -\frac{\partial P}{\partial z}$$

$$+ \frac{\partial}{\partial y}\left[\mu\left(\frac{\partial w}{\partial y} + \frac{\partial v}{\partial z}\right)\right] + \frac{\partial}{\partial z}\left[(\lambda + 2\mu)\frac{\partial w}{\partial z} + \lambda\frac{\partial v}{\partial y}\right] \qquad (4)$$

Energy:

$$\rho u \frac{\partial}{\partial x}\left(e + \frac{V^2}{2}\right) + \rho v \frac{\partial}{\partial y}\left(e + \frac{V^2}{2}\right) + \rho w \frac{\partial}{\partial z}\left(e + \frac{V^2}{2}\right) =$$

$$\rho \dot{q} + \frac{\partial}{\partial y}\left(k \frac{\partial T}{\partial y}\right) + \frac{\partial}{\partial z}\left(k \frac{\partial T}{\partial z}\right) - \left[\frac{\partial (Pu)}{\partial x} + \frac{\partial (Pv)}{\partial y} + \frac{\partial (Pw)}{\partial z}\right]$$

$$+ \frac{\partial}{\partial y}\left[u\mu\left(\frac{\partial u}{\partial y}\right)\right] + \frac{\partial}{\partial z}\left[u\mu\left(\frac{\partial u}{\partial z}\right)\right] + \frac{\partial}{\partial y}\left[v\lambda\left(\frac{\partial v}{\partial y} + \frac{\partial w}{\partial z}\right) + 2v\mu\frac{\partial v}{\partial y}\right]$$

$$+ \frac{\partial}{\partial z}\left[v\mu\left(\frac{\partial w}{\partial y} + \frac{\partial v}{\partial z}\right)\right] + \frac{\partial}{\partial y}\left[w\mu\left(\frac{\partial w}{\partial y} + \frac{\partial v}{\partial z}\right)\right]$$

$$+ \frac{\partial}{\partial z}\left[w\lambda\left(\frac{\partial v}{\partial y} + \frac{\partial w}{\partial z}\right) + 2w\mu\frac{\partial w}{\partial z}\right] \qquad (5)$$

It is necessary to solve Eqs (1) through (5) in order to obtain values for the streamwise velocity component, u, and the temperature distribution, T, in the flow field. However, emphasis is placed primarily on the gradients of velocity and temperature at the surface of the ogive-cylinder. The gradients are key terms in the skin friction and heat transfer relations and they also characterize the thin region of flow near the surface called the boundary layer.

2.2 The Viscous Boundary Layer

A high Reynolds number flow field around an

ogive-cylinder can be divided into two regions: (1) the viscous boundary layer adjacent to the surface and (2) the essentially inviscid region outside of the boundary layer and extending upwards to the shock wave. The velocity of the fluid particles goes from zero (no slip) at the surface to the inviscid flow velocity found between the shock and the boundary layer (4:135). Some fluid particles exit the inviscid flow region when they enter the boundary layer. Due to the viscous nature of the flow, shear stresses in the boundary layer do shearing work on adjacent fluid particles and in turn elevate the local fluid temperature. Temperature variations lead to heat conduction to the body and produce changes in both the fluid viscosity and density. These variations in density and viscosity affect the velocity distribution and, consequently, the shear stress distribution. As a result, skin friction, which depends on shear stress distribution, is partly controlled by heat transfer, which is dependent on temperature distribution. The boundary layer can be described as either a velocity boundary layer, characterized by the presence of velocity gradients and shear stresses, or a thermal boundary layer, where temperature gradients and heat transfer are the dominant features (8:249). Under some circumstances, the profiles describing the two boundary layer types are similar and a relationship can be established between the primary features of each.

2.3 Heat Transfer and Skin Friction

Heat transfer and skin friction are the primary features of velocity and thermal boundary layers. The key ingredient in skin friction is the shear stress at the surface of the ogive-cylinder. The shear stress at the surface is

$$\tau_s = \mu \frac{\partial u}{\partial y}\Big|_{y=0} \tag{6}$$

where $\partial u/\partial y$ is the gradient of velocity and μ is the coefficient of viscosity. The no slip condition is imposed at the surface so that the axial velocity at the wall is zero. As a consequence, energy transfer can only occur by conduction. Heat flux at the surface is given by the Fourier heat conduction equation

$$q_s = -k \frac{\partial T}{\partial y}\Big|_{y=0} \tag{7}$$

where $\partial T/\partial y$ is the gradient of temperature and k is the thermal conductivity. The local skin friction coefficient is defined by

$$C_f \equiv \frac{\tau_s}{\rho_e u_e^2 / 2} \tag{8}$$

where τ_s is determined from Eq (6). The nondimensional form

of the local heat transfer coefficient, the Stanton number, is defined by

$$St = \frac{q_s}{\rho_e u_e c_p (T_w - T_e)} \tag{9}$$

where q_s is determined from Eq (7). For steady flow, an energy balance will be established between the body surface and the convective flow in the boundary layer. The heat transfer at the surface must be identical to the heat transfer convected from the flow, provided that radiation heat transfer is negligible. Eq (7) can be stated as

$$q_s = -k\frac{\partial T}{\partial y}\Big|_{y=0} = h(T_w - T_e) \tag{10}$$

where h is the convective conductance or convective heat transfer coefficient. Eq (9) can be rewritten by substituting Eq (10) in for the value of q_s,

$$St = \frac{h(T_w - T_e)}{\rho_e u_e c_p (T_w - T_e)} = \frac{h}{\rho_e u_e c_p} \tag{11}$$

The Stanton number and the coefficient of skin friction are both nondimensional groupings. Furthermore, the Stanton number is the primary characteristic parameter for the thermal boundary layer just as the skin friction coefficient

is for the velocity boundary layer.

Since both skin friction and heat transfer are dependent upon gradients at the surface, it will be convenient to assume that the gradients are similar at the surface (11:408). Before proceeding, however, it is necessary to define two additional nondimensional groupings, Reynolds number (Re_x), and Prandtl number (Pr),

$$Re_x = \frac{\rho u x}{\mu} \tag{12}$$

$$Pr = \frac{\mu c_p}{k} \tag{13}$$

For a laminar flow, the relationship between heat transfer and skin friction is based on the proportionality between the thermal conductivity, k, and the product of viscosity and specific heat, μc_p, such that $k \propto \mu c_p$. The molecular values of μ and k (from Sutherland's formula) are related through the Prandtl number, Eq (13). Therefore, this proportionality implies the laminar Prandtl number is of order 1. A very important result can be obtained by dividing Eq (9) by Eq (8) to get

$$\frac{St}{C_f/2} = \frac{q_s}{\rho_e u_e c_p (T_w - T_e)} \cdot \frac{\rho_e u_e^2}{\tau_s} \tag{14}$$

$$\frac{St}{C_f/2} = \frac{k \frac{\partial T}{\partial y}}{\rho_e u_e c_p (T_e - T_w)} \cdot \frac{\rho_e u_e^2}{\mu \frac{\partial u}{\partial y}} \qquad (15)$$

$$\frac{St}{C_f/2} = \frac{k}{\mu c_p} \cdot \frac{\frac{\partial T}{\partial y}}{(T_e - T_w)} \cdot \frac{u_e}{\frac{\partial u}{\partial y}} \qquad (16)$$

At a given point in the boundary layer, the gradient of temperature, $\partial T/\partial y$, will be proportional to $(T_w - T_e)$ and the gradient of velocity, $\partial u/\partial y$, will be proportional to u_e. Then, Eq (16) becomes

$$\frac{St}{C_f/2} \propto \frac{k}{\mu c_p} \qquad (17)$$

but it was shown previously that $k \propto \mu c_p$. If $k = \mu c_p$, then Eq (17) yields the familiar Reynolds analogy for laminar flow

$$St \propto C_f/2 \qquad (18)$$

For turbulent flow, a similar analogy can be obtained and will be discussed in the following section. A general form of Reynolds analogy, given by Chi and Spalding Reference 7, is

$$St = S\frac{C_f}{2} \qquad (19)$$

where S is the Reynolds analogy factor. Chi and Spalding determined an empirical value of 1.16 for S based on the best available experimental data for laminar flow over a flat plate (7:430).

By numerically solving the PNS equations, Eqs (1) through (5), the streamwise velocity and temperature can be determined and the skin friction and heat transfer evaluated using Eqs (6) through (9) at points along the surface.

2.4 The Turbulence Model

The skin friction and heat transfer relations developed in the previous section were applicable to a laminar flow. Since turbulent flows were also investigated during this effort, consideration was given to the use of a turbulence model to include the effects of turbulence on skin friction and heat transfer.

Heat transfer and skin friction values for turbulent flows are generally larger than those for laminar flows. This is true because energy is transmitted more readily in a turbulent boundary layer. Also, the gradients of velocity and temperature are much larger at the body surface for a turbulent flow than for a laminar flow. Significant error can result if the laminar form of the PNS equations are solved for a turbulent flow. Consequently, the parabolized

Navier-Stokes equations must be modified to adequately approximate turbulent flows.

The effects of turbulence were chosen in the present effort to be approximated by the Baldwin-Lomax turbulence model. The Baldwin-Lomax model is one of the most popular algebraic eddy viscosity models currently used for hypersonic flows (2:281). An eddy viscosity model is one that approximates the effects of turbulence through an eddy viscosity coefficient, μ_t . This coefficient is substituted in place of the laminar value of μ in the stress terms of the PNS equations (3:1). The Baldwin-Lomax model is also an algebraic model; one that uses just algebraic expressions containing mean flow properties. Although the form of the Baldwin-Lomax model used in this effort is based on characteristic length determinations similar to the widely used Cebici-Smith model, Reference 5, the Baldwin-Lomax model precludes having to explicitly locate the edge of the boundary layer or determine a boundary layer thickness for use as a characteristic length (5:1).

An excellent discussion of the Baldwin-Lomax turbulence model is given in Reference 3. However, to maintain continuity, the basic equations for a two layer model are included here. A two layer model is used to describe the predominantly viscous region immediately adjacent to the surface and the fully turbulent region comprising the remainder of the boundary layer. The inner layer is the viscous region where the momentum and heat transfer can be

accounted for by viscous shear and molecular heat conduction. In the outer, fully turbulent region, momentum and heat transfer are accounted for by using the concept of eddy diffusivity. In each layer, the eddy viscosity coefficient, μ_t, can be defined as

$$\mu_t = \begin{cases} (\mu_t)_{inner} & \text{for } y \leq y_{crossover} \\ (\mu_t)_{outer} & \text{for } y \geq y_{crossover} \end{cases} \quad (20)$$

where y is the local normal distance from the wall and $y_{crossover}$ is the point in the turbulent flow where $(\mu_t)_{inner}$ and $(\mu_t)_{outer}$ have the same value. In the inner region,

$$(\mu_t)_{inner} = \rho l^2 |\omega| \quad (21)$$

where the mixing length l is given by the Van Driest relation

$$l = ky\left[1 - \exp\left(\frac{-y+}{A+}\right)\right] \quad (22)$$

and the vorticity, ω, for a three dimensional flow is

$$|\omega| = \left[\left(\frac{\partial u}{\partial y} - \frac{\partial v}{\partial x}\right)^2 + \left(\frac{\partial v}{\partial z} - \frac{\partial w}{\partial y}\right)^2 + \left(\frac{\partial w}{\partial x} - \frac{\partial y}{\partial z}\right)^2\right]^{1/2} \quad (23)$$

In Eq (22), A+ is an effective sublayer thickness, a dimensionless constant with a value of 26. The other dimensionless constant, k, is the mixing length constant, and has a value of 0.4. Also, y+ is given by

$$y+ = \frac{\rho_w u_\tau y}{\mu_w} = \frac{(\rho_w \tau_w)^{1/2} y}{\mu_w} \qquad (24)$$

In the outer region,

$$(\mu_t) = \rho K C_{cp} F_{WAKE} F_{KLEB} \qquad (25)$$

where K, the Clauser constant, has a value of 0.0168 and $C_{cp} = 1.6$. F_{WAKE} and F_{KLEB} are related to the function

$$F(y) = y|\omega|\left[1 - \exp\left(\frac{-y+}{A+}\right)\right] \qquad (26)$$

such that

$$\begin{cases} & F_{WAKE} = y_{max} F_{max} & (27) \\ \text{or} & \\ & F_{WAKE} = C_{wk} y_{max} u_{DIF}^2 / F_{max} & (28) \end{cases}$$

The value of F_{WAKE} used is the smaller of the expressions given by Eqs (27) and (28). Thus, F_{WAKE} is highly dependent upon the vorticity profile in the outer region, and F_{max} is

dimensionally equivalent to a maximum velocity in the computational plane occurring at y_{max}. The value of C_{wk} = 0.25 and u_{DIF} is given by

$$u_{DIF} = [(u^2 + v^2 + w^2)^{1/2}]_{max} \quad (29)$$

The Klebanoff intermittency factor is given by

$$F_{KLEB}(y) = \left[1 + 5.5\left(\frac{C_{KLEB}y}{y_{max}}\right)^6\right]^{-1} \quad (30)$$

and accounts for the decrease in turbulence at the edge of the boundary layer. In Eq (30), C_{KLEB} has a value of 0.3. The dimensionless, empirically derived constants defined here are also used in the PNS version of the model. These constants have been used successfully for a number of applications over a wide range of flow conditions (19:2), (18:2), (14:8) and (16:3). Once a turbulent eddy viscosity coefficient, μ_t, was computed, it could be related to the turbulent thermal conductivity, k_t, through the turbulent Prandtl number

$$Pr_t = \frac{\mu_t c_p}{k_t} \quad (31)$$

The usual procedure, according to Anderson, Reference 2, is to assume a turbulent Prandtl number, Pr_t = 1. However,

for this effort, $Pr_t = 0.8$ and a laminar Prandtl number of $Pr = 0.72$ was used (19:2), (15). Thus, once μ_t is obtained from the Baldwin-Lomax turbulence model, k_t is obtained from the relation

$$k_t = \frac{\mu_t c_p}{Pr_t} \tag{32}$$

The values obtained for the turbulent eddy viscosity coefficient, μ_t, and the turbulent thermal conductivity, k_t, can be substituted into the parabolized Navier-Stokes equations to adequately model the turbulent hypersonic flow throughout the flow field. Similarly, use was made of Stokes hypothesis such that the coefficient of viscosity, λ, is given by $\lambda = -2\mu/3$. For the turbulent flow case, λ_t was defined by $\lambda_t = -2\mu_t/3$ using the previously determined value of the turbulent eddy viscosity coefficient, μ_t.

III. PARABOLIZED NAVIER-STOKES CODE

3.1 PNS Code Description

The AFWAL Parabolized Navier-Stokes code was used to numerically solve the hypersonic, viscous flow over an ogive-cylinder body. An improved version of the 1983 AFWAL/NASA merged baseline code was supplied by WRDC/FIMG, the High Speed Aero Performance Branch of the Flight Dynamics Laboratory, a component of the Wright Research and Development Center. The improved version has been vectorized for use on the CRAY X-MP Model 216 supercomputer. Several code modifications have been made over the years to improve the code's computational accuracy, efficiency and range of application. The improved PNS code source file was stored on the CDC Cyber 800 series mainframe computer, which served as a front-end device for the CRAY X-MP. Access to the Cyber and the CRAY was provided by WRDC/FIMG and all computer runs were made via telnet using FIMG's Silicon Graphics Iris work stations.

The PNS code required approximately 38 seconds to compile before executing either the starting solution or the marching solution. Binary versions of the PNS source code were obtained and saved on the CRAY itself to make the most efficient use of the expensive CRAY computer time. One binary version was used to run all starting solutions and a second binary version was used for all the marching solutions. Two external files were needed for each solution

case. They consisted of a run file which controlled file disposition and an input file which assigned specific values to the operating variables. For instance, RNBOG was the name of the marching solution run file and OGIVIN was the marching solution input file. RNOGISB was the starting solution run file and OGISBIN was the corresponding input file. Examples of these files can be found in Appendix B.

3.2 PNS Methodology

The methodology employed in the improved PNS code is essentially the same found in other widely-used PNS codes. Parabolizing the Navier-Stokes equations imposes limitations on the application of the PNS code. These simplifications require that the flow be supersonic in the inviscid outer region and that the streamwise velocity component be everywhere positive (1:425). Although stable, time-like marching precludes flow separation in the streamwise direction, crossflow separation can be considered. An ogive-cylinder, subjected to a hypersonic flow, experiences a favorable streamwise pressure gradient downstream of the initial attached bow shock and flow separation is unlikely.

The parabolized Navier-Stokes equations were cast in conservative form and finite difference solutions were obtained by using the Beam-Warming implicit algorithm. The PNS code methodology can, in general, be described as a noniterative, implicit, space-marching, finite difference solution applicable to steady, hypersonic, high Reynolds

number, viscous flows (18:1).

Application of the PNS code to hypersonic, viscous flow over an ogive-cylinder was relatively straightforward, provided the instructions in the user's manual were closely followed. The AFWAL PNS merged baseline code user's manual by Kaul and Chaussee, Reference 9, provided a better explanation of PNS code input variables and operations than did the user's manual for the vectorized version, Reference 21. Significant user preparation was required prior to code execution in order to activate the necessary program options, define the input variables, and quantify the configuration to be simulated.

3.3 Ogive Cylinder Geometry

The configuration selected for modeling in the PNS code was a tangent ogive-cylinder. A tangent ogive-cylinder is one in which the ogive surface and the cylinder surface share a common tangent line at their junction. This results in a smooth, continuous surface with no sharp breaks and one that is slowly varying in the axial direction. The secant ogive-cylinder is an example of a geometry possessing a sharp break or surface slope discontinuity at the junction of the secant-ogive and the cylinder. However, the PNS code is capable of handling discontinuous surface slopes provided that the surfaces themselves vary gradually in the streamwise direction. Physical inputs required to describe the geometry were the body radius, the ogive length and the

overall body length. These inputs were placed in the PNS code to define the body at each axial plane during flow field calculations. The ogive-cylinder described in the PNS code update file was identical to the ogive-cylinder model tested experimentally. Both had a fineness ratio (ogive length/ogive diameter) of 2.33 and an L/D (total length/ogive diameter) of 5.0 corresponding to a diameter of 3.0 inches and a nose length of 7.0 inches. Appendix A contains the derivation of the ogive geometry equations.

3.4 Starting Solution

A starting solution was needed because the marching solution required two initial data planes to march downstream and compute a new data plane of flow field variables. The starting solution provided the two initial data planes. Inherent in the AFWAL PNS code is the capability to internally generate a conical starting solution. However, in order to apply the starting solution to a sharp-nosed body other than a cone, the nose of the body must be approximated with a cone. The ogive-cylinder was modified with a short cone 0.3 inches in length. This modification allowed a viscous conical starting solution to be generated directly from the PNS code.

Unlike the marching solution, the starting solution procedure involves an iterative process between two planes of data. Figure 1 describes the location of the two data planes and the starting solution geometry. The iterative

process involved the following steps. The bow shock was assumed to exist at the angle given by the value of CHI1 and CHI2 have the same value for the ogive-cylinder geometry at zero angle of attack but may be different for other body shapes. The primary flow field variables, ρ, ρu, ρv, ρw, and e, were computed at the j and j-1 planes using the Rankine - Hugoniot equations. The product of ρ and the transformation Jacobian, J, was formed at the same radial location for the j and j-1 planes. The scaled difference given by the expression, $AMAX = [(\rho J)_j - (\rho J)_{j-1}]$, was computed and compared to the somewhat arbitrarily specified tolerance value of 1.0×10^{-5} (14). If the scaled difference was greater than the tolerance, then iterations

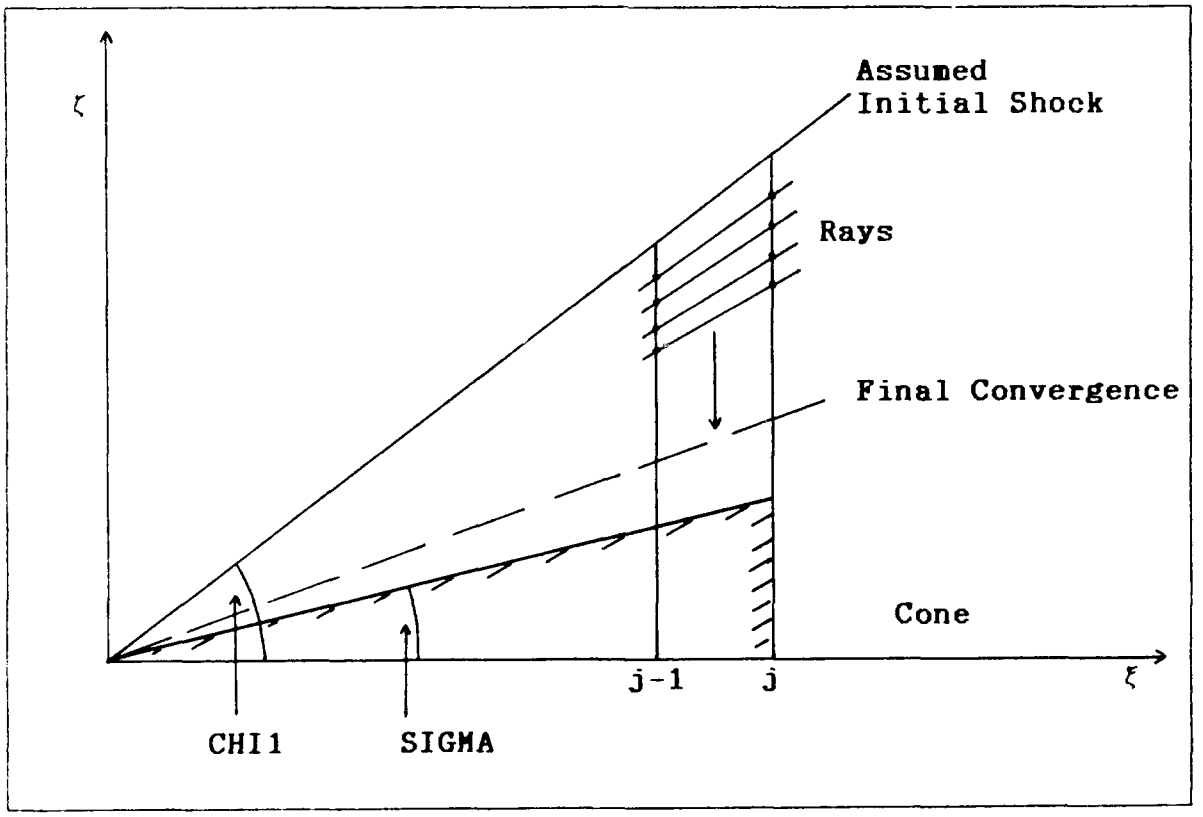

Figure 1. Starting Solution Geometry

continued. The shock location was moved successively closer to the body and the flow field properties were recomputed. While the iterative process was occurring, the viscous layer was gradually growing in thickness above the surface. Eventually, the shock location moved close enough to the viscous layer that conical-like viscous properties were obtained and the scaled difference became smaller than the tolerance. Once this event occurred, the bow shock location was fixed and iterations ceased. Properties along rays were considered to be constant and a converged starting solution was obtained (19:3). Thus, the viscous flow properties computed at the j and j-1 planes during the last iteration were retained for use as initial data planes.

The convergence process can be observed by considering the scaled density difference value, AMAX, at each iteration. Figure 2a shows the variation of AMAX with iteration for a laminar case. Convergence was achieved but not without some difficulty. The figure shows a significant amount of high frequency oscillations that occurred while the solution was converging. High frequency oscillations are a common problem encountered by many numerical techniques employing finite difference algorithms. The oscillational behavior of AMAX, displayed in Figure 2a, suggests that perhaps the shock location might also be oscillating during the iterative process. This possibility was addressed and the results are shown in Figure 2b. The shock location starts at an initial angle of 46 degrees

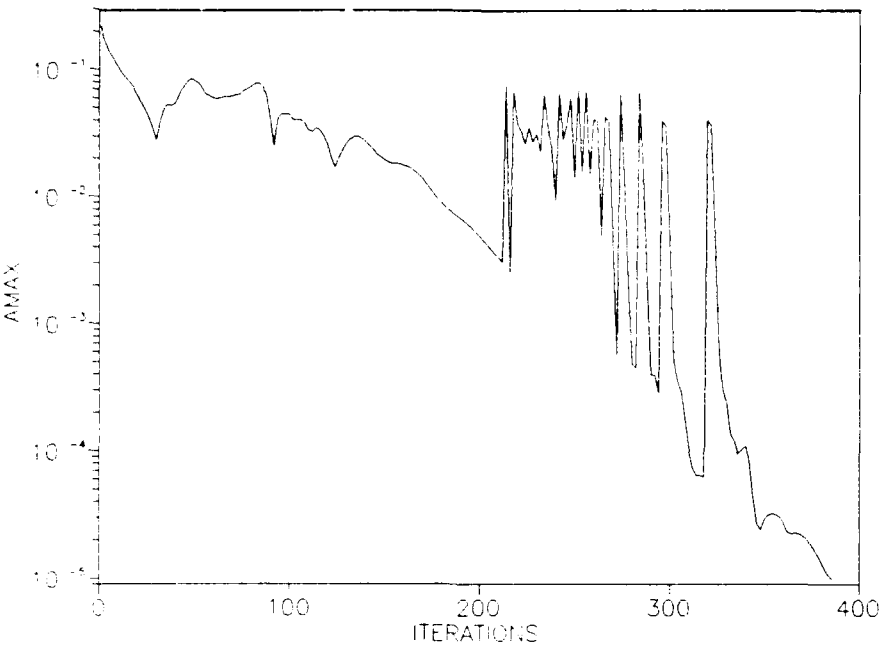

Figure 2a. Starting Solution Convergence - Laminar Case (EPSA = 0.5)

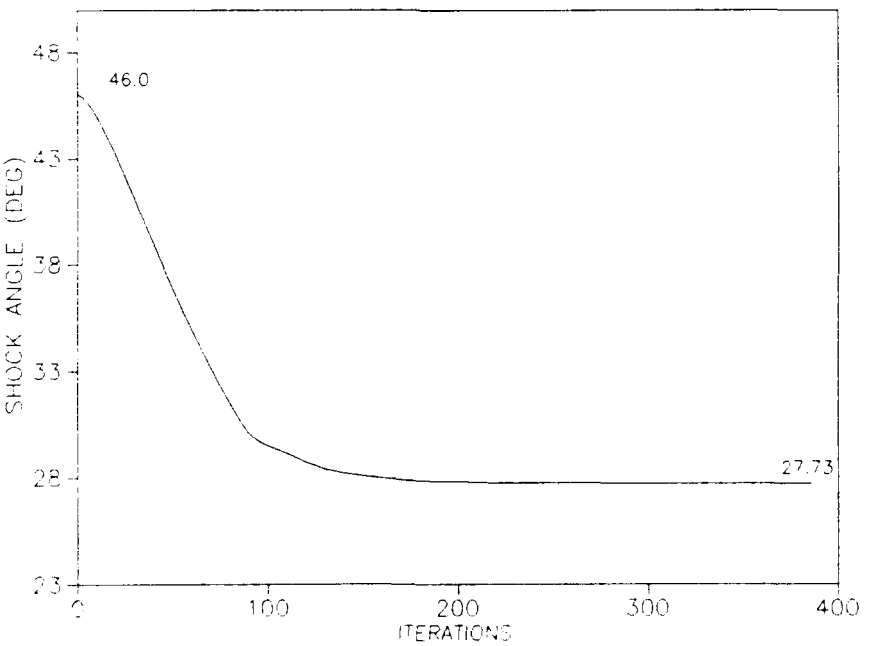

Figure 2b. Conical Shock Convergence - Laminar Case

(CHI1) and decreases smoothly to 95 percent of the final convergence angle after approximately 100 iterations. As can be seen, the final shock angle of 27.73 degrees is obtained in fewer iterations than the convergence criterion. The results shown in Figure 2b indicate that the shock position is not oscillating during the iterative process for the laminar case considered.

It appears that the matrix conditioning parameter, EPSA, has a dampening effect on high frequency oscillations. The solution shown in Figure 2a was obtained with an EPSA value of 0.5. Figure 3 shows the same laminar case run with the a value of EPSA = 1.0 and no other changes. A marked reduction in oscillations occurred. Increasing EPSA may be necessary to get a converged solution for high Reynolds number flows even though a large value has some negative effects. These negative effects will be discussed in Chapter 4.

Figure 4 shows the convergence of a solution for a turbulent case that had a high EPSA value of 1.0 and contains minimal high frequency oscillations. The starting solution obtained for the laminar case shown in Figure 3 required 386 iterations before AMAX reached a value of 9.653×10^{-6}. The turbulent case, Figure 4, required 482 iterations before AMAX descended below tolerance at 9.904×10^{-6}. Obtaining a converged solution proved to be quite a challenge. As a matter of fact, a considerable amount of time and computer resources was spent just trying to obtain

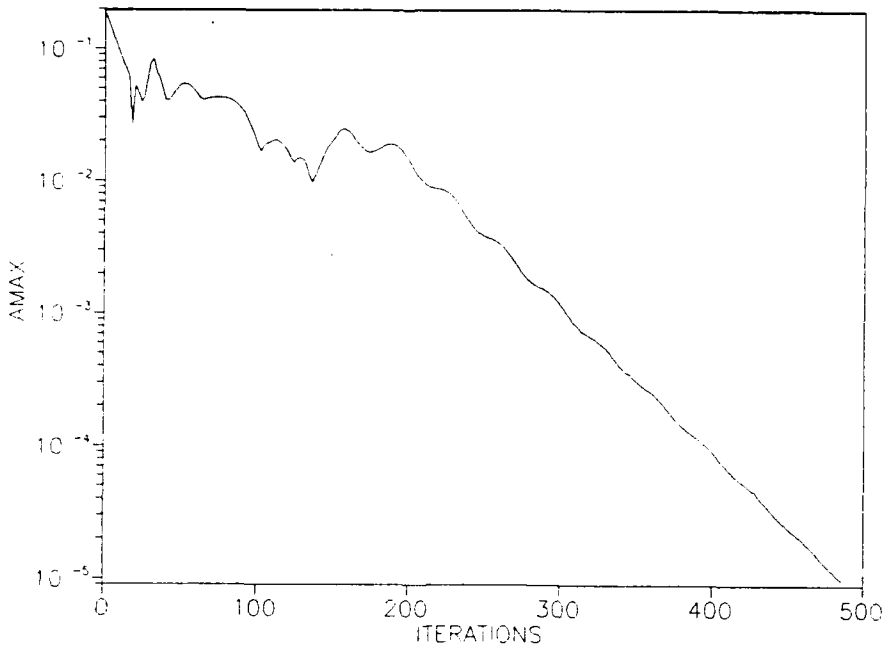

Figure 3. Laminar Starting Solution - EPSA Increased

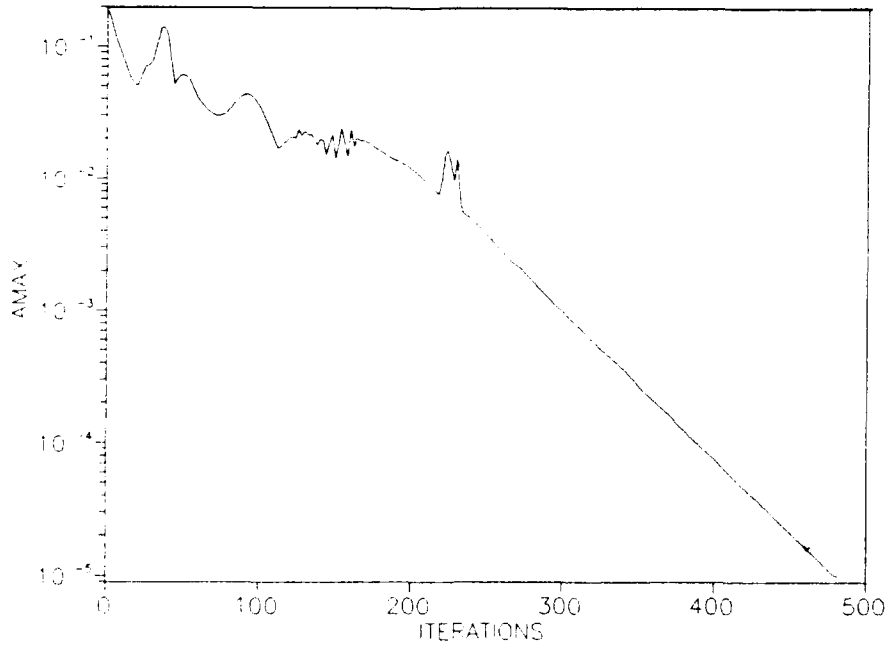

Figure 4. Starting Solution Convergence - Turbulent Case (EPSA = 1.0)

starting solutions for the laminar and the turbulent flows. Many solutions diverged or simply leveled off at an AMAX value between 0.01 and 0.001, far greater than the tolerance value of 0.00001. Simply put, an improper set of input parameters would never converge regardless of how many iterations were allowed. However, persistence and creative "fine-tuning" of the input variables eventually resulted in obtaining converged solutions for all cases. All starting solutions were saved on the Cyber for use as input files for the appropriate marching solution.

3.5 Marching Solution

Execution of the PNS code to obtain a marching solution required that a starting solution be saved to TAPE3. The two planes of data were stored on TAPE3 and were read into the PNS code from Subroutine STRTPL. For the procedure established in the current effort (i.e. in RNBOG), file manipulation required use of the file rename command, SRENAME,file1,file2. For instance, TAPE3 would be renamed as the starting solution OGVRB22 by entering: SRENAME,TAPE3,OGVRB22 while in the Cyber command line. After obtaining the desired output from the marching solution, the procedure would be reversed: SRENAME,OGVRB22,TAPE3. More than one starting solution file was lost by inadvertently renaming TAPE3 with a different starting solution without first saving the original starting solution. With TAPE3 properly defined, the input file for

the marching solution, specified as OGIVIN, could be tailored for a specific test condition.

OGIVIN contains 91 input variables: 41 integer values and 40 real values. These inputs can be grouped into seven categories: 1) flow field conditions, 2) integration parameters, 3) marching parameters, 4) smoothing parameters, 5) geometry definition, 6) output parameters, and 7) force and moment parameters. Since no force and moment data were required, category (7) will be ignored. The input variables, separated into respective groups, are:

Group 1. Flow Field Conditions

ALPHA	Angle of attack (degrees)
BETA	Angle of yaw (degrees)
FSMACH	Free stream Mach number
RE	Free stream Reynolds number (per length)
GAMMA	Flow field specific heat for ideal gas, or Free stream specific heat for real gas
TWALL	Adiabatic or fixed wall temp. (Rankine)
TINF	Free stream temperature (degrees Rankine)
DQINF	Computed or specified free stream dynamic pres.
IREAL	Ideal or real gas solution
INVIS	Inviscid or viscous flow solution

Group 2. Integration Parameters

METHOD	Euler implicit or 3-pt backward difference
IDPDX	Sublayer model: Streamwise pressure gradient ignored, Schiff-Steger model, or Vigneron model.
IHYBRD	Viscous region defined by LBLP or total enthalpy
IPER	Pitch plane symmetry or periodic conditions
ISLIP	Viscous no-slip boundary conditions imposed gradually or immediately
LADD	Viscous sublayer= sonic line grid point + LADD
LBLP	Index on boundary layer edge grid point
XTRANS	Axial location for beginning of transition
ICYL	Cartesian or cylindrical coordinates
ICROSS	Cross-flow viscous option
LAMIN	Turbulence model option

Group 3. Marching Parameters

JS	Index of the first marching step, or the index

	of the first starting solution iteration
JMAX	Maximum number of axial marching steps, or maximum number of iterations
DX	Axial marching step size
CNBR	Step size option: constant or dynamic
NCNBR	Dynamic step size update
ISTEP	Step size scaling option
ISMTH	Dynamic smoothing on SMU and SMUIM
ICONIC	Conic step-back option
Group 4.	Smoothing Parameters
SMU	Explicit smoothing parameter
SMUIM	Implicit smoothing parameter
EPSA	Matrix conditioning parameter
EPSB	Matrix conditioning parameter, EPSB=EPSA
Group 5.	Geometry Definition
	(Size)
KMAX	Number of points in circumferential direction
LMAX	Number of points in the radial direction
	(Body)
X	Starting plane data, or first axial location
XEND	Last axial location
ZOB	Z origin of body
INCHES	Dimensions are in inches
IBODY	Options for body grid generation
AOVERB	Ellipse ratio (A/B)
SIGMA	Major cone half angle (degrees)
XOB	Axial location of body origin
XOS	Axial location of outer boundary origin
ISEG	Defines the surface to be interpolated
ISPLIN	Linear or spline curve fit of body geometry
	(Grid)
DS	Radial spacing option
IGRID	Grid generator option
METRC	Metric coefficient option
ISTRCH	Radial grid clustering option
PER	% of grid points radially clustered near surface
PERMIN	Lower limit of PER, windward side of body
PERMAX	Upper limit of PER, leeward side of body
DSYPLUS	Maximum value of y+ maintained during marching
IDAPT	Solution adaptive grid option
NPOINT	Option on location of first radial step (DS)
	(Shock)
IFIT	Shock fitting or shock capturing calculation
IRAY	Shock propagation option
CHI1	Outer boundary angle referenced to y axis
CHI2	outer boundary angle referenced to z axis

The input variables for the output parameters and the force and moment parameters, Groups 6 and 7, can be found in

Appendix B. Once OGIVIN inputs have been selected and entered into the input file, the PNS code can be executed to obtain a marching solution. Several of the input variables will be given specific definitions based on flow conditions and grid choices in the following section. A complete listing of all variables for each simulation is also contained in Appendix B.

IV. NUMERICAL MODELING

4.1 The Sublayer Model

One of the two simplifications made to parabolize the Navier-Stokes equations required modifying the streamwise convective flux vector to allow stable time-like marching in the streamwise direction. Contained within the streamwise convective flux vector is a pressure gradient term that allows information to be propagated upstream through the subsonic portion of the boundary layer. During the solution process, subsonic flow encountered near the surface will result in at least one negative eigenvalue from the Jacobian transformation matrix (9:9). Consequently, this negative eigenvalue leads to an ill-posed problem in which exponentially growing errors or departure solutions occur (21:79). Therefore, to obtain stable, time-like marching behavior, it is necessary to modify the streamwise pressure gradient to prevent upstream feedback.

The improved version of the PNS code offers three sublayer models for handling the streamwise pressure gradient. The input variable which reflects the model chosen is IDPDX and IDPDX can have values of 0, 1, or 3. Each value corresponds to a particular sublayer model. For IDPDX = 0, the zero pressure gradient model is selected. This model assumes that a zero streamwise pressure gradient exists in the sublayer region along the surface. This model was not used since the give-cylinder geometry experienced a

non-zero streamwise pressure gradient along the ogive nose. The second model, used when IDPDX = 1, was the Schiff-Steger sublayer model. In this model, the pressure was calculated at the sonic part of the boundary layer and this pressure value was then assumed below the sonic line to the body surface. This is a reasonable assumption based on the fact that for thin, subsonic sublayers, the normal pressure gradient is essentially negligible (14:9). However, due to the pressure interaction between the supersonic and subsonic regions, the Schiff-Steger model does not completely prevent departure solutions from occurring (1:438). The third choice, IDPDX = 3, activates the Vigneron sublayer model. Within this model, a fraction of the streamwise pressure gradient remains in the streamwise momentum equation and the other fraction can either be completely omitted or evaluated explicitly. The pressure gradient splitting technique employed in the Vigneron sublayer model prevents the unstable behavior that ordinarily occurs when the entire pressure gradient is retained in the convective flux vector and evaluated in the subsonic sublayer region.

The Vigneron sublayer model was preferred to the Schiff-Steger model and was used for all numerical simulations. In the Vigneron model, the fraction of the streamwise pressure gradient retained in the streamwise convective flux vector is defined as $\omega(\partial P/\partial x)$. The remaining fraction, given as $(1-\omega)(\partial P/\partial x)$, is evaluated explicitly using a backward - difference formula (16:3).

This splitting technique can be better described by considering the vector representation of the PNS equations, assuming perfect gas and constant viscosity, such that

$$\frac{\partial \underline{E}}{\partial x} + \frac{\partial \underline{F}}{\partial y} + \frac{\partial \underline{G}}{\partial z} = \frac{\partial \underline{S}}{\partial y} \tag{33}$$

where $\underline{E}$, $\underline{F}$, and $\underline{G}$ are the convective flux vectors and $\underline{S}$ is the viscous flux vector. The streamwise convective flux vector, $\underline{E}$, is given by

$$\underline{E} = \begin{bmatrix} \rho u \\ \rho uu + P \\ \rho uv \\ \rho uw \\ (e_t + P)u \end{bmatrix} \tag{34}$$

Eq (33) can be rewritten to reflect the pressure gradient splitting technique as

$$\frac{\partial \underline{E}}{\partial x} + \frac{\partial \underline{P}}{\partial x} + \frac{\partial \underline{F}}{\partial y} + \frac{\partial \underline{G}}{\partial z} = \frac{\partial \underline{S}}{\partial y} \tag{35}$$

where the streamwise flux vector and streamwise pressure vector are defined as

$$\underline{E} = \begin{bmatrix} \rho u \\ \rho uu + \omega P \\ \rho uv \\ \rho uw \\ (e_t + P)u \end{bmatrix} \tag{36}$$

$$\underline{P} = \begin{bmatrix} 0 \\ (1-\omega)P \\ 0 \\ 0 \\ 0 \end{bmatrix} \tag{37}$$

A solution to the set of equations represented by Eq (35) results in the formation of a transformation matrix. Stable marching places a restriction on the eigenvalues from the transformation matrix such that all eigenvalues must be real and positive. This restriction can only be satisfied if the streamwise velocity component, u, is always positive and the following condition on ω is met (21:86), (1:439):

$$\omega < \frac{\gamma M_x^2}{1 + (\gamma - 1) M_x^2} \tag{38}$$

where M_x is the local streamwise Mach number. In the computational domain, ξ replaces x as the streamwise coordinate so that Eq (38) can be rewritten as

$$\omega < \frac{\gamma M_\xi^2}{1 + (\gamma - 1) M_\xi^2} \tag{39}$$

and M_ξ is now the local streamwise Mach number in the ξ coordinate. The condition that u always be positive prohibits treatment of reverse flow situations. This should not pose a problem for the ogive-cylinder geometry at zero

angle of attack since a favorable streamwise pressure gradient exists along the ogive nose and the flow is accelerating in the streamwise direction. Furthermore, the flow over the cylindrical part of the body behaves much like the flow over a flat plate in which case the favorable pressure gradient gradually approaches a zero pressure gradient. Regardless of the surface location, a minimal possibility of streamwise flow separation or reversal exists. A value for ω can be obtained by introducing a safety factor σ, such that Eq (39) becomes

$$\omega = \frac{\sigma\gamma M_\xi^2}{1 + (\gamma - 1) M_\xi^2} \qquad (40)$$

By considering the maximum value that ω can have, $\omega = 1$, σ can be determined from Eq (40). This value of σ is then used to determine ω for specific flow conditions and is substituted into Eq (35) to solve the general flow field.

The Vigneron sublayer model was used in all PNS code simulations. A comparative case was run using the Schiff - Steger model to explore the occurrence of oscillations previously encountered by Neumann and Patterson, Reference 14. The results of the sublayer model comparison can be found in the following section.

4.2 PNS Code Output

The PNS code allows the user to select the type and

frequency of output generated during a simulation. The amount of data generated by the PNS code was considerable, so care was taken to print out only the data needed. The output data generated during a marching solution was divided into three basic groups: surface flow variables, body and shock geometry, and flow field variables. Data from all three groups was initially provided at each axial marching plane to observe general trends. Once a reasonable solution was obtained, the data were routinely output every 50 planes or at half inch locations since an axial step-size of DX = 0.01 inches was used.

Since this effort was primarily concerned with surface conditions, emphasis was placed on output data from the surface flow variables group. The data collected from this group included surface pressure ratio, P/P_{∞}, shear stress, τ_w, coefficient of friction, C_f, Stanton number, St, and heat flux, q. Values were collected at nondimensional axial locations starting at x/L = 0.02 (0.3 inches from the nose) and plots were generated to examine general trends. Often, the code predictions were compared to theoretical predictions to determine if reasonable trends existed. Experimental data were not used for comparison during the PNS simulations due to the objectives of this effort.

Data from the body and shock geometry group were used to verify the correct ogive-cylinder surface geometry and to examine shock location. For example, the ogive body radius at the starting plane must equal the starting solution nose

cone height, z, or a surface discontinuity will be created. Surface discontinuities could result in streamwise flow separations, thus invalidating the use of the PNS code. Initially, an error was made while defining the ogive geometry in the PNS code, resulting in z being larger than the ogive radius by 0.015 inches. Consequently, a sharp corner was created in the ogive surface which caused a local flow expansion region which then appeared as an oscillation in the pressure ratio curve. Figure 5 gives a qualitative representation of the effect that the surface discontinuity had on the pressure ratio at that point. The sudden decrease in pressure resulted from the PNS code attempting

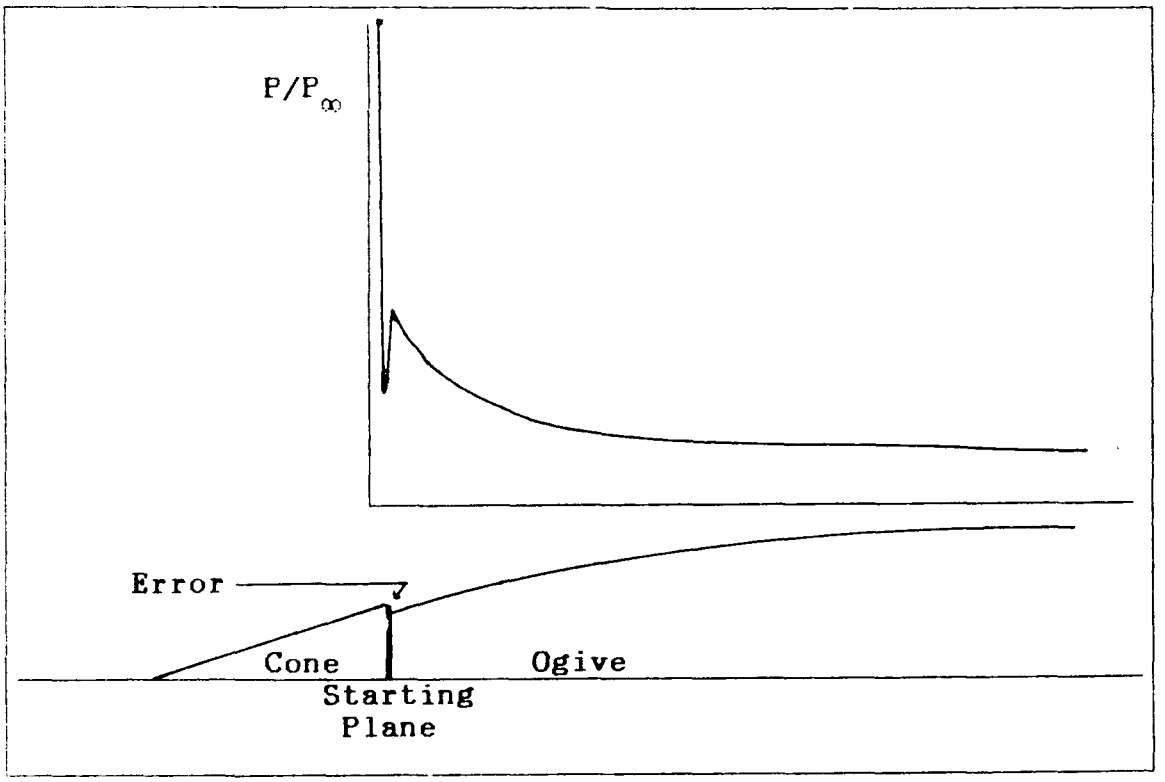

Figure 5. Cone - Ogive Surface Discontinuity

to model the expansion region encountered in the flow. Had the ogive radius been larger than the cone height, a streamwise flow separation might well have occurred, potentially causing a code failure.

The shock position relative to the axial location could also be examined using this data. Figure 6 shows the general shock shape and location relative to the ogive-cylinder body for M_∞ = 5.76 (upper shock line) and M_∞ = 5.90 (lower shock line). The nondimensional shock position has been plotted against the nondimensional axial location and the surface of the ogive-cylinder. Although the Mach number increase is small, Figure 6 illustrates the

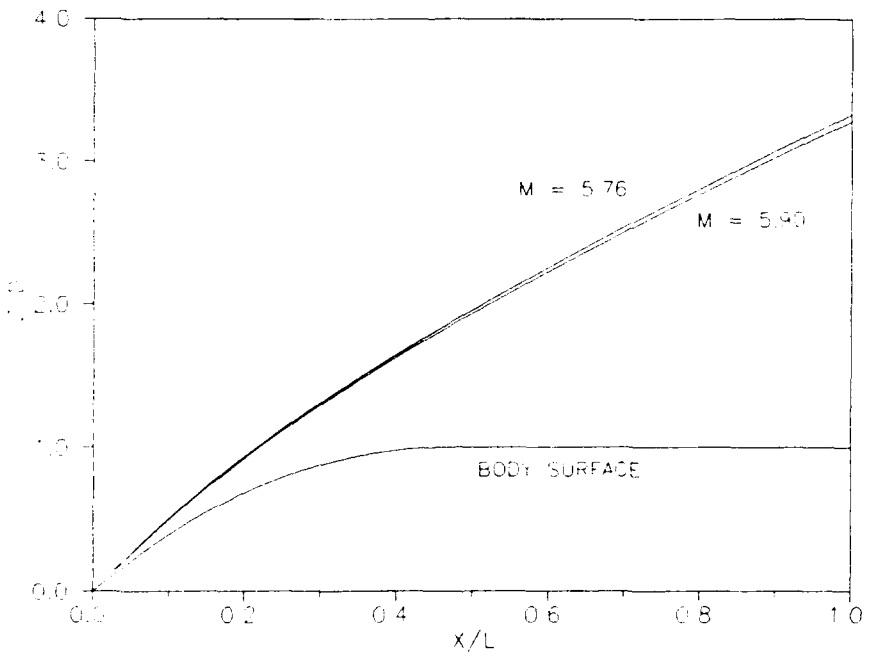

Figure 6. Shock Position on Ogive - Cylinder Body

hypersonic characteristic of decreasing shock angle with increasing Mach number.

Little use was made of the third group of output data, the flow field variables. As previously mentioned, emphasis was placed on surface conditions and not on the overall flow field.

4.3 Parametric Analysis

Conducting a complete parametric analysis on the PNS code input variables was beyond the scope of this effort. However, it was soon discovered that a few variables had a greater effect on heat transfer and skin friction than did others. Of the 91 input variables requiring definition, only eight (DS, LMAX, PER, IDPDX, LBLP, SMU, SMUIM, and EPSA) were considered in the following analysis. During the analysis, a set of laminar flow conditions was considered where $M_\infty = 5.78$ and $Re = 0.388 \times 10^6$. A set of turbulent flow conditions was also chosen in which $M_\infty = 5.90$ and $Re = 2.542 \times 10^6$. These conditions were consistent with experimental test conditions #2 and #5, respectively, which are defined in Chapter 5.

4.3.1 Geometry Definition Parameters. As expected, the variable controlling the placement of the first radial grid point away from the surface, DS, had a strong influence on heat transfer and skin friction results. Selecting a positive value for DS equated to defining a physical length in inches for the distance between the surface and the first

radial grid point. Since heat transfer and skin friction are functions of temperature and velocity gradients at the surface, reasonable results are dependent upon suitably small values of DS. Chaussee, Reference 6, suggested starting with a DS value of 0.001 and subsequently reducing its value to approximately 0.00005 (6:4). Although better resolution should be obtained closer to the surface, code failures often occurred in both the starting and marching solutions due to very small DS values. Quite literally, one had to find the smallest DS value that was both acceptable to the code and still provided reasonable results.

The strategy employed during this effort consisted of letting the nondimensional variable, y+, guide in the selection of DS. For laminar flows, y+ was not applicable and a laminar value for DS of DS = 0.00005 was chosen (15). For turbulent flows, the strategy required keeping y+ of the first interior point at a value of approximately two at the surface. This was accomplished as an iterative process. An initial value of DS was chosen and the code was run. The resulting y+ value, output with the surface flow variables, was checked. If y+ was greater than two, DS was reduced by an order of magnitude and the code was run again. This process was repeated until the desired value of y+ was obtained. After obtaining a converged starting solution with the desired DS value, a marching solution was attempted using the same DS value. Using the same DS value for both solutions minimized errors which may occur during grid

respacing in the code interpolation subroutine.

As mentioned above, a typical procedure started with a DS value of 0.005 and then reduced DS by an order of magnitude until a y+ value of approximately two was obtained. Figure 7 illustrates the effect of DS on Stanton number for three order of magnitude variations in DS. Reducing DS from 5 x 10^{-4} to 5 x 10^{-5} significantly improved the Stanton number prediction in the vicinity of the ogive-cylinder nose. All three curves converge on the same Stanton number prediction at x/L = 0.3 from the nose.

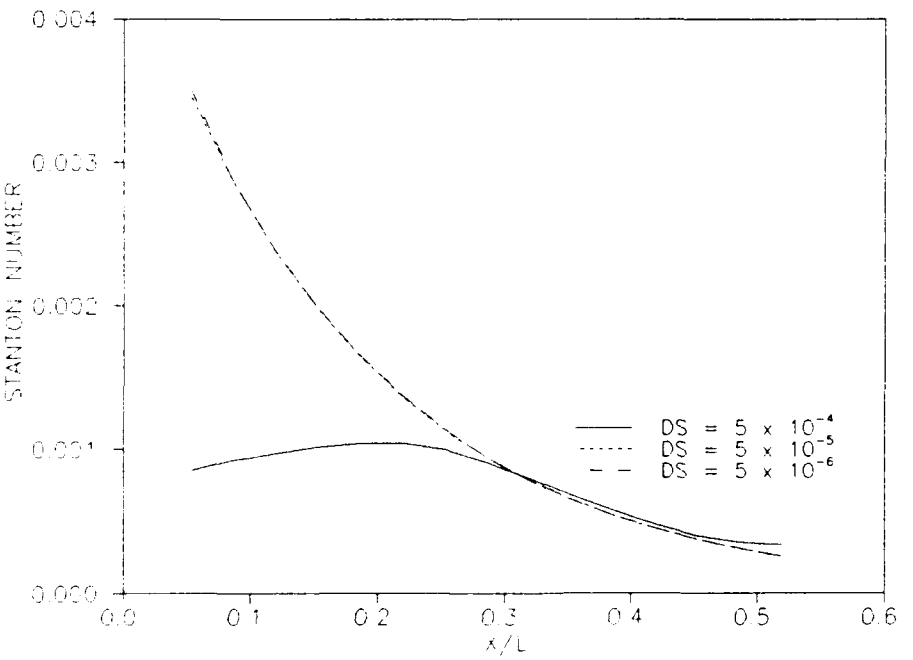

Figure 7. Effects of DS on Stanton Number

However, in the region of highest heat transfer, a significant difference exists for DS = 5×10^{-4} compared to DS = 5×10^{-5} and DS = 5×10^{-6}. It is also interesting to note that a further order of magnitude decrease in DS from 5×10^{-5} to 5×10^{-6} offered no improvement in Stanton number profile. The corresponding values of y+ for each DS value are presented in Table 1. A final value of DS = 0.00001 was chosen and successfully used for all turbulent cases.

Table 1. DS and y+ Values Corresponding to Figure 7

DS	y+
5.0×10^{-4}	16.910
5.0×10^{-5}	1.701
5.0×10^{-6}	0.170

Part of the parametric analysis consisted of a mesh resolution study to determine if the radial grid point density affected heat transfer and skin friction results. The input variable controlling the number of radial grid points was LMAX. The study considered LMAX values of 30, 60, 90, and 120 for both a laminar and a turbulent case. In each case, the number of circumferential grid points was held constant at KMAX = 19. Generally, all predictions were based on 120 radial grid points and 19 circumferential grid points for comparison to experimental data. Figure 8 shows

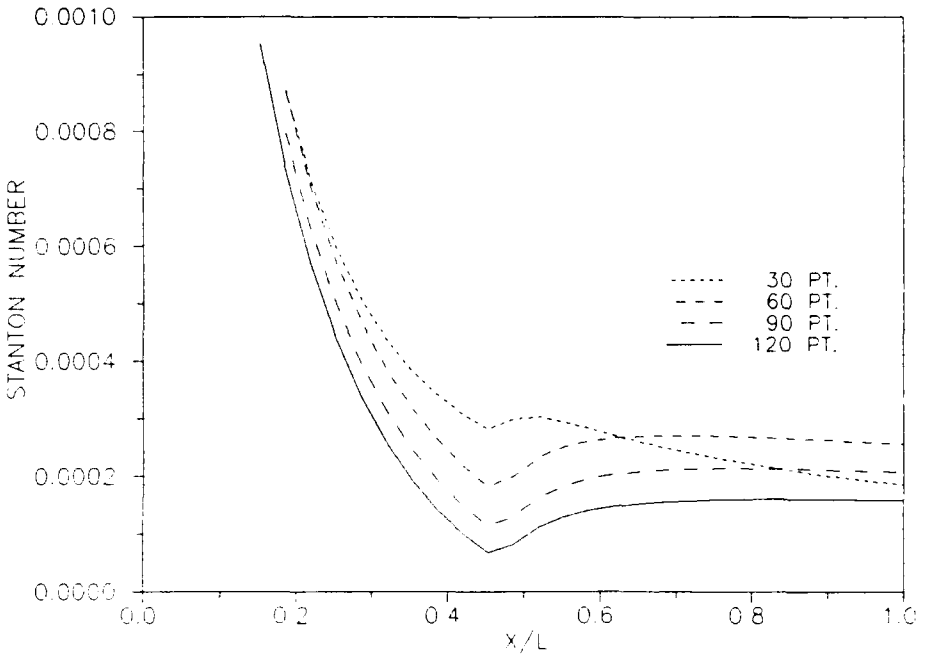

Figure 8. LMAX Effect on Stanton Number - Laminar Case

the results of the mesh resolution study for laminar heat transfer. Increasing the number of radial grid points resulted in a reduction of the local Stanton number predicted along the body. The local Stanton number at x/L = 0.487 (7.3 inches from the nose), decreased by an average value of 35 percent for each 30 point increase in grid density. However, the results along the ogive nose were all very similar. The inconsistent behavior of the 30 point curve in Figure 8 was attributed to the poor resolution of the thermal gradient at the surface in the presence of the growing boundary layer. As the boundary layer thickened along the body, 30 radial grid points provided too few points near the surface to adequately define the temperature gradient. A similar trend in skin friction for 30 point

increases in grid density can be seen in Figure 9. The average variation in skin friction coefficient at the same point, x/L = 0.487, was approximately 10 percent (excluding the 30 point curve).

For the turbulent heat transfer case, the results shown in Figure 10 suggest that all of the grid densities will provide similar results. A slight variation in the LMAX = 30 curve exists, but it was not considered excessive. Figure 11 contains the results of LMAX variation for skin friction for the turbulent case. Once again, all of the choices for LMAX provided similar results. Heat transfer and skin friction were less sensitive to LMAX variations in the turbulent case because of the nature of the turbulent boundary layer. The flatter profile allows the velocity and temperature gradients to be adequately defined by fewer radial grid points and hence, smaller values of LMAX. Thus, for the same DS value, little variation in heat transfer or skin friction occurred with LMAX variation for the range of LMAX values considered.

The final input variable in the geometry definition group to be considered was PER. This variable controls the percentage of grid points between the body and the shock which are to be clustered radially near the body surface. For instance, if PER = 0.5 and LMAX = 60, then 50 percent of LMAX, or 30 points, will be exponentially clustered near the surface starting at a physical distance defined by DS. The remaining points will be evenly distributed from the last

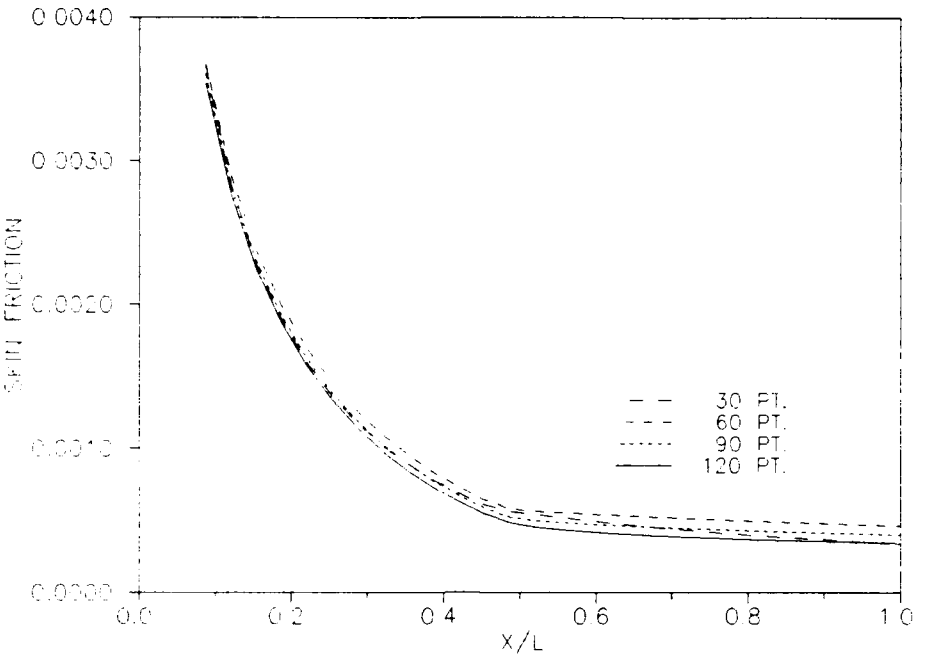

Figure 9. LMAX Effect on Skin Friction - Laminar Case

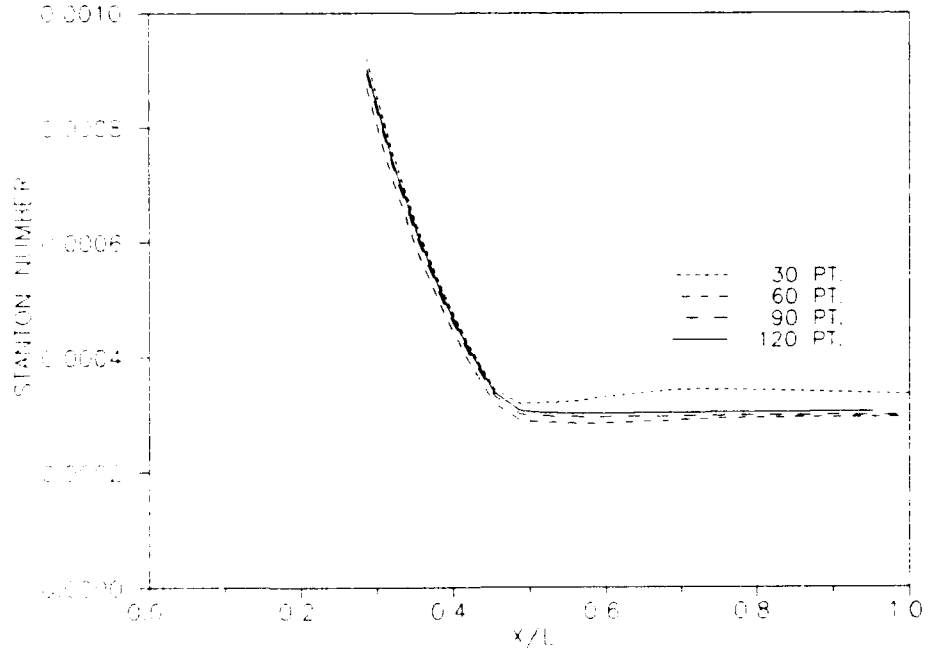

Figure 10. LMAX Effect on Stanton Number - Turbulent Case

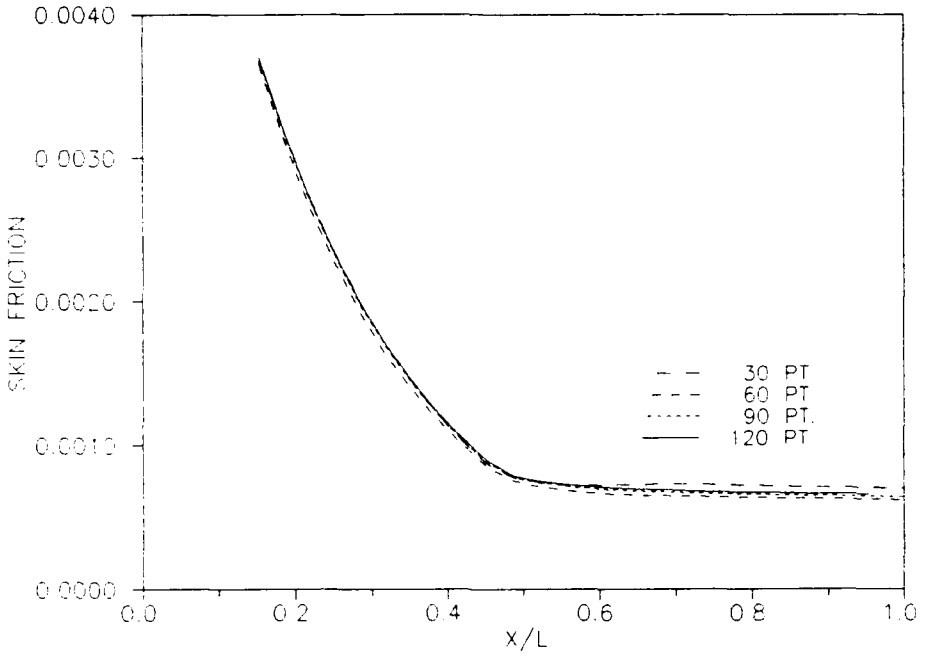

Figure 11. LMAX Effect on Skin Friction - Turbulent Case

clustered point to the shock. Figure 12 shows an example of the grid structure taken at x/L = 0.287 (4.3 inches from nose) for KMAX = 19, LMAX = 60 and PER = 0.5. The narrow, dark band results from clustering 30 radial grid points near the surface in a region where the shock is relatively close to the body. Since the body is axisymmetric, only 19 circumferential grid points are used to describe the ogive-cylinder geometry from 180° at the top to 0° at the bottom. The figure shows only a cross-sectional quadrant measuring 90° which contains nine circumferential segments.

Intuitively, clustering more points near the surface should improve boundary layer resolution but not necessarily heat transfer or skin friction. Since only three points were needed to curve-fit the slope of the velocity and

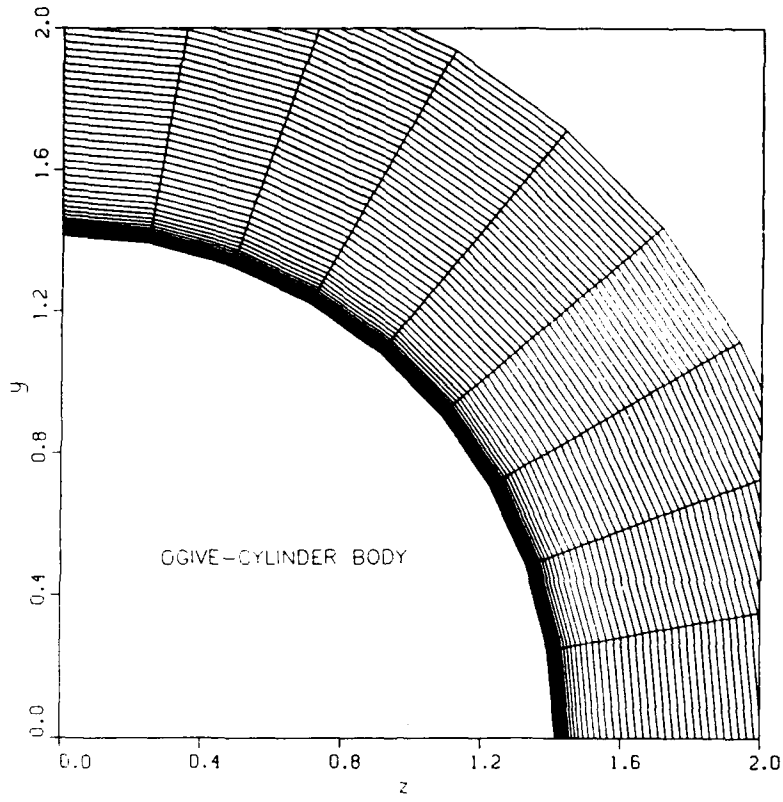

Figure 12. Grid Structure With Radial Clustering

temperature profiles, relatively low PER values provided reasonable results. For instance, the laminar case was considered where PER took on values from 0.2 to 0.7 with LMAX = 60. Stanton number results taken at x/L = 0.6 were essentially constant over the range of PER values. However, when the same case was run again using the same PER range, but LMAX reduced to LMAX = 30, larger Stanton numbers occurred for PER values below 0.4. The Stanton number variations resulted from poor temperature gradient resolution and were attributed to too few points near the surface for PER < 0.4. This conclusion was verified by examination of the boundary layer at x/L = 0.6. Since a

large LMAX value of 120 was used for comparison to experimental data, clustering 50 percent of the grid points radially was considered reasonable.

4.3.2 Integration Parameters. Only two input variables from this group, IDPDX and LBLP, were considered in the study. The first, IDPDX, was discussed in the section on sublayer models. As previously mentioned, the Vigneron sublayer model was used for all simulations with one exception. The Schiff-Steger sublayer model was used for the laminar case in an attempt to explore the occurrence of oscillations as reported by Neumann and Patterson, (14:4). For this case, values of LMAX = 60 and PER = 0.5 were used. Figure 13 shows a comparison of the two sublayer models for the laminar case. The scale has been expanded to show more detail for the pressure ratio curve in the vicinity of the ogive-cylinder shoulder located at x/L = 0.467 (7 inches from the nose). The Schiff-Steger model clearly had difficulty negotiating the expansion region. However, the two sublayer models compared favorably on either side of the shoulder. The Schiff-Steger model also produced oscillations in the heat transfer computations as seen in Figure 14. In this figure, the two models do not match as well for Stanton number as they did for pressure ratio. Oscillations occurred in the vicinity of the shoulder and appear to be centered around the junction of the ogive nose and the cylinder aft-body. The captions in Figures 13 and 14 refer to the Vigneron sublayer model as

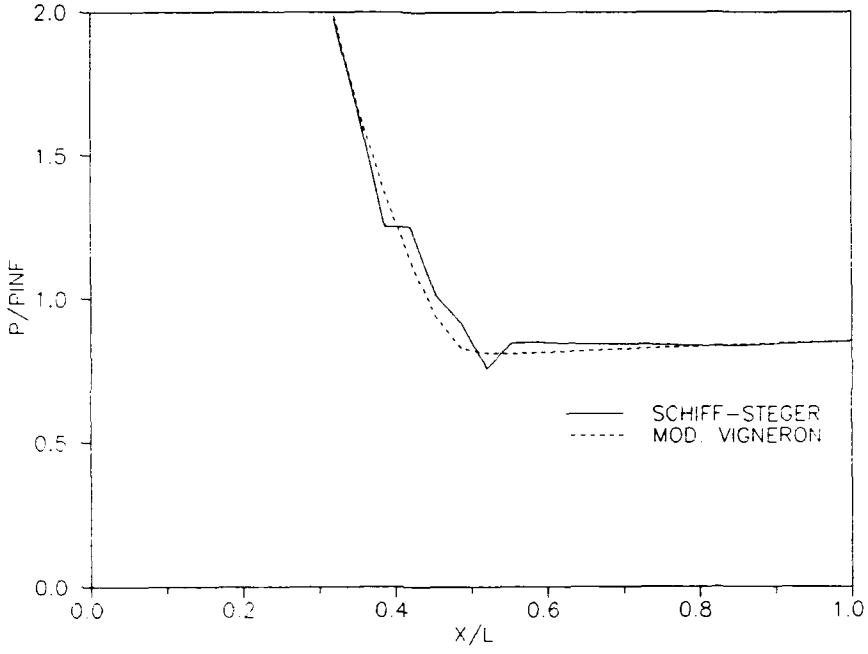

Figure 13. Sublayer Model Comparison for Pressure Ratio

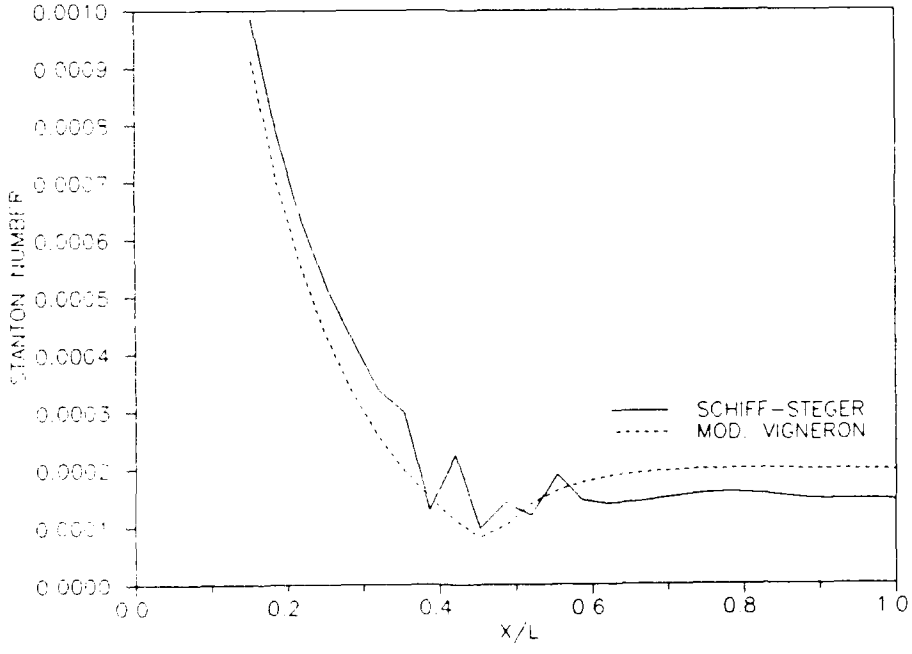

Figure 14. Sublayer Model Comparison for Stanton Number

the modified Vigneron sublayer model. The reason for this was Vigneron et al (16:2), applied the splitting technique only to the streamwise momentum equation, whereas the splitting technique was applied to both the streamwise momentum and energy equations in the improved PNS code (21:87). Based on these results, the modified Vigneron sublayer model was chosen as the preferred sublayer model for all predictions.

The second input variable studied from the integration parameter group was the boundary layer grid point index, LBLP. This variable determined the extent of application of the turbulence model and the point where the boundary layer variables were normalized. Initially, a value of LBLP equal to 75 percent of LMAX was used for all cases. However, this value was smaller than the LBLP value used in previous research and Reference (15) suggested using LBLP equal to 83 percent of LMAX. The larger value corresponds to the y/δ location in the boundary layer where $u \simeq 0.99u_e$. The test cases were run using both values of LBLP to explore its effects, if any, on heat transfer and skin friction results. Figure 15 illustrates the physical interpretation of LBLP. The difference between the 0.83 and 0.75 values shown in the figure results in a decrease in the area under the curve. The decrease in area corresponds to a loss of momentum that can affect the boundary layer properties. Comparing the two definitions of LBLP sheds some light on the gross boundary layer properties as computed by the PNS code. However, it

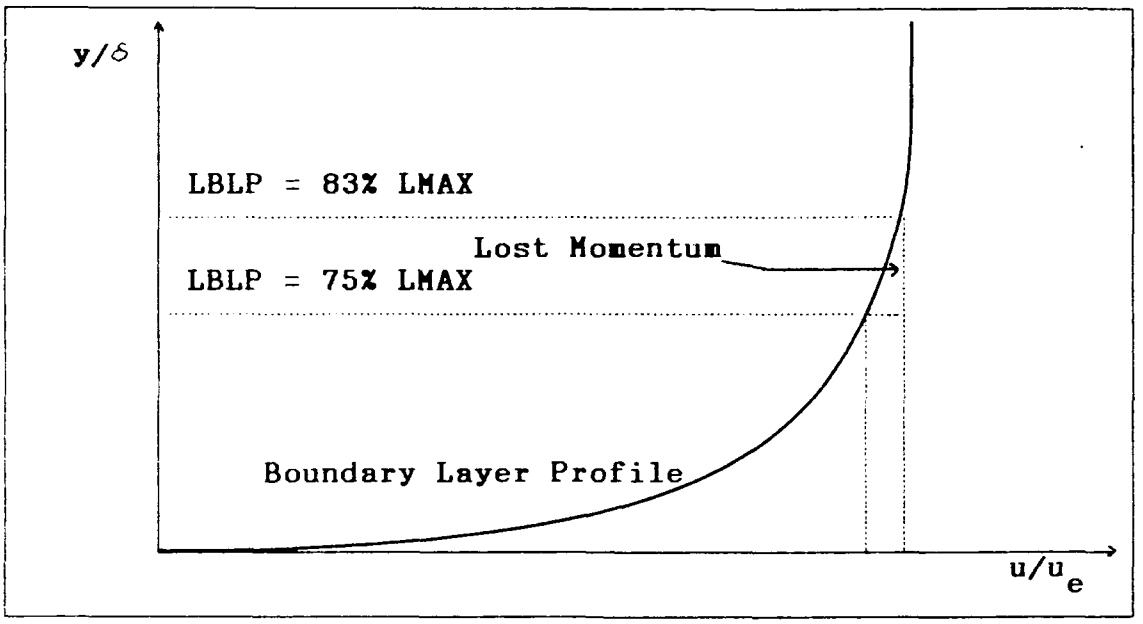

Figure 15. Physical Description of LBLP

was determined that the variation in LBLP had little effect on heat transfer and skin friction results. The LBLP variation can be gauged by considering its effect on the boundary layer displacement thickness, δ^*, where δ^* is given as:

$$\delta^* = \int_0^{(LBLP-1)} \left(1 - \frac{\rho u}{(\rho u)_{LBLP}}\right) dy \qquad (33)$$

Table 2 presents a comparison of LBLP values using four grid point densities and evaluating δ^* at x/L = 0.487 for the laminar case.

Table 2. LBLP Effects on Displacement Thickness

LMAX	30		60	
LBLP	23	25	45	50
δ^*	0.0248	0.0293	0.0217	0.0285
Δ(%)	+10.98	+2.01	-2.12	-0.72
LMAX	90		120	
LBLP	68	75	90	100
δ^*	0.0219	0.0284	0.0201	0.0285
Δ(%)	-0.84	-0.79	-9.30	-0.56

The percent variation, Δ(%), was determined by comparing each δ^* value to an overall average. For the 0.75 case, this value was $\delta^*|_{avg} = 0.02214$ and $\delta^*|_{avg} = 0.02868$ for the 0.83 case. Clearly, all values for δ^* using 0.83·LMAX agreed very well. The same was not true, however, for δ^* using 0.75·LMAX. The results presented in Table 2 would suggest a noticeable variation in δ^* exists between the two LBLP definitions along the surface of the ogive-cylinder body. Figure 16 shows the displacement thickness growth along the the body for the laminar case in which the two LBLP definitions are compared. Although the difference is noticeable, it should be re-emphasized that the smaller value of LBLP had little effect on the heat transfer and skin friction results at the surface of the body.

4.3.3 Smoothing Parameters. The PNS code uses four smoothing and conditioning terms (SMU, SMUIM, EPSA and EPSB) as part of the numerical formulation. The smoothing terms

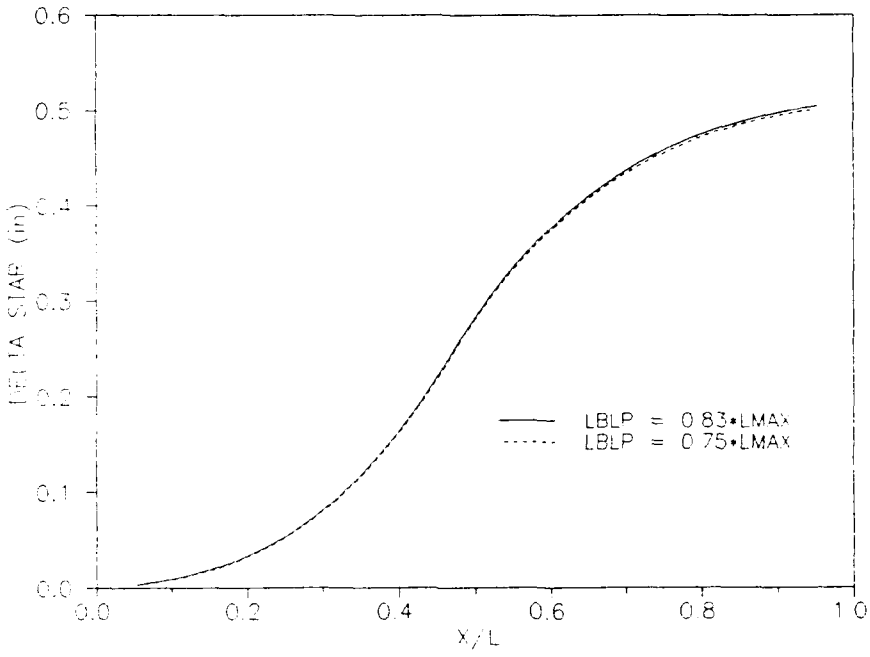

Figure 16. Displacement Thickness Comparison for LBLP

are required to damp high frequency oscillations that occur due to the odd-even uncoupling of grid points common to central difference formulations and to control nonlinear effects such as shocks. The conditioning terms adjust the eigenvalues of the difference matrices to avoid singularities and unstable imaginary modes (21:108).

The explicit damping term, SMU, is proportional to fourth order dependent variable differences in the circumferential and normal directions. Its value must be large enough so that oscillations in the shock shape are prevented. However, if SMU is too large,it can take on the character of a source term and non-physical results can occur in the solution. Stalnaker et al, Reference 21,

suggest a range of values for SMU between $1/16 \leq SMU \leq 1$. Various references consulted recommended keeping the damping term at its lowest possible value. An initial value of SMU = 0.1 provided adequate damping for the marching solutions and was eventually chosen for use in all numerical simulations. Favorable results were obtained for SMU = 0.2 for the starting solutions. Since there were no embedded or reflected shocks present in the flow field, there was little reason to explore variations in the value of SMU.

The implicit damping term, SMUIM, was included in the numerical formulation to maintain stability when large values of SMU were required. The range of acceptable values for SMUIM was given by Reference 21 as $2 \cdot SMU \leq SMUIM \leq 3 \cdot SMU$. For the starting solutions, a value of SMUIM = 0.4 was used and a value of SMUIM = 0.2 was used for the marching solutions.

The matrix conditioning terms, EPSA and EPSB, are included to condition the matrices appearing in the numerical formulation of the difference models. EPSA is present to ensure that the diagonal elements of the matrices were non-zero. EPSB modifies the rate at which the smoothing terms increase or decrease in size in response to changes in the circumferential or radial directions. A survey of literature indicated that EPSA and EPSB should be kept as small as possible, but no clear guidance was given as to how small. Stalnaker et al, Reference 21, suggested using a minimum value of either 0.1 or SMU to define EPSA.

Also, it was suggested that EPSB should be set equal to EPSA. Values for EPSA of 0.05 to 0.1 were also suggested in another reference (12:13). It was anticipated that larger values might be necessary due to the high Reynolds number flows investigated. Good results were obtained for EPSA = 0.2 to 0.3 and the decision was made to use the larger value. However, significant problems were encountered in the starting solution due to the small DS values used for the high Reynolds number flows. After extensive investigation (approximately 54 starting solution attempts), it was discovered that converged solutions could be obtained by carefully selecting values for EPSA and EPSB while keeping the desired values for DS, SMU and SMUIM. For instance, with EPSA = 0.5, significant high frequency oscillations occurred during the iteration process for a laminar flow case as evidenced by the AMAX curve in Figure 2a. The same case failed to converge for EPSA values of 0.2 to 0.4. Only after setting EPSA = 0.5 was a converged solution obtained. This involved a rather painstaking process in which EPSA was increased by increments of 0.01 and the starting solution was executed until convergence was achieved. Additionally, increasing EPSA to a value of 1.0 suppressed the high frequency oscillations as evidenced by Figure 3. The lesson learned from this experience was that the best choice of EPSA depended on many factors and often could only be found after extensive trial and error.

A similar situation occurred for the turbulent case

shown in Figure 4. Initial EPSA values of 0.3 failed to result in convergence and subsequent increases were attempted. Convergence was finally achieved for a value of EPSA = 1.0. However, further investigation revealed that a lower EPSA value, EPSA = 0.95, would sometimes result in convergence, while at other times divergence would result. Apparently, the starting solution calculations were very sensitive to values between 0.95 and 0.99 for the flow conditions considered. To be safe, a value of EPSA = 1.0 was used for the turbulent cases.

A probable explanation for the problems encountered with the starting solutions can be found in the events occurring during the iterative process. The radial location in which flow computations are occurring changes as each iteration moves the shock closer to the actual converged viscous shock location. As a result, the smoothing terms are incapable of preventing instabilities from occurring with a low value of EPSB. Increasing EPSA and, consequently EPSB, stabilizes the fluctuations occurring in the radial direction by modifying the smoothing terms as changes in the radial direction occurred. The larger values of EPSA and EPSB were sufficient to obtain converged starting solutions.

Once satisfied that reasonable laminar and turbulent starting solutions were obtained, marching solutions were attempted using flow field values consistent with the planned experimental test conditions. Actual comparisons to experimental data would be done only after successfully

obtaining what was considered to be the best possible PNS predictions.

V. COMPARISON WITH EXPERIMENTAL DATA

5.1 Experimental Data

5.1.1 Facilities. The Air Force Wright Research and Development Center Mach 6 High Reynolds Number Facility was used to gather the experimental data contained in this thesis. The Mach 6 wind tunnel is an intermittent, blow-down type tunnel with an axisymmetric, 12.346-inch nozzle exit diameter. Figure 17 is a photograph of this Mach 6 wind tunnel located in building 450. The direction of air flow is from right to left, relative to the reader. In the test section, the open jet length can be varied from 17 inches to 28 inches. A storage heater, containing 50,000 pounds of stainless steel balls, heats the air supply from 900 to 1100 $^{\circ}$R. This temperature range is high enough to prevent air liquefaction from occurring in the test section during hypersonic testing. A test section free stream Reynolds number range of 1.5 million to 30 million (per foot) is possible by varying the tunnel reservoir pressure from 100 psia to 2000 psia. This Reynolds number range produced laminar through fully developed turbulent boundary layers on models in the test s ction. Tunnel run times are dependent on the vacuum pumping system for low Reynolds number tests and on the storage heater capacity for high Reynolds number tests. Several four minute, low Reynolds number tests were possible per day while only a single three

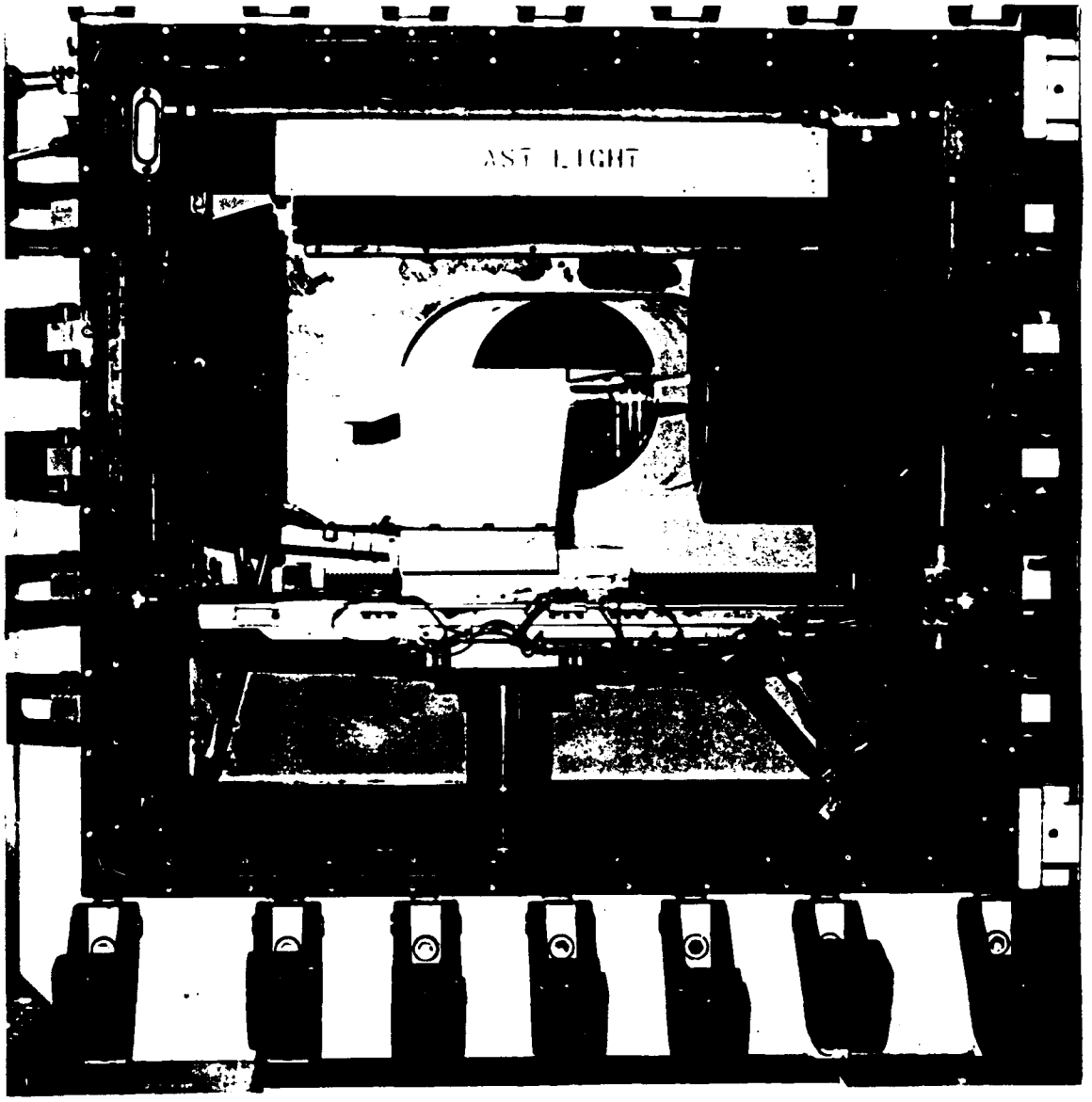

Figure 17. Test Section of the WRDC Mach 6 Wind Tunnel

minute, high Reynolds number test could be performed per day (13:1,5). Since several tests were of the high Reynolds number, turbulent flow type, great care was taken to ensure that the data acquisition system was properly functioning and that the ogive-cylinder model was correctly installed in the test section before each test.

5.1.2 Ogive-Cylinder Model. The experimental data used for comparison to the PNS code predictions were taken from the ogive-cylinder model shown in Figure 18. The two piece model was of stainless steel construction and had dimensions of 15 inches total length and 3.0 inches in diameter. The ogive nose section had a radius of curvature

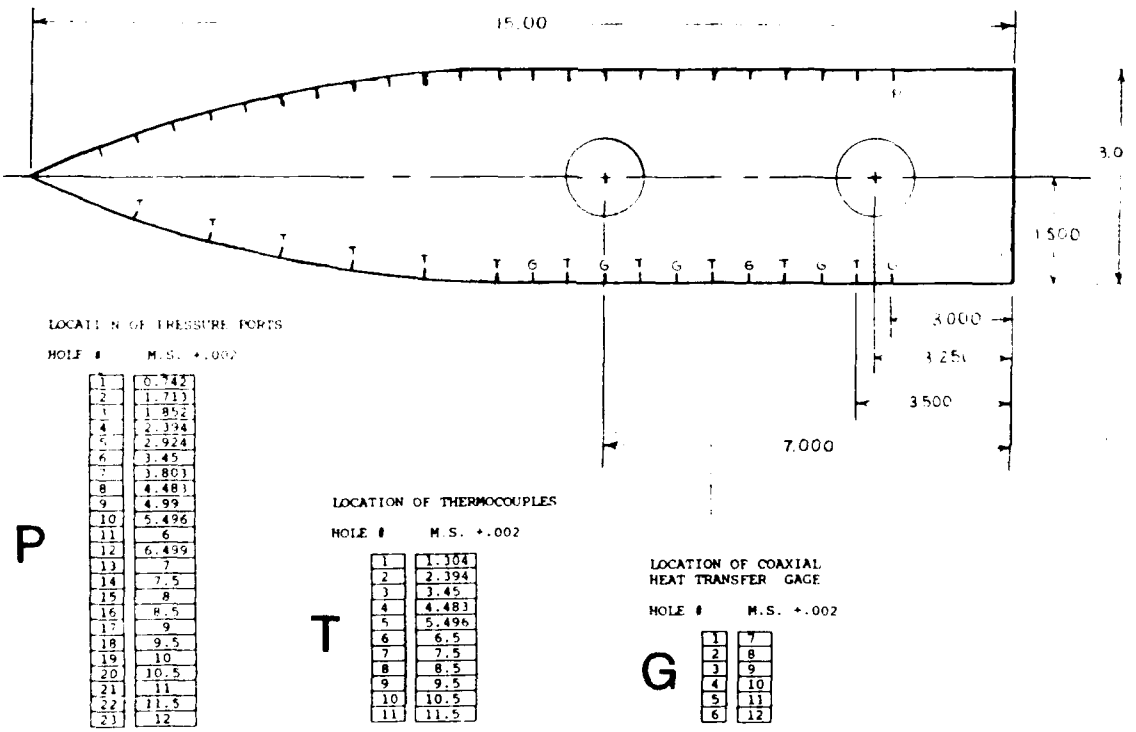

Figure 18. Ogive - Cylinder Model

of 17.083 inches and a nose length of 7 inches. The cylindrical aft-body was 8 inches long (17). The two piece construction was necessary to provide access to the instrumentation contained within the model. The two pieces joined together along an axial interface in such a way as to not interfere with the flow passing directly over any of the 42 different instrumentation ports. The surface of the ogive-cylinder model was very smooth and the model did not employ any flow tripping devices.

Model instrumentation included static pressure taps, thermocouples, coaxial heat transfer gauges and skin friction gauges. Table 3 presents the location of the static pressure taps positioned along the surface of the model. Surface locations, as well as dimensional and nondimensional axial locations, are given relative to the pressure tap position. The location of the thermocouples along the surface is given in Table 4 and Table 5 presents the location of the heat flux coaxial heat transfer gauges. Originally, three floating balance skin friction gauges were to be used, but only two could be mounted in the model due to test section blockage considerations. Table 6 presents the skin friction gauge location data. The pressure taps were positioned along the surface of the model at a circumferential position different than the other instrumentation locations. The thermocouples and coaxial heat transfer gauges were interspersed axially along the cylindrical aft-body. As a matter of fact, all of the heat

transfer and skin friction gauges were located on the cylindrical part of the model and only pressure and thermocouples were located on the model ogive nose.

Table 3. Ogive-Cylinder Pressure Tap Locations

Pressure Tap #	Surface Pos. (in)	Axial Pos. (in)	$\frac{x}{L}$
1	1.21314	0.74175	0.049
2	1.71314	1.30399	0.087
3	2.21314	1.85210	0.124
4	2.71314	2.39385	0.159
5	3.21314	2.92395	0.195
6	3.71314	3.44984	0.230
7	4.21314	3.80300	0.254
8	4.71314	4.48349	0.298
9	5.21314	4.99019	0.333
10	5.71314	5.49642	0.366
11	6.21314	6.00004	0.400
12	6.71314	6.49896	0.433
13	7.21314	7.00000	0.467
14	7.71314	7.50000	0.500
15	8.21314	8.00000	0.533
16	8.71314	8.50000	0.567
17	9.21314	9.00000	0.600
18	9.71314	9.50000	0.633
19	10.21314	10.00000	0.667
20	10.71314	10.50000	0.700
21	11.21314	11.00000	0.733
22	11.71314	11.50000	0.767
23	12.21314	12.00000	0.800

Table 4. Ogive-Cylinder Thermocouple Locations

Thermo-couple #	Surface Pos. (in)	Axial Pos. (in)	$\frac{x}{L}$
1	1.71314	1.3039	0.087
2	2.71314	2.3938	0.159
3	3.71314	3.4498	0.229
4	4.71314	4.4834	0.298
5	5.71314	5.4964	0.366
6	6.71314	6.4989	0.433
7	7.71314	7.5000	0.500
8	8.71314	8.5000	0.567
9	9.71314	9.5000	0.633
10	10.71314	10.5000	0.700
11	11.71314	11.5000	0.767

Table 5. Ogive - Cylinder Coaxial Gauge Location

Coaxial Gauge #	Surface Pos. (in)	Axial Pos. (in)	$\frac{x}{L}$
1	7.21314	7.0000	0.467
2	8.21314	8.0000	0.533
3	9.21314	9.0000	0.600
4	10.21314	10.0000	0.667
5	11.21314	11.0000	0.733
6	12.21314	12.0000	0.800

Table 6. Ogive-Cylinder Skin Friction Gauge Location

Gauge #	Surface Pos. (in)	Axial Pos. (in)	$\frac{x}{L}$
1	8.2134	8.0000	0.533
2	11.9631	11.7500	0.783

5.1.3 Test Conditions. The original intent of this research effort was to compare PNS code heat transfer and skin friction predictions to experimental data from hypersonic turbulent flows. However, the test plan was expanded to include additional laminar flow tests. Table 7 shows the test matrix containing the range of test conditions (T/C's) conducted in the Mach 6 wind tunnel.

Table 7. Ogive-Cylinder Test Conditions

T/C #	Mach #	Total Pressure (psia)	Reynolds # (per inch)	Flow Type
1	5.76	100	133,333.3	Laminar
2	5.78	300	387,500.0	Laminar
3	5.79	700	883,333.3	Transition
4	5.86	1400	1,750,000.0	Turbulent
5	5.90	2000	2,541,666.7	Turbulent

Several tests were conducted for each set of test conditions and the results were compiled and presented as average local Reynolds number, local Stanton number, local heat flux, and local skin friction values. Data reduction was performed by the WRDC/FIMG project engineer and the Mach 6 wind tunnel staff. Each test condition was assigned a specific symbol for data representation and that symbol was used consistently throughout this thesis. Table 8 describes the symbols used.

Table 8. Data Symbol Definition

T/C #	Symbol Used
1	Circle
2	Square
3	Triangle
4	Diamond
5	Star

5.1.4 Experimental Uncertainties. Measurement uncertainties are given in the following tables. Table 9 presents the basic experimental measurement uncertainties while Table 10 presents the parameter uncertainties determined from the basic measurements. These uncertainties formed the error bands used for comparison between the experimental data and the PNS code predictions.

Table 9. Experimental Measurement Uncertainties (14)

T/C #	T (%)	ρ (%)	U_∞ (%)	M_∞ (%)
1	0.3	13.72	1.18	1.05
2	0.3	12.90	1.34	1.22
3	0.3	5.77	1.02	0.86
4	0.3	3.32	1.32	1.20
5	0.3	2.78	1.79	1.70

Table 10. Parameter Uncertainties (14)

T/C #	P (%)	Re_x (%)	St (%)	C_f (%)
1	13.72	3.26	15.93	8.17
2	12.90	3.11	15.25	8.05
3	5.76	1.72	9.96	4.48
4	3.31	1.37	8.79	3.62
5	2.76	1.34	8.69	3.61

5.2 PNS Code and Data Comparisons

The goal of this research effort was to generate PNS code predictions for both laminar and turbulent hypersonic, viscous flows over an ogive-cylinder body. The specific focus of the effort was to compare the predictions for local Stanton number and local skin friction coefficient to experimental data. Although surface pressure ratio was not included in the specific focus of this effort, it served as an additional measure of the code's overall predictive capability. Instead of placing error bands on the pressure ratio and Stanton number figures, tables have been included for test conditions #2 and #5 to compare the experimental data to the PNS code output at each heat flux or pressure sensor location.

5.2.1 Surface Pressure Ratio. In general, PNS codes do a good job of predicting surface pressures over axisymmetric bodies at small angle of attack (19:1). The following figures support this statement for the

ogive-cylinder body at zero angle of attack. Surface pressure measurements, taken at approximately half inch intervals along the ogive-cylinder body, were divided by the free stream static pressure to obtain a nondimensional ratio. Figure 19 shows the surface pressure ratio versus axial location for all five test conditions. The spread of data at each axial location indicates a reasonably consistent pressure transducer response over the range of stagnation pressures investigated. However, the pressure transducer response for test condition #1, P_o = 100 psia, M_∞ = 5.76 and $Re_L = 0.133 \times 10^6$, displayed more variation than

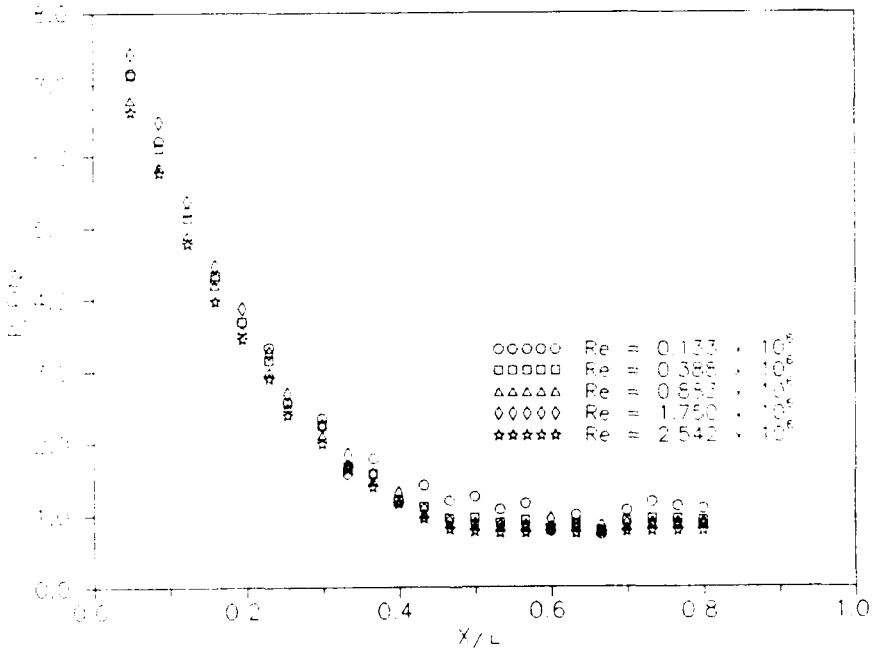

Figure 19. Surface Pressure Ratio - All Test Conditions

the other four tests. This variation can be seen in Figure 20 in which the data points are mildly scattered above and below the prediction curve given by the code. It appears in the figure that the PNS code over-predicts the surface pressure ratio near the ogive nose. However, all of the predicted pressure ratio points lie within the experimental data error band for test condition #1. The table containing this information can be found in Appendix C. The average error band for the experimental data was ± 13.7 percent. This value was also the largest average error of all tests and resulted from the insensitivity of the pressure transducers. The transducers were rated at 15 psi, but were attempting to measure the very low pressures of 0.1 to 0.2 psi.

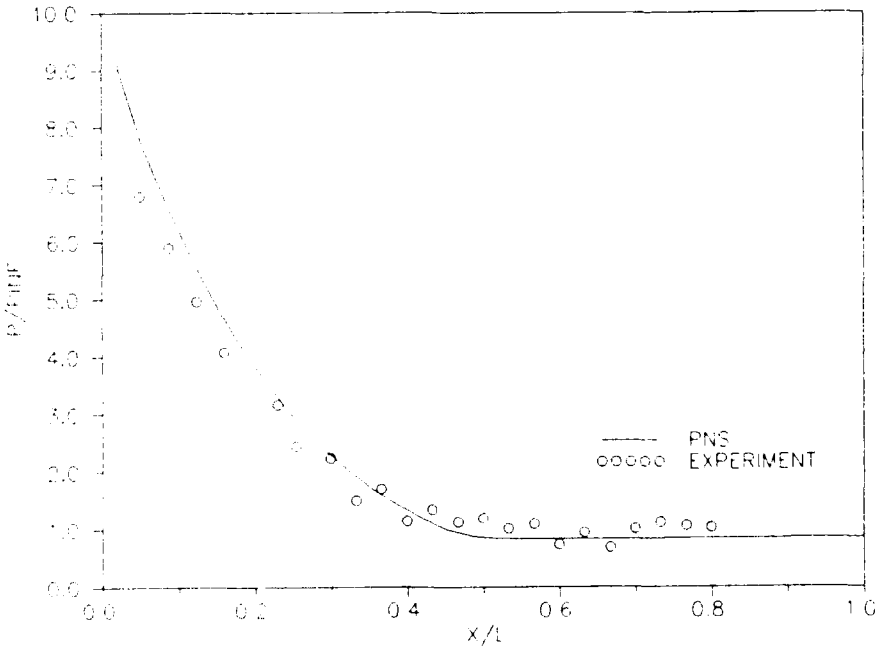

Figure 20. Surface Pressure Ratio - Test Condition #1

The results from test condition #2, P_o = 300 psia, M_∞ = 5.78 and $Re_L = 0.387 \times 10^6$, can be seen in Figure 21. Clearly, the code and data are in good agreement. In this case, the code did over-predict the surface pressure in the vicinity of the nose. This trend quickly diminished and the predicted values fell nicely within the error bands as shown in Table 11. The average error in surface pressure for test

Table 11. Surface Pressure Ratio Error Band - T/C #2

Pressure Tap #	Experimental Data (Error Band)	PNS Code
1	5.769 - 7.478	7.660
2	4.947 - 6.412	6.573
3	4.154 - 5.385	5.614
4	3.510 - 4.549	4.625
5	2.984 - 3.869	3.720
6	2.552 - 3.307	3.128
7	2.077 - 2.693	2.621
8	1.819 - 2.358	2.188
9	1.358 - 1.761	1.822
10	1.269 - 1.645	1.513
11	0.975 - 1.264	1.254
12	0.907 - 1.176	1.038
13	0.772 - 1.000	0.885
14	0.779 - 1.010	0.822
15	0.715 - 0.927	0.815
16	0.744 - 0.964	0.816
17	0.654 - 0.847	0.819
18	0.701 - 0.909	0.823
19	0.633 - 0.821	0.830
20	0.736 - 0.954	0.828
21	0.772 - 1.000	0.832
22	0.758 - 0.983	0.834
23	0.747 - 0.969	0.837

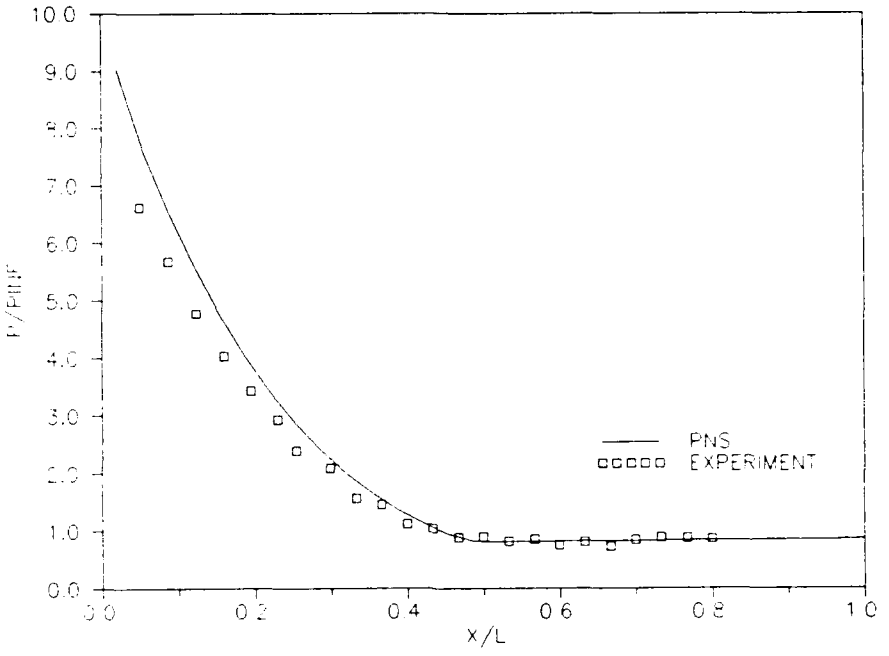

Figure 21. Surface Pressure Ratio - Test Condition #2

condition #2 was ± 12.9 percent. The average surface pressure error also decreased as the stagnation pressure increased. Figure 22 shows the comparison between the code and the data for the test condition in which P_o = 700 psia, M_∞ = 5.79 and the free stream Reynolds number was 0.883 x 10^6. The code and the data agree very well and it is clear that most of the variations in data due to pressure transducer insensitivity have vanished. The code results are shifted more towards the high side of the experimental data error band as can be seen in Appendix C. Test condition #3 had an average error of ± 5.76.

The results shown in Figure 23 suggest that the PNS code performed as well for a turbulent flow case as it

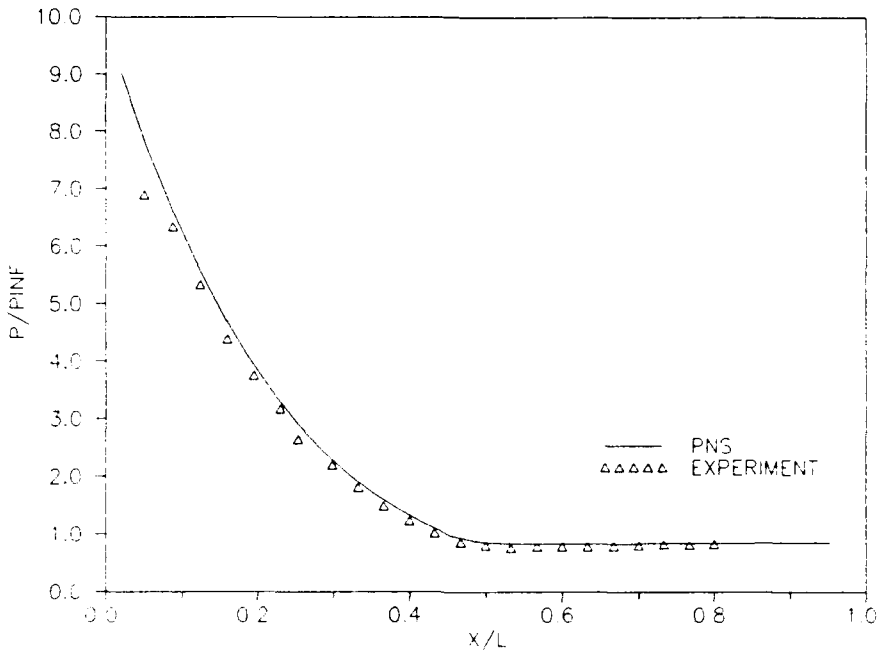

Figure 22. Surface Pressure Ratio - Test Condition #3

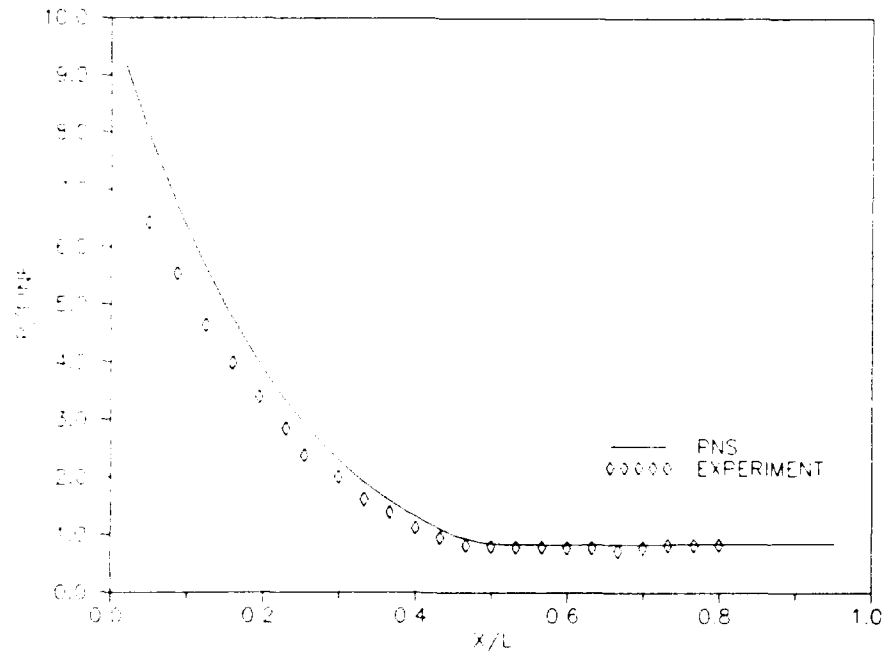

Figure 23. Surface Pressure Ratio - Test Condition #4

had for the previous laminar flow cases. Although the error band for this data was ± 3.31 percent, corresponding to P_o = 1400 psia, M_∞ = 5.86 and Re_L = 1.750 x 10^6, the difference between code predictions and data on the ogive nose is considerably larger than for the laminar cases. Along the ogive nose, for example, the code predicted values approximately 10 percent higher than the data error band for the first eight pressure tap locations. As a matter of fact, only one predicted surface pressure ratio value fell within the data error band along the entire ogive-cylinder. The last test condition to be considered had a free stream Mach number of M_∞ = 5.90, P_o = 2000 psia and a Reynolds number of 2.542 x 10^6. The results shown in Figure 24 for PNS code prediction compared to experimental data are also in good agreement. A point by point comparison between the predicted values and the data for this case is presented in Table 12. This test condition had the lowest average data error of ± 2.76 percent.

Some general observations can be made about the surface pressure ratio comparisons shown in Figures 20 through 24. First, all of the PNS predictions appear to be in very good agreement with the experimental data taken over a wide range of Reynolds numbers, i.e. 0.133 x 10^6 to 2.542 x 10^6. The predictions also appear to compare more favorably as the Reynolds number increases. Second, both the code predictions and the data agree well in the region around the ogive-cylinder shoulder. Although the ogive geometry

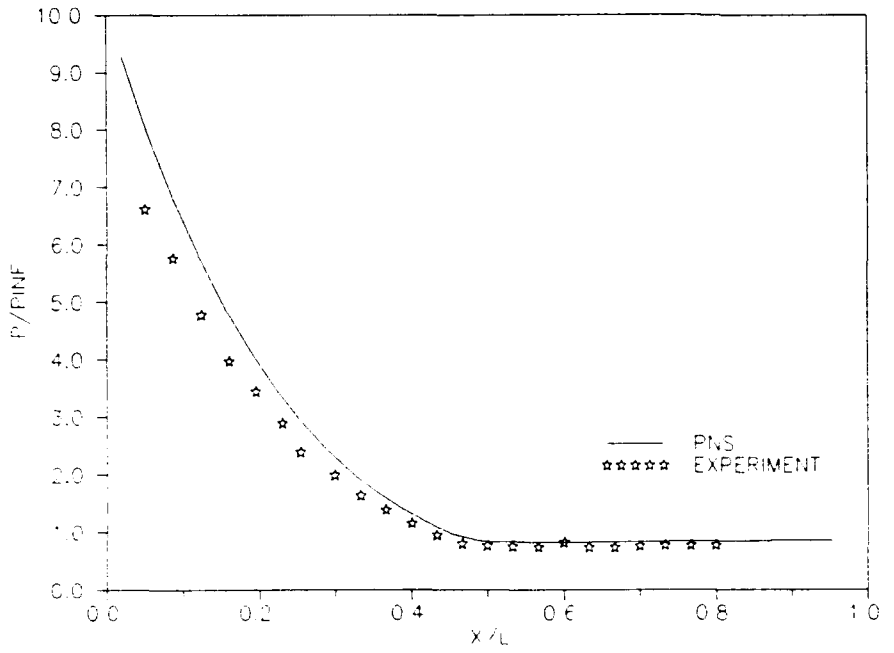

Figure 24. Surface Pressure Ratio - Test Condition #5

Table 12. Surface Pressure Ratio Error Band - T/C #5

Pressure Tap #	Experimental Data (Error Band)	PNS Code
1	6.711 - 7.093	7.937
2	6.169 - 6.520	6.810
3	5.183 - 5.477	5.814
4	4.263 - 4.505	4.939
5	3.655 - 3.863	3.845
6	3.089 - 3.260	3.231
7	2.570 - 2.716	2.948
8	2.132 - 2.254	2.257
9	1.756 - 1.856	1.878
10	1.446 - 1.528	1.560
11	1.192 - 1.259	1.293
12	0.988 - 1.045	1.073
13	0.839 - 0.886	0.916
14	0.788 - 0.833	0.849
15	0.741 - 0.783	0.833
16	0.760 - 0.803	0.828
17	0.759 - 0.803	0.829
18	0.759 - 0.803	0.831
19	0.775 - 0.819	0.834
20	0.787 - 0.832	0.837
21	0.802 - 0.848	0.840
22	0.791 - 0.835	0.843
23	0.806 - 0.852	0.846

blends smoothly into the cylindrical aft-body, an expansion region of Prandtl-Meyer flow exists and the code handled the region reasonably well. Finally, the PNS code static pressure predictions were always larger than the experimental data. The code never once predicted values smaller than the lower data error band for any part of the ogive-cylinder body.

5.2.2 Heat Transfer. The local Stanton number was chosen as the best heat transfer characteristic to examine in comparing PNS predictions to the experimental results. Stanton number, defined in Chapter 2, was shown to be dependent upon the heat flux, q. The heat flux, in turn, is a function of the thermal conductivity of the air and the temperature gradient normal to the surface. As expected, proper definition of the thermal gradients at the surface proved to be the key in obtaining reasonable heat transfer results from the PNS code

It was previously mentioned that the widely varying behavior in local Stanton number, displayed in Figure 8, was due to poor resolution of the thermal gradient at the surface. Poor resolution occurred because too few radial grid points were used even though DS was very small. Based on the results of the parametric analysis, the decision was made to use 120 radial grid points and cluster 50 percent of the points near the surface for all numerical simulations. Increasing the number of radial grid points was just one of several steps taken to ensure reasonable results. It was

also necessary to ensure that heat transfer values from the starting solution were reasonably close to the heat transfer values computed by the marching solution at the first plane. This was necessary to prevent large discrepancies between the two solutions from being propagated along in the marching solution (15). A reliable means of verifying consistency between the two solutions involved examination of their respective boundary layers at the first marching plane, x/L = 0.02067 (0.31 inches from nose). For instance, Figure 25 shows the two boundary layer profiles for the laminar case (T/C #2). Clearly, the slopes of the two

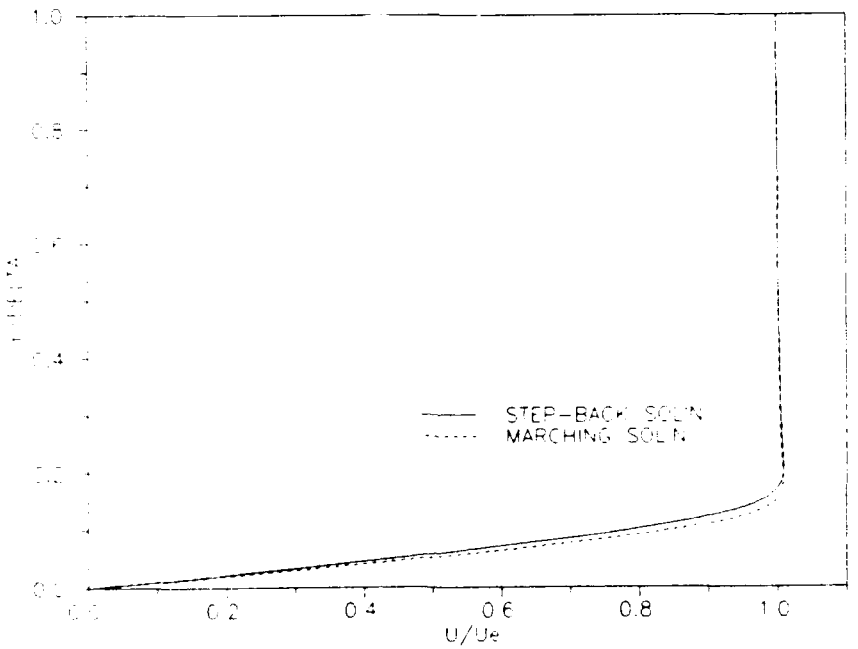

Figure 25. Boundary Layer Profile - Test Condition #2

curves are indistinguishable near the surface ($y/\delta \simeq 0$). As a result, only very small differences existed between the heat transfer computations made during the starting solution and those made during the marching solution in the vicinity of $x/L = 0.02067$. Furthermore, several closely-spaced points were located near the surface and very good thermal gradient resolution occurred. The boundary layer profile obtained for T/C #2 was similar to the boundary layer profiles for T/C #1 and T/C #3. As a result, heat transfer results from the PNS code agreed well with the experimental data.

The laminar flow solutions proved to be easier to obtain than the turbulent flow solutions. Obtaining starting solutions for the turbulent flows caused a great deal of trouble and required several days of "fine-tuning" before the right combination of input variables was discovered. Figure 26 is a good case in point. This particular turbulent flow case, T/C #5, required a very large value of EPSA (EPSA = 1.0) before convergence was achieved. The large smoothing value resulted in poor agreement between the starting and marching solution boundary profiles. The large variation between the two profiles was attributed to the EPSA value damping out the higher order derivative terms in the starting solution numerical formulation. It should be noted, however, that even though the two profiles shown in Figure 26 do not closely match, their slopes near the surface were similar

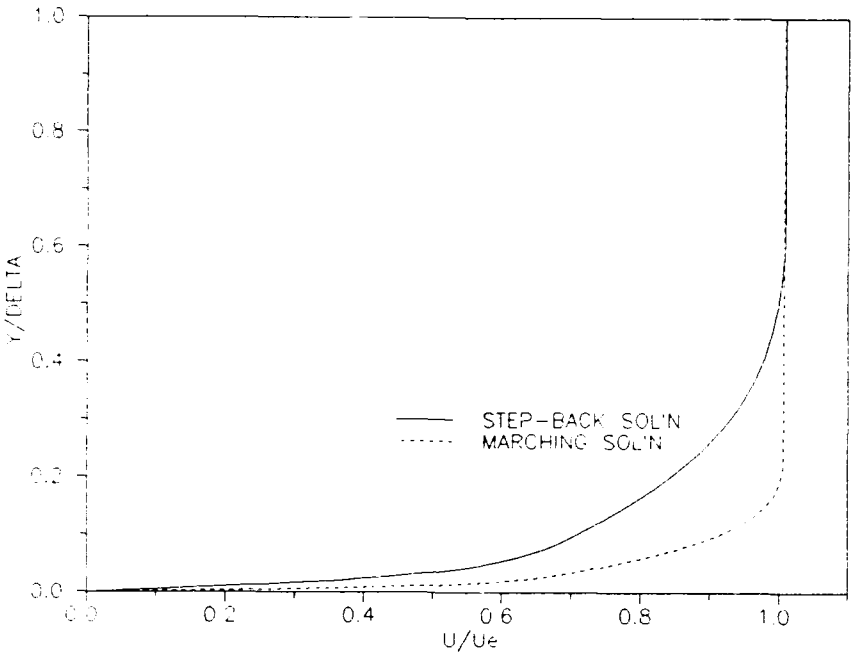

Figure 26. Boundary Layer Profile - Test Condition #5

enough that a reasonable approximation for the thermal gradient existed. A comparison of Figures 25 and 26 also reveals that the marching solution in Figure 25 is representative of a characteristic laminar boundary layer profile and the marching solution in Figure 26 is characteristic of a turbulent boundary layer profile. The turbulent boundary layer profile is fuller and has a steeper gradient at the surface than the laminar boundary layer profile. The boundary layer profiles were considered reasonable if the velocity ratio, u/u_e, for the first radial point was less than 0.1 to 0.15 as suggested by Reference 21. The value of u/u_e for the first non-zero radial point typically had a value less than 0.05, which indicated that

very good boundary layer resolution was achieved.

Once convinced that the boundary layer profiles, and hence, thermal gradients, were reasonable, marching solutions along the length of the ogive-cylinder body were generated. Although predictions were made starting very close to the ogive nose, no experimental data was generated in that region to substantiate the code's predictions. However, the flow near the surface was affected by the ogive nose and some of these effects still lingered as the flow came into contact with the first coaxial heat transfer gauge located at the shoulder. Figure 27 shows the comparison between the code predictions and the data for local Stanton number for test condition #1. Good agreement exists along the cylindrical aft-body after the code negotiates the flow expansion at the shoulder. In the region of the shoulder, though, the code slightly under - predicted Stanton number and it was difficult to differentiate between a data trend that was increasing towards the nose and data error associated with measurement uncertainties. The error band for the average Stanton number error was ± 15.93 percent. A table of data error and code prediction comparisons is included in Appendix C.

The PNS code predictions for local Stanton number for test condition #2 can be seen in Figure 28. It appears that very good agreement between the code and the data exists, although a characteristic of the code is to under-predict the heat transfer at the shoulder of the

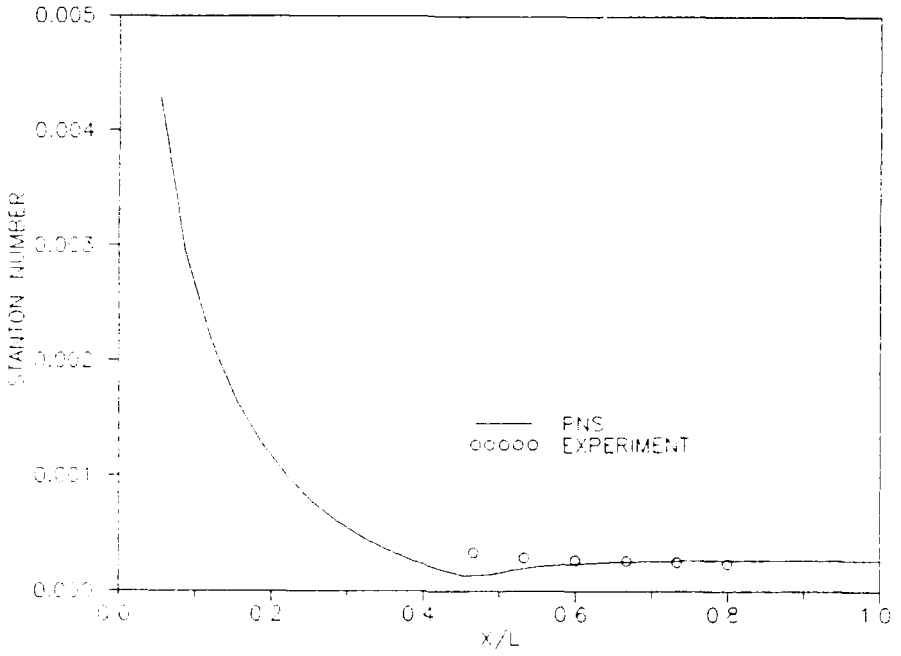

Figure 27. Stanton Number Comparison - Test Condition #1

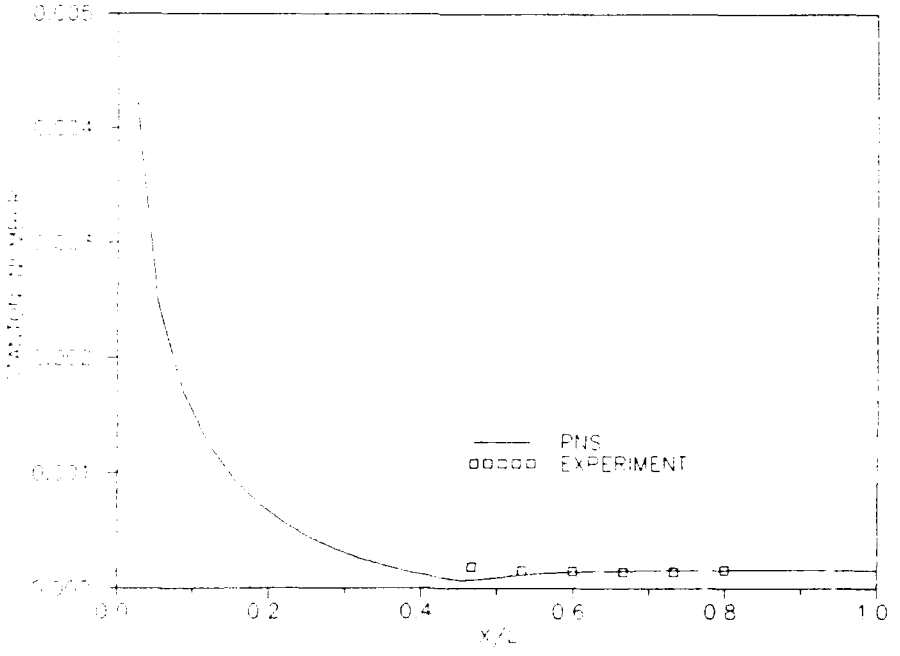

Figure 28. Stanton Number Comparison - Test Condition #2

ogive-cylinder, as shown by Figure 28. A better appreciation of the predictive capability of the code can be gained by considering a comparison of the code and data at each coaxial heat transfer gauge location in terms of the error range associated with the particular test condition. The average error for test condition #2 was 15.25 percent. Table 13 presents the comparison at each coaxial gauge location. With the exception of the first data point, all of the code values easily fall within the error range of the data.

Table 13. Local Stanton Number Comparisons - T/C #2

Coaxial Gauge #	Experimental St # ($x10^4$)	PNS Code St # ($x10^4$)
1	0.1575 to 0.2141	0.08182
2	0.1289 to 0.1753	0.1307
3	0.1253 to 0.1704	0.1482
4	0.1203 to 0.1636	0.1554
5	0.1214 to 0.1650	0.1587
6	0.1371 to 0.1865	0.1599

Figure 29 shows the same set of experimental data compared to PNS predictions from the mesh resolution study. This figure leaves little doubt that 120 radial grid points yields the best heat transfer results.

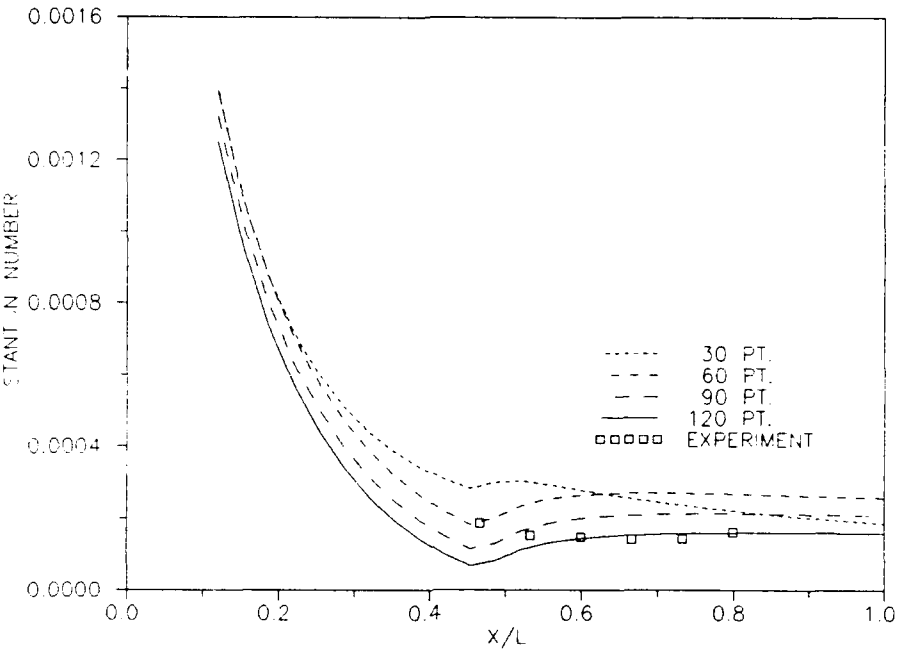

Figure 29. Stanton Number Comparison - Test Condition #2

The next test condition was treated first as a laminar flow and then as a turbulent flow with numerical models of both flow types generated. This was done because the free stream Reynolds number was 0.883×10^6 and typical transition Reynolds number values for flow over a flat plate were given as 0.35 to 0.5×10^6 (20:474). It was anticipated that transition might occur on the ogive-cylirder for test condition #3. Figure 30 shows the results of a comparison between the PNS code for a laminar model and a turbulent model. The two curves serve as upper and lower heat transfer bounds for the actual experimental data. When the experimental data were combined with the two models for comparison, the rather interesting results shown

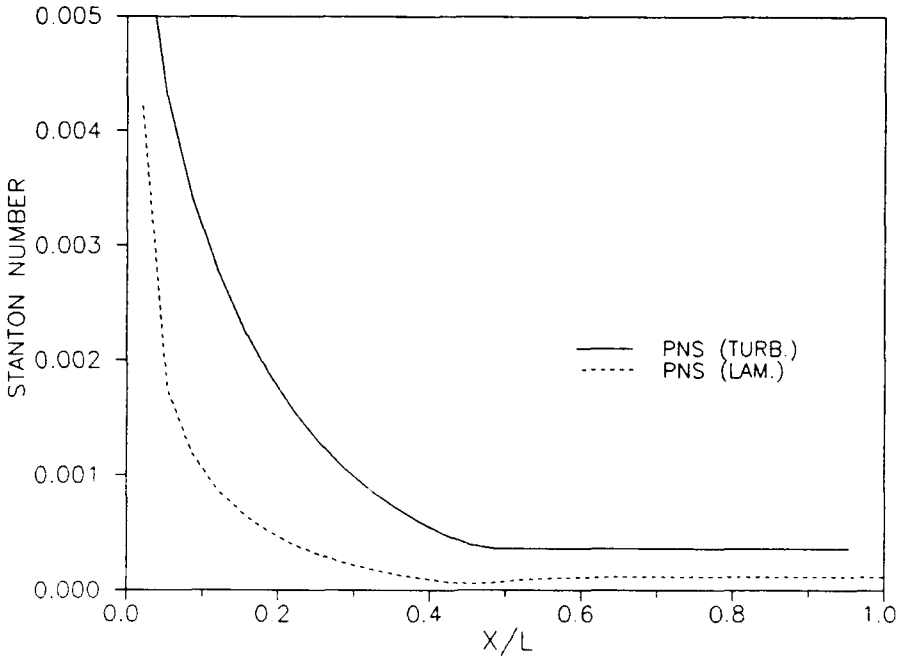

Figure 30. Comparison of PNS Predictions - T/C #3

in Figure 31 were obtained. These results suggest that the flow in test condition #3 was probably laminar over the ogive nose and transitioned to turbulent flow over the cylinder aft-body. The data appear to increase in Stanton number in the vicinity of x/L = 0.65 (9.75 inches from the nose). Although the PNS code does not have a transition model, it does have the capability to switch from laminar flow computations to turbulent computations at an axial location specified by the user. Given the results in Figure 31, an estimate for the transition point was obtained by inspection. The transition point value used was 9.3 inches or x/L = 0.62. When the code was run using the value XTRANS = 9.3, the results shown in Figure 32 were obtained. The

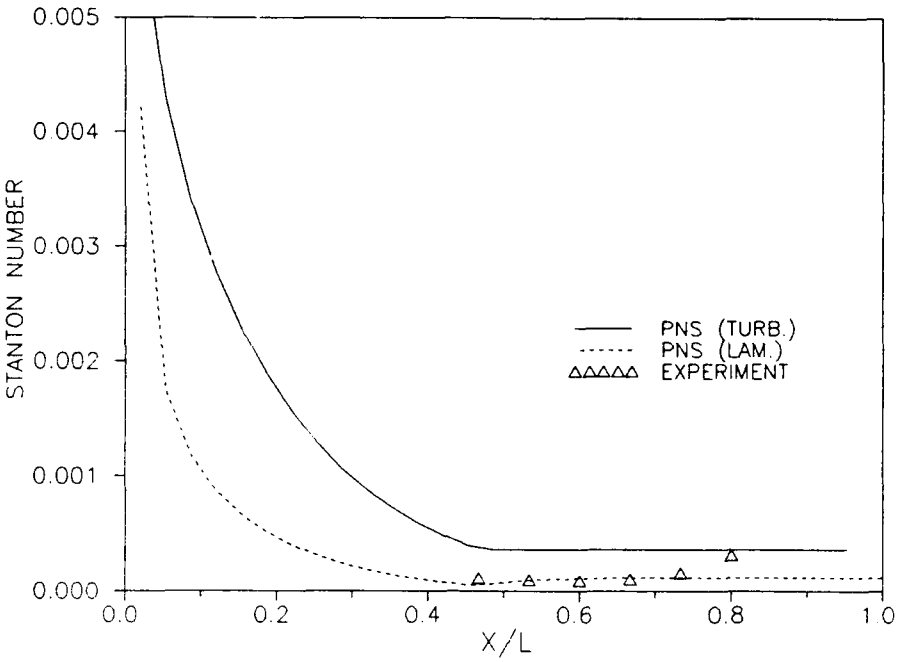

Figure 31. Stanton Number Comparisons - Test Condition #3

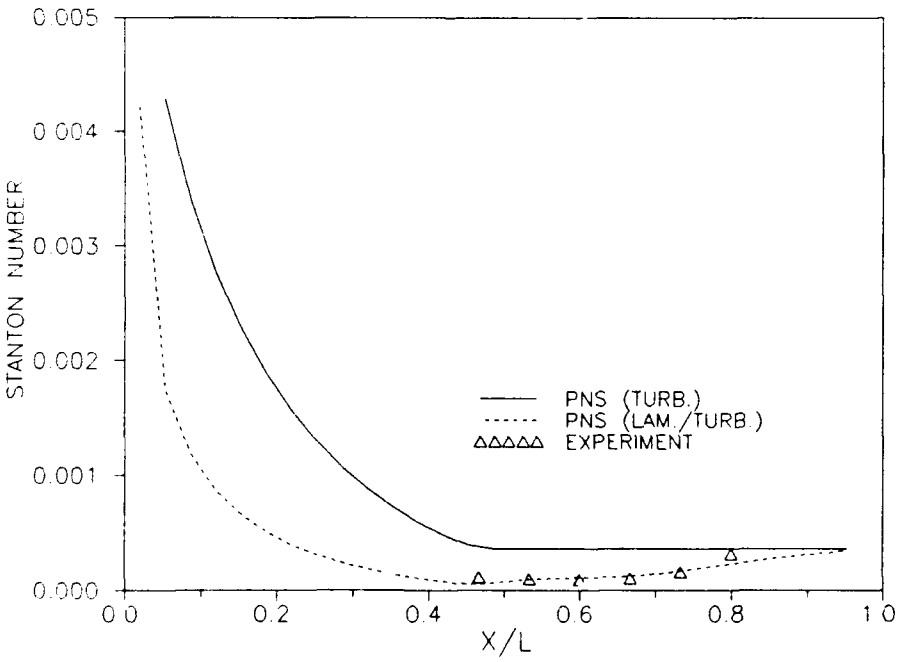

Figure 32. PNS Solution Using XTRANS Option - T/C #3

numerical simulation employing the local transition point produced good results and supports the presumption that transition probably occurred on the ogive-cylinder model downstream of the shoulder. No further attempts were made to improve the choice of XTRANS since such action was felt to be outside of the scope of the thesis objectives. The experimental data displayed in Figures 31 and 32 had an average error of ± 9.96 percent.

The code predictions for the turbulent flow of test condition #4 were compared to the data in Figure 33. The Stanton number prediction curve appears to be smoother in the vicinity of the shoulder than for the laminar cases. Figure 33 shows an average Stanton number of approximately 0.00045 with an error band of ± 8.79 compared to the PNS code. Although the code tends to under-predict the local Stanton number, the code and the data agree reasonably well. A point by point comparison is included in Appendix C.

The final test condition, #5, was a fully developed turbulent flow case. This case had the highest Reynolds number, 2.542×10^6, and also caused the most trouble in obtaining a converged starting solution. However, a solution was obtained and as can be seen in Figure 34, the PNS code predictions appear to agree very well with the experimental data. The average error was ± 8.69 percent and was also the lowest of the five test conditions. Table 14 presents the results of the comparison between the data and the code at the six coaxial heat transfer gauge locations.

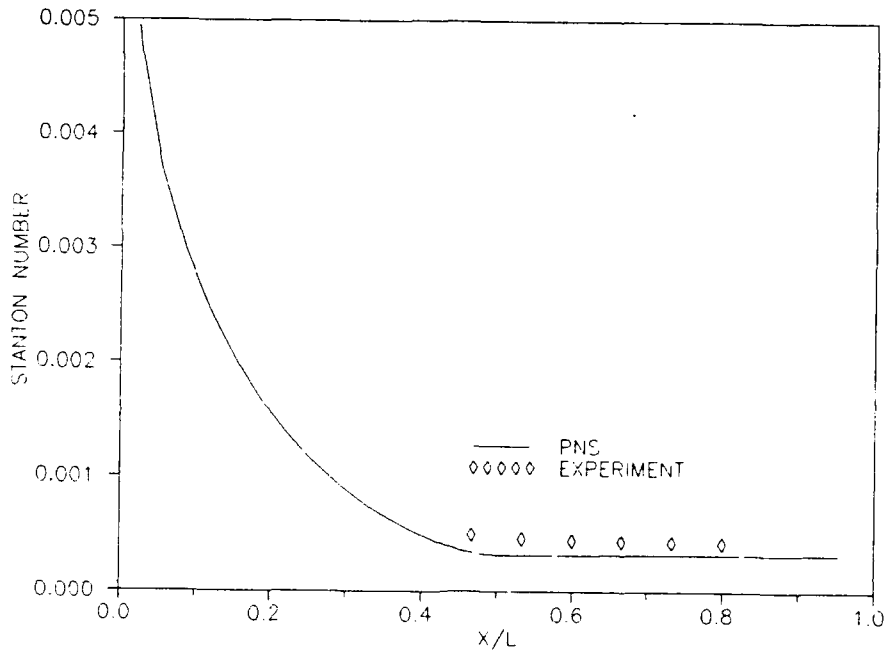

Figure 33. Stanton Number Comparisons - Test Condition #4

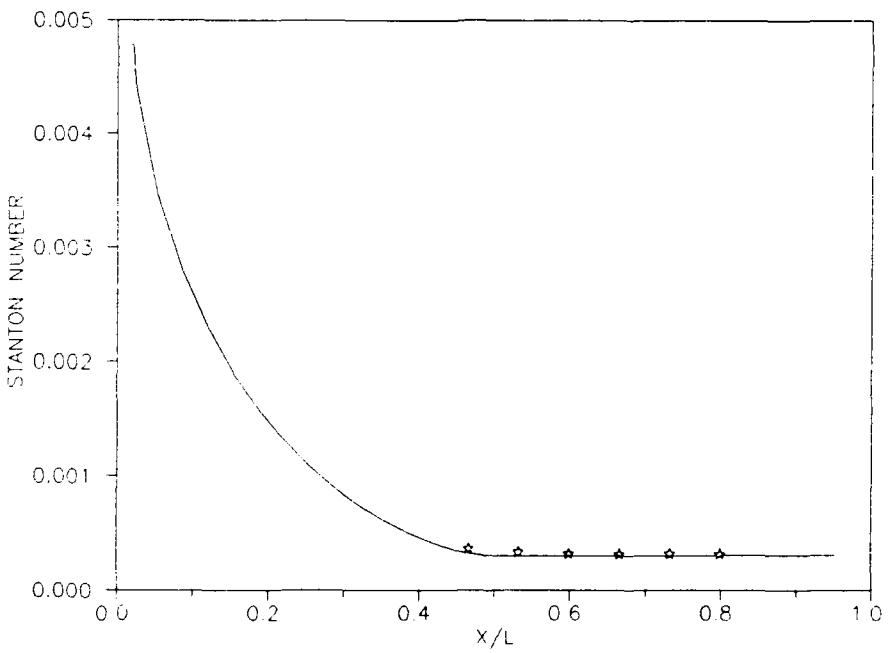

Figure 34. Stanton Number Comparisons - Test Condition #5

Table 14. Local Stanton Number Comparison - T/C #5

Coaxial Gauge #	Experimental St # ($\times 10^4$)	PNS Code St # ($\times 10^4$)
1	0.3360 to 0.4005	0.3068
2	0.3070 to 0.3657	0.3012
3	0.2940 to 0.3502	0.3019
4	0.2905 to 0.3458	0.3022
5	0.2930 to 0.3487	0.3029
6	0.2917 to 0.3470	0.3038

Excellent agreement between the local Stanton number and the PNS code predictions can be seen in Table 14. A similar comparison for the other cases can be found in Appendix C. Test condition #5 was also the turbulent case used in the mesh resolution study discussed in Chapter 4. Figure 35 shows the results from the study compared to the experimental data. Clearly, any of the LMAX values used in the numerical simulation would yield reasonable heat transfer results for this turbulent flow test condition.

A common characteristic of the PNS code was to under - predict the local Stanton number values for both laminar and turbulent flows. The tendency to predict a smaller Stanton number value was more obvious when comparing the code and data results given in Table 14 for the turbulent flow than for the laminar flow results given in Table 13. Figure 36

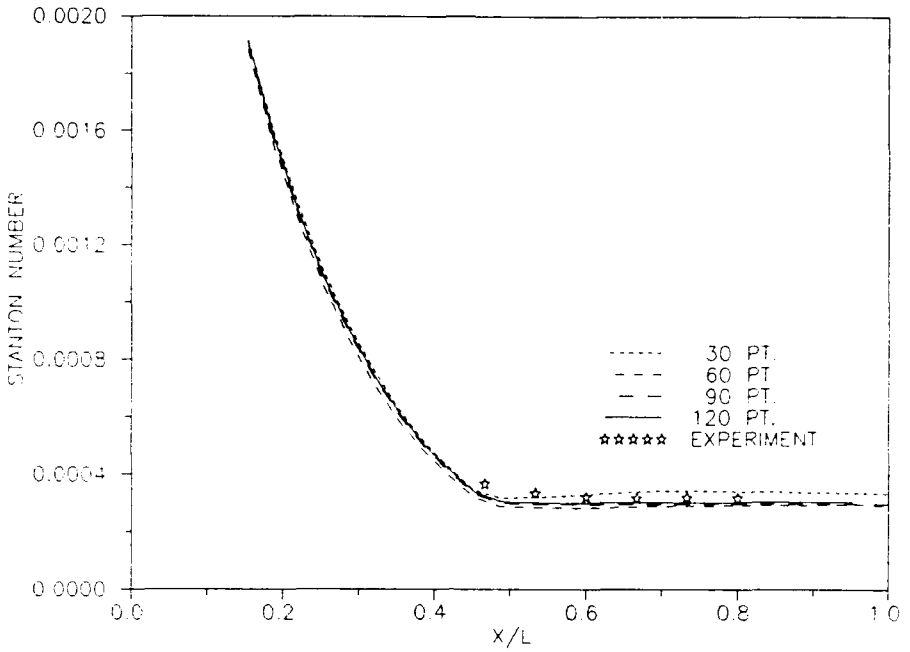

Figure 35. Stanton Number Comparison - Test Condition #5

addresses the question as to why the turbulent Stanton number values were on the lower side of the error band. In this figure, the heat flux prediction curves have been cropped to consider only the region where coaxial gauges are present on the model. The bottom curve corresponds to test condition #2 and has essentially the same profile as the local Stanton number curve given in Figure 28. Stanton number data also compared well with the PNS code predicted values for test condition #2. However, the top curve, corresponding to test condition #5, suggests that the larger predicted heat flux value should result in a larger predicted Stanton number compared to the data. This wasn't the case and a possible explanation lies in the experimental

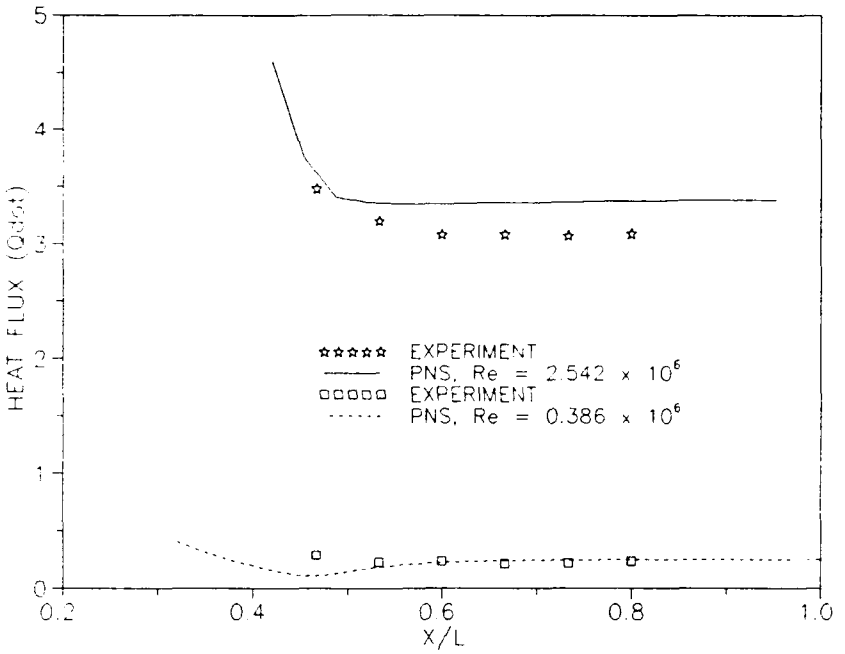

Figure 36. Heat Flux Comparison - T/C #2 and T/C #5

data. At the higher Reynolds numbers, the experimental data is perhaps more sensitive to the heat conducted axially through the body and its effects on the temperature gauges. Axial heat conduction increases the heat flux term in the experimental data, leading to potentially larger heat flux experimental values.

Figure 37 is a typical log-log plot of Stanton number versus local Reynolds number. All five sets of test conditions are presented in the figure. Close examination of the first two sets of data corresponding to test conditions #1 (circles) and #2 (squares) shows a gradual, upward shift in the data point at x/L = 0.8 as Reynolds number increases. The data for test condition #3,

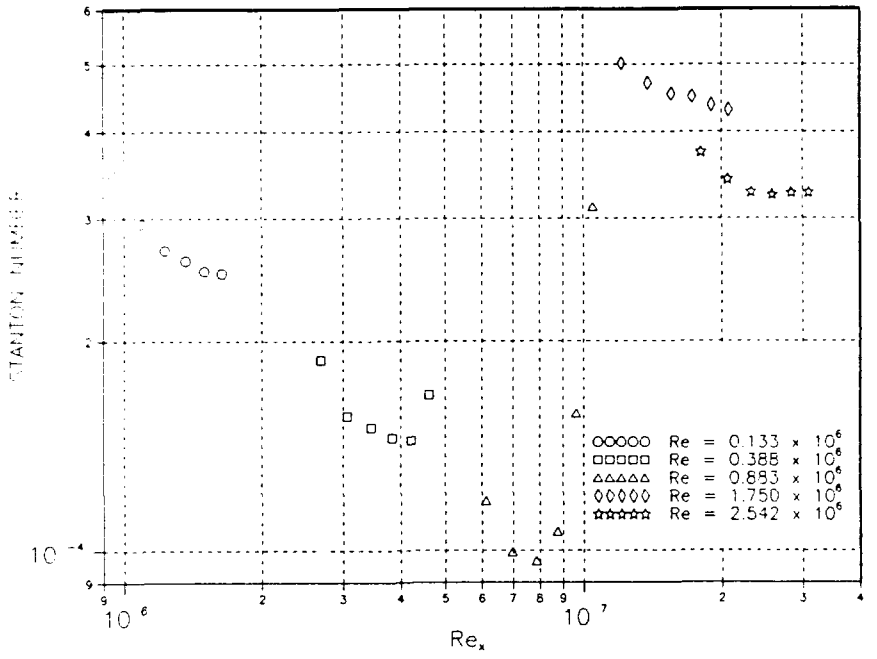

Figure 37. Stanton Number Versus Local Reynolds Number

represented by the triangles, strongly suggests that transition may have begun as far forward on the body as x/L = 0.6 and that the flow was approaching fully developed turbulent flow at the last axial location of x/L = 0.8. Test condition #4 (diamonds) and test condition #5 (stars) were fully developed turbulent flows and appear to be in the region where the last data point from test condition #3 was headed.

Overall, the PNS code predictions agreed very well with the experimental data for all test conditions considered. It appeared, however, that the PNS code had a tendency to under-predict heat transfer in the presence of an accelerating flow (favorable pressure gradient). This

statement is based on comparisons of the first and second data points for Figures 27 through 35. In each figure, the prediction curve dipped below the experimental data at the shoulder, but gradually increased until good agreement with the data was achieved. The gradual increase was probably due to the favorable pressure gradient giving way to a zero pressure gradient flow field on the cylinder aft-body. Finally, the PNS code performed well using the transition point option applied to test condition #3. With a little effort, the code could be made to model the experimental data for transition with very good results.

5.2.3 Skin Friction. The PNS code predictions for skin friction compared well with the sparse experimental data. Only one skin friction coefficient was available for each test condition and it was taken at x/L = 0.783 (11.75 inches from the nose). Figure 38 shows the comparison for test condition #1. The error band for the data point is ± 8.72 percent and a reasonably good agreement exists between the code and the data. Numerical comparisons between the code prediction and the data for each test condition is given in Table 15. Figure 39 has the same general profile as the previous figure and the experimental data point lies very nearly on the prediction curve. The error band for this data point is ± 8.05 percent. Very good agreement exists for the code prediction of skin friction on the cylindrical aft-body for test condition #2. In both test conditions #1 and #2, the PNS code predicted local skin

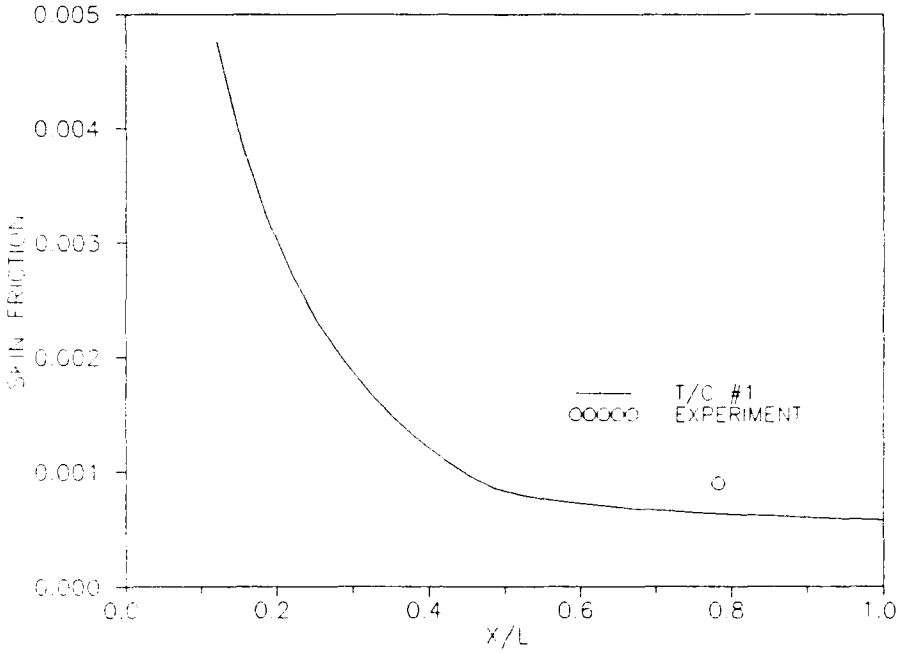

Figure 38. Skin Friction Comparison - Test Condition #1

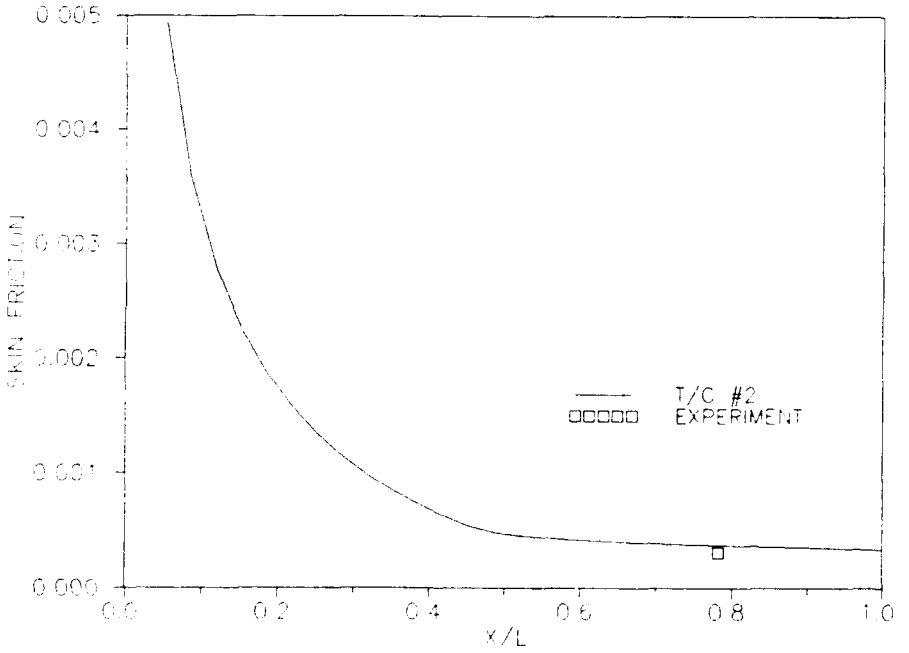

Figure 39. Skin Friction Comparison - Test Condition #2

friction coefficient for a laminar flow.

The agreement between data and the prediction curve is not so good for test condition #3 as shown in Figure 40. This test condition was modeled as a laminar flow and, as was established in the previous section, transition to turbulent flow had probably occurred upstream of this data point. Figure 41 shows the same data point compared to the code prediction curve using the transition option. The agreement is better than before, but is still not very good. This data point had an error band of ± 4.48 percent and is compared to the prediction curve in Table 15. The last skin friction comparison, Figure 42, also shows very good agreement between the code prediction and the data point. The error band for this case is ± 3.63 percent. A better feel for how well the code compared to the data points is gained from the results in Table 15. Experimental data for test condition #5 was not available. The results from Table 15 show good agreement for a laminar case, T/C #2, and a

Table 15. Skin Friction Comparisons

T/C #	C_f - Exp. (x 1000)	C_f - PNS (x 1000)
1	0.8260 to 0.9729	0.6368
2	0.2847 to 0.3345	0.3721
3 (L)	1.0946 to 1.1973	0.2589
3 (L-T)	1.0946 to 1.1973	0.4221
4	0.7957 to 0.8554	0.7191

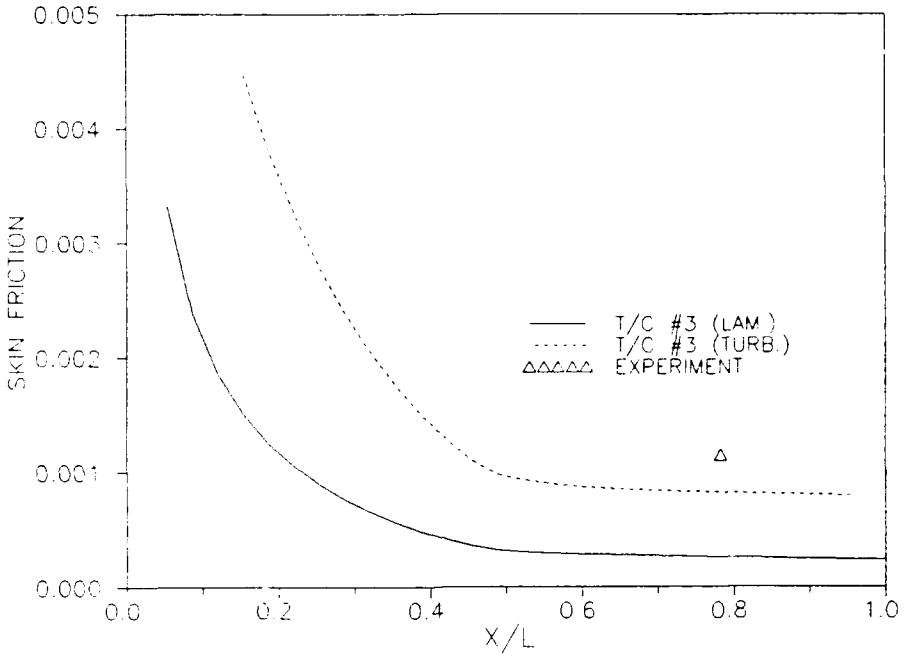

Figure 40. Skin Friction Comparison - Test Condition #3

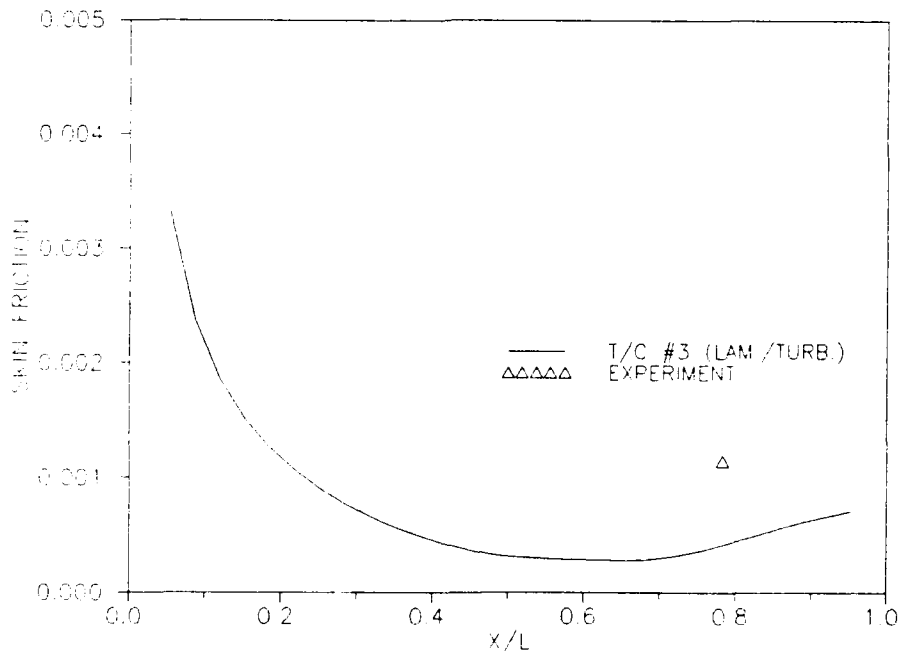

Figure 41. Skin Friction Using XTRANS Option - T/C #3

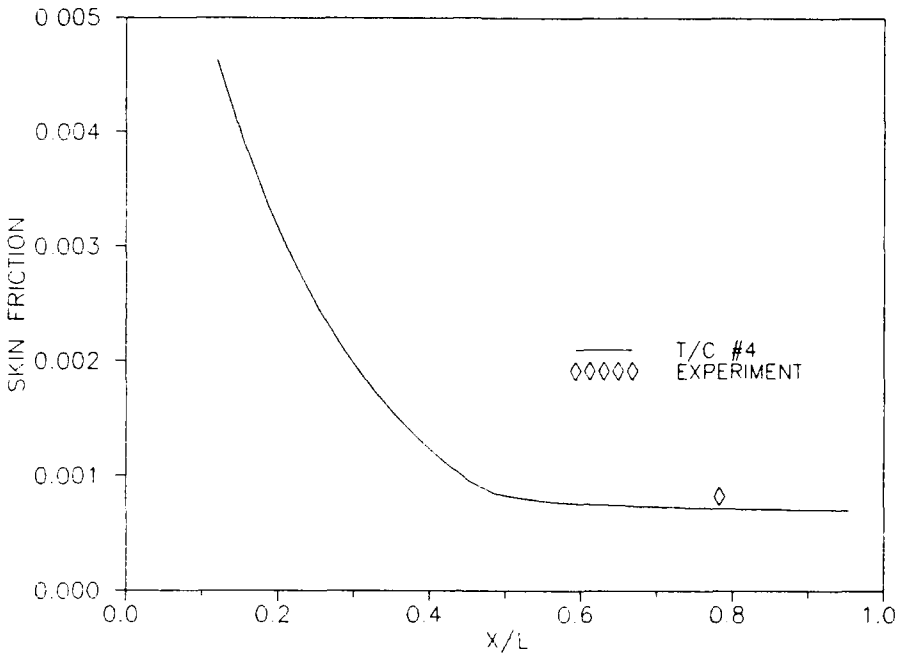

Figure 42. Skin Friction Comparison - Test Condition #4

turbulent case, T/C #4, but poor agreement for the other two cases which happen to be a laminar and a turbulent case also. It is difficult to make a general conclusion about the skin friction data with regards to the predicted results based on a single data point for each test condition. The data appears to be reasonable, in a qualitative sense, based on Figure 43. The general trend in the laminar data and the turbulent data is consistent with general skin friction coefficient versus Reynolds number curves found in the literature (11:400). However, at best, Figure 43 only implies that the trend in the experimental data is reasonable.

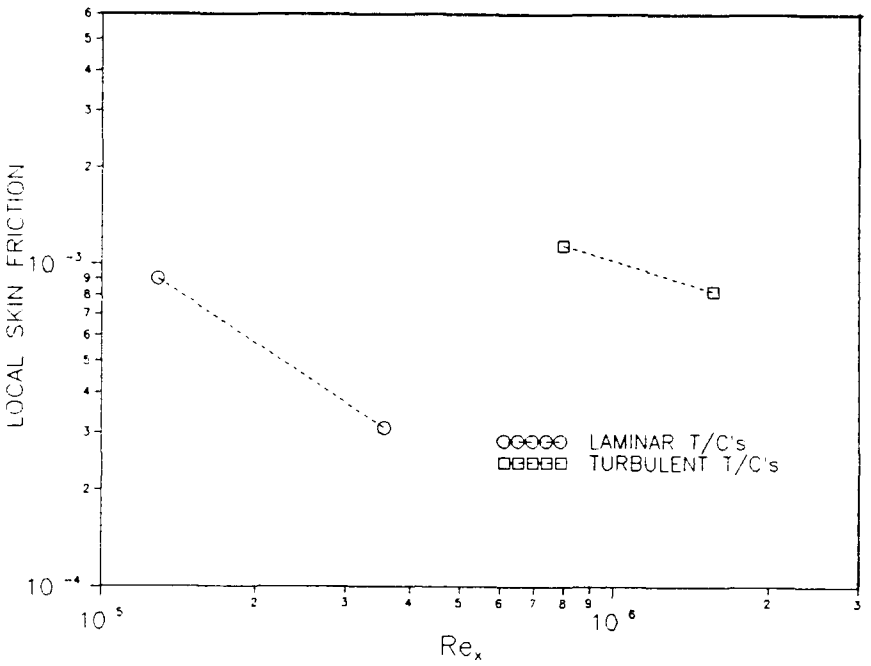

Figure 43. Skin Friction Versus Local Reynolds Number

VI. CONCLUSIONS AND RECOMMENDATIONS

6.1 Conclusions

The hypersonic, viscous flow over an ogive-cylinder body at zero angle of attack was studied using the WRDC/FIMG PNS code. Five sets of flow conditions were investigated ranging from low Reynolds number, laminar flow, to high Reynolds number, fully developed turbulent flow. Included in the investigation was a flow situation in which the laminar flow boundary layer transitioned to a turbulent flow boundary layer on the body. A parametric study was also conducted on selected input variables to determine their effect on heat transfer and skin friction results. Once satisfied with the PNS results, comparisons were made between the computational results and the experimental data for similar flow conditions. The following conclusions summarize the thesis results in light of the objectives stated in Chapter 1:

1. PNS starting and marching solutions were obtained for the test conditions investigated using the WRDC/FIMG PNS code. The PNS code required meticulous selection of the input variables and improper choices resulted in either unstable solutions or nonphysical answers. A very large amount of user time and "fine-tuning" of the input variables was necessary to obtain accurate solutions. This was especially true for the high Reynolds number turbulent flows. For instance, one particular turbulent case required

27 attempts just to obtain the starting solution.

The heat transfer and skin friction results were determined to be reasonable based on the satisfactory resolution of the temperature and velocity gradients at the surface. The first point away from the surface was either 5 x 10^{-5} inches, for the laminar cases, or 1 x 10^{-5} inches for the turbulent cases. Numerical smoothing was maintained at a reasonably small value of 0.1 for SMU and 0.2 for SMUIM for all cases.

2. The parametric study revealed that several of the input variables could be varied slightly without any appreciable change in Stanton number or skin friction coefficient. However, choice of location for the first radial grid point, DS, did have a significant influence on heat transfer and skin friction results. Small changes in DS caused large variations in the heat transfer on the ogive nose, the region of highest heat transfer. The laminar flows were more sensitive to the number of radial grid points used than were the turbulent flows. The thermal and velocity gradients were easier to resolve for the turbulent boundary layers than for the laminar boundary layers.

3. Experimental data were generated for the same flow conditions used in the numerical simulations. Comparisons were made between the data and the PNS predictions for surface pressure ratio, local Stanton number and local skin friction coefficient. A discussion of these comparisons follows:

a. Surface Pressure Ratio. All of the surface pressure results compared very well. The PNS code tended to slightly over-predict surface pressures in the region of accelerating flow along the ogive nose. This tendency occurred in all test cases and could probably be attributed to one or more of the following reasons: (i) the influence of the cone approximation used in the starting solution, (ii) the contribution of both fractions of the streamwise pressure gradient present when using the modified Vigneron sublayer model, and (iii) the occurrence of flow acceleration near the surface due to elevated sublayer temperatures resulting from axial heat conduction in the model. This last reason addresses why the predicted results, subject to a constant surface temperature condition in the PNS code, are higher than the experimental data. The tendency for surface pressure over-prediction diminished along the cylinder aft-body in conjunction with a decrease in the contribution of the above mentioned reasons.

b. Stanton Number. Stanton number data was provided at six axial locations along the cylinder aft-body with the first data station located at the shoulder. Stanton number predictions for the laminar cases compared well with the data except for the region immediately behind the shoulder. In this region of accelerating flow, the code under-predicted the Stanton number for probably the same reasons mentioned in part (a) above. In particular, application of the Vigneron splitting technique to the

streamwise energy equation resulted in an additional heat transfer term and this additional term could have a significant effect on the local heat flux and hence, local Stanton number prediction. The Stanton number predictions for the turbulent cases also compared well with the experimental data. The turbulent prediction curves did not have the dip at the shoulder characteristic of the laminar curves. The data for test condition #3 suggested that laminar to turbulent boundary layer transition occurred on the cylinder aft-body in the vicinity of the shoulder. The PNS code was able to model this result after it was observed in the experimental data that transition had probably occurred. Except for the transition case (T/C #3), all of the PNS solutions were obtained prior to getting the experimental data. This prevented judicious tinkering of the code input variables in an effort to manipulate better agreement between the code predictions and the data. Finally, it should be noted that no changes were made to the constants used in the turbulence model, although the conditions for which they were derived were probably very much different than the conditions investigated.

c. Skin Friction. The skin friction results were classified as reasonable. Only one data point was obtained for each case and the data compared well for one laminar case (T/C #2) and one turbulent case (T/C #4). It did not compare as favorably for the remaining two laminar cases, although T/C #3 was probably turbulent at the point where

the skin friction measurement was taken.

4. The WRDC/FIMG PNS code performed well in predicting surface pressure ratios and local Stanton numbers for the flow conditions considered over the ogive-cylinder body. Furthermore, the skin friction results were consistent in trend and reasonable in magnitude. Therefore, these results validate the use of the WRDC/FIMG PNS code for the flow conditions and geometry considered. In addition, the reasonable comparisons between heat transfer and skin friction predictions and the experimental data suggest that the physics involved have been adequately modeled by the PNS code numerical formulations.

6.2 Recommendations

The areas recommended for further study can be divided into two categories: PNS code improvements and PNS code applications.

Recommendations for additional research directed towards improving the WRDC/FIMG PNS code are:

1. Thoroughly investigate the case of transition that probably occurred for T/C #3 by closely examining the temperature, velocity and heat flux data. Attempt to predict the experimental results using the XTRANS option in the PNS code and develop an applicable transition model based on the relaxation technique for use in the PNS code.

2. Thoroughly examine the starting solution methodology to establish a quicker and more reliable method of obtaining starting solutions required to initiate the

marching solution.

3. Modify the existing WRDC/FIMG PNS code to make it an interactive code instead of a batch code. Improve the storage of output data to streamline analyses. Provide interactive graphics to zero-in on particular output data for immediate visualization. Create output data files for collecting flow field results or surface results.

Recommendations for additional research directed towards application of the WRDC/FIMG PNS code are:

1. Conduct a rigorous parametric study on the input variables (DS, IDPDX, PER, EPSA, EPSB, DX, SMU, SMUIM, and LMAX) that influence surface flow conditions and predicted results. Explore the inter dependency of the parameters.

2. Consider running the PNS code for the ogive-cylinder at an angle of attack. Angle of attack data exists for several different flow conditions. Examine the occurrence of crossflows and the onset of streamwise flow separations with increasing angle of attack.

3. Modify the existing ogive-cylinder model with additional coaxial heat transfer gauges along the ogive nose to collect data in the region of highest heat transfer and in the presence of a favorable pressure gradient. Attempt to determine the cause of the over-prediction of surface pressure along the nose and the under-prediction of local Stanton number at the shoulder. Heat transfer and skin friction results for hypersonic flows over an ogive nose are of particular interest to the Advanced Medium Range

Air-to-Air Missile Program Office and could be of value in the design of radomes for future high speed missiles.

Bibliography

1. Anderson, Dale A., John C. Tannehill, and Richard H. Pletcher. *Computational Fluid Mechanics and Heat Transfer.* Series in Computational Methods in Mechanics and Thermal Sciences. New York: Hemisphere Publishing Corporation, 1984.

2. Anderson, John D. Jr. *Hypersonic and High Temperature Gas Dynamics.* Series in Aeronautical and Aerospace Engineering. New York: McGraw-Hill Book Company, 1989.

3. Baldwin, B. S. and H. Lomax. "Thin Layer Approximation and Algebraic Model for Separated Turbulent Flows." *AIAA 16th Aerospace Sciences Meeting.* AIAA-78-257 (January 1978).

4. Bertin, John J. and Michael L. Smith. *Aerodynamics for Engineers.* Englewood Cliffs, New Jersey: Prentice-Hall, Inc., 1979.

5. Cebeci, T. "Calculation of Compressible Turbulent Boundary Layers With Heat and Mass Transfer," *AIAA 3rd Fluid and Plasma Dynamics Conference.* AIAA-70-741, June 1970.

6. Chaussee, Denny S. "NASA Ames Research Center's Parabolized Navier-Stokes Code: A Critical Evaluation of Heat-Transfer Predictions," *AIAA 22nd Thermophysics Conference.* AIAA-87-1474 (June 1987).

7. Hemsch, Michael J. and Jack N. Nielsen. *Tactical Missile Aerodynamics.* Progress in Astronautics and Aeronautics, Vol. 104. New York: American Institute of Aeronautics and Astronautics, 1986.

8. Incropera, Frank P. and David P. DeWitt. *Introduction to Heat Transfer.* New York: John Wiley and Sons, 1985.

9. Kaul, U. K. and D. S. Chaussee. *"AFWAL Parabolized Navier-Stokes Code: 1983 AFWAL/NASA Merged Baseline Version,"* AFWAL-TR-83-3118, Air Force Wright Aeronautical Laboratories, Wright-Patterson Air Force Base, Ohio, May 1984.

10. Krasnov, Nikolai F. *Aerodynamics of Bodies of Revolution.* New York: American Elsevier Publishing Company, Inc., 1970.

11. Kuethe, Arnold M. and Chuen-Yen Chow. *Foundations of Aerodynamics: Bases of Aerodynamic Design* (Third Edition). New York: John Wiley and Sons, 1976.

12. McWherter, M., R. W. Noack and W. L. Oberkampf. "Evaluation of Inviscid/Boundary Layer and Parabolized Navier-Stokes Solutions for Design of Reentry Vehicles," *AIAA 22nd Aerospace Sciences Meeting.* AIAA-84-0486 (January 1984).

13. Molten, Capt Randy G. *"Expansion of the Aerodynamic Simulation Capabilities of the Air Force WRDC Mach 6 High Reynolds Number Facility,"* WRDC-TM-89-173-FIMG, Flight Dynamics Laboratory, Wright Research and Development Center, Wright-Patterson Air Force Base, Ohio, August 1989.

14. Neumann, R. D. and J. L. Patterson. "Results of an Industry Representative Study of Code to Code Validation of Axisymmetric Configurations at Hypervelocity Flight Conditions," *AIAA Thermophysics, Plasmadynamics and Lasers Conference.* AIAA-88-2691 (June 1988).

15. Patterson, Jerold L. and E. Brown-Edwards. *AFWAL PNS Code.* Private communication. HQ WRDC, Wright-Patterson AFB OH, July - September, 1990.

16. Rakich, J. V., Y. C. Vigneron and R. Agarwal. "Computation of Supersonic Viscous Flows Over Ogive-Cylinders at Angle of Attack," *AIAA 17th Aerospace Sciences Meeting.* AIAA-79-0131 (January 1979).

17. Scaggs, N. E., L. Galassi and J. Leugers. *"Heat Transfer and Skin Friction Measurements for a Favorable Pressure Gradient,"* WRDC-TM-90-335-FIMG, Flight Dynamics Laboratory, Wright-Patterson AFB OH, December 1990.

18. Schiff, L. B. and J. L. Steger. "Numerical Simulation of Steady Supersonic Viscous Flow," *AIAA 17th Aerospace Sciences Meeting.* AIAA-79-0130 (January 1979).

19. Schiff, L. B. and W. B. Sturek. "Numerical Simulation of Steady Supersonic Flow Over an Ogive-Cylinder-Boattail Body," *AIAA 18th Aerospace Sciences Meeting.* AIAA-80-0066 (January 1980).

20. Schlichting, Hermann. *Boundary-Layer Theory* (Seventh Edition). New York: McGraw-Hill Book Company, 1979.

21. Stalnaker, J. F. and others. *"Improvements To The AFWAL Parabolized Navier-Stokes Code Formulation."* AFWAL-TR-86-3076, Air Force Wright Aeronautical Laboratories, Wright-Patterson Air Force Base, Ohio, September 1986.

APPENDIX A. OGIVE NOSE GEOMETRY

An expression was needed for the ogive nose radius as a function of the axial location, since it was necessary to be able to define the surface location along the ogive nose at each axial marching plane. Therefore, the radius R was needed as R(x). The following figure defines the x-R coordinate system and the ogive arc which defines the body surface.

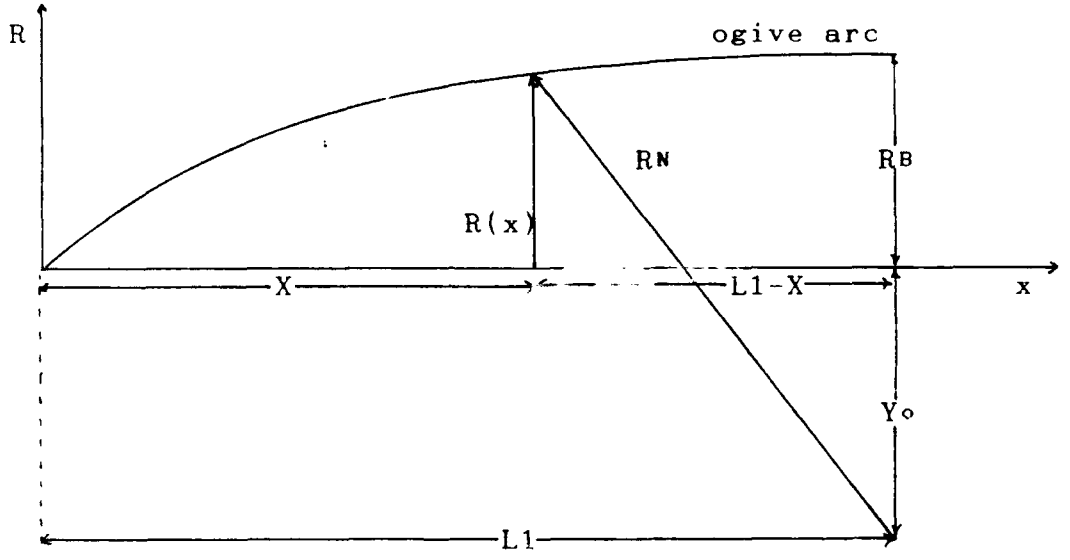

Figure A.1. Ogive Radius Function Geometry (10:20-22)

From the definition of a right triangle,

$$(Y_o + R)^2 + (L1 - X)^2 = R_N^2 = Y_o^2 + L1^2 \qquad (A.1)$$

which simplifies to

$$R^2 + 2Y_oR - 2XL1 + X^2 = 0 \qquad (A.2)$$

and yields a value for R of:

$$R = -Y_o \pm [Y_o^2 - X^2 + 2XL1 + (L1^2 - L1^2)]^{1/2} \qquad (A.3)$$

Making use of the relation, $X^2 - 2XL1 + L1^2 = (X - L1)^2$, the expression given in Eq (A.3) can be simplified to

$$R = -Y_o + [R_N^2 - (X - L1)^2]^{1/2} \qquad (A.4)$$

where $R_N^2 = Y_o^2 + L1^2$. Now, substituting in the value of Y_o given as $Y_o = R_N - R_B$, Eq (A.4) becomes:

$$R = R_B - R_N + [R_N^2 - (X - L1)^2]^{1/2} \qquad (A.5)$$

Since R_N may not be specified, Eq (A.5) can be modified to remove the dependence on the value of R_N. For instance

$$R_N^2 = Y_o^2 + L1^2 = (R_N - R_B)^2 + L1^2$$

$$= R_N^2 - 2R_NR_B + R_B^2 + L1^2 \qquad (A.6)$$

$$\therefore \quad R_N = (R_B^2 + L1^2)/(2R_B) \qquad (A.7)$$

An expression for R(x) can now be written as

$$R(x) = R_B - \left[\frac{R_B^2 + L1^2}{2R_B}\right] + \left[\frac{(R_B^2 + L1^2)^2}{4R_B^2} - (X - L1)^2\right]^{1/2} \qquad (A.8)$$

Eq (A.8) can be verified by evaluating the equation at the endpoints of the ogive arc. Evaluate Eq (A.8) at the

origin, where x = 0 and R(x) = 0

$$R(x) = 0 = R_B - \left[\frac{R_B^2 + L1^2}{2R_B}\right] + \left[\frac{(R_B^2 + L1^2)^2}{4R_B^2} - L1^2\right]^{1/2} \quad (A.9)$$

Lable each term in Eq (A.9) as T1, T2 and T3 respectively, therefore, simplifying term T3 becomes

$$T3 = \left[\frac{R_B^4 + 2R_B^2L1^2 + L1^4 - 4R_B^2L1^2}{4R_B^2}\right] = \frac{R_B^2 + L1^2}{2R_B} \quad (A.10)$$

$$T2 + T3 = \left[\frac{R_B^2 + L1^2}{2R_B}\right] + \left[\frac{R_B^2 - L1^2}{2R_B}\right] = R_B \quad (A.11)$$

Therefore, T1 - (T2 + T3) yields

$$R_B - (R_B) = 0 \quad (A.12)$$

The results from Eq (A.12) indicates that Eq (A.8) yields the correct value at the origin. Now, evaluate Eq (A.8) at the shoulder of the ogive arc where x = L1 and R(x) = R_B.

$$R(x) = R_B = R_B - \left[\frac{R_B^2 + L1^2}{2R_B}\right] + \left[\frac{(R_B^2 + L1^2)^2}{4R_B^2}\right]^{1/2} \quad (A.13)$$

$$R_B = R_B - \left[\frac{R_B^2 + L1^2}{2R_B}\right] + \left[\frac{R_B^2 + L1^2}{2R_B}\right] \quad (A.14)$$

$$\therefore R_B = R_B \quad (A.15)$$

Eq (A.15) indicates that Eq (A.8) yields the correct value of R(x) at the shoulder. Finally, Eq (A.8) should also

yield the result that the slope of R(x) is zero at the shoulder. The slope is given by

$$\frac{dR}{dx} = (L1 - x)\left[\frac{(R_B^2 + L1^2)^2}{4R_B^2} - (x - L1)^2\right]^{-1/2} \qquad (A.16)$$

When a value of x = L1 is substituted into Eq (A.16), the correct result of $\left.\frac{dR}{dx}\right|_{x=L1} = 0$ is obtained. The expression given by Eq (A.8) for the ogive surface checks at both the origin and the shoulder. Furthermore, Eq (A.8) verifies that the geometry is definitely a tangent ogive. This equation provides a value for the ogive radius as a function of x from the nose to the junction of the ogive with the cylindrical aft-body at the shoulder.

The starting solution requires definition of a nose cone to fix the shock location relative to the body. Two primary input values needed for the conical solution are XOS and SIGMA. Both are described below.

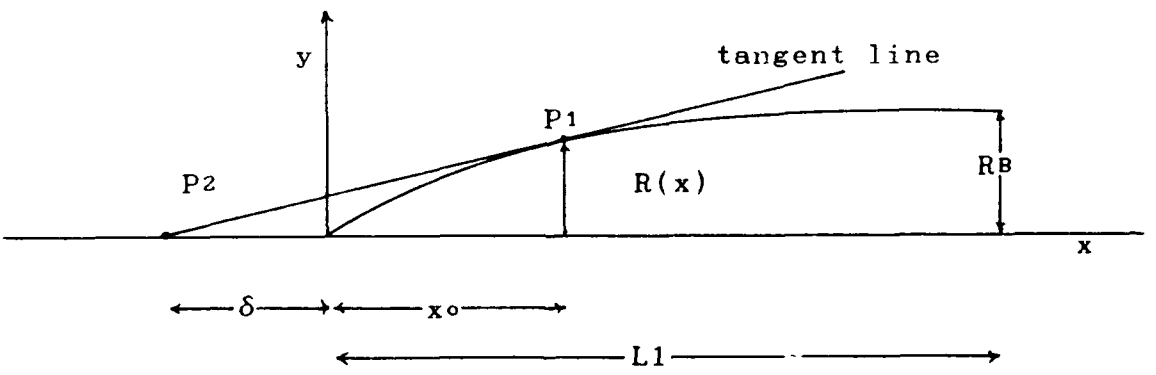

Figure A.2. Ogive nose cone geometry

The slope of the tangent line is given by Eq (A.16) as

$$Rp(x) = \frac{dR}{dx} = (L1 - x)\left[\frac{(RB^2 + L1^2)^2}{4RB^2} - (x - L1)^2\right]^{-1/2} \qquad (A.17)$$

At $x = x_o = 0.3$, $R(x_o) = 0.131318$. The slope at point P1 where $P1 = (0.3, 0.131318)$ is $Rp(P1) = 0.42635$. The value for δ, the distance from the origin to the point where the tangent line intercepts the x axis, can be determined from manipulation of the slope expression, Equation A.17. The value for δ is assigned to the PNS code variables XOS and XOB in the geometry definition group. Having chosen a value for x_o, the nose cone length, of $x_o = 0.3$ inches, determine δ from the two-point slope formula:

$$y1 - y2 = m(x1 - x2) \qquad (A.18)$$

Let $m = Rp(P1)$ and $x2 = \delta$ to define points P1 and P2 from Figure A.2 in equation A.18 as:

$$x1 = x_o = 0.3 \qquad x2 = \delta$$
$$y1 = R(x_o) = 0.131318 \qquad y2 = 0.0$$

$$\therefore \quad \delta = x1 - [(y1 - y2)/Rp(P1)] \qquad (A.19)$$

For the ogive geometry described above, $\delta = -0.008003$. It is now possible to determine the major cone half angle, SIGMA.

$$SIGMA = \tan^{-1}\left[\frac{R(x_o)}{x_o + |\delta|}\right] \qquad (A.20)$$

After substituting in the known values of x_o, δ, and $R(x_o)$, a value for SIGMA of 23.091 degrees was obtained. This was the value used in all starting solutions for the major cone half angle.

APPENDIX B. PNS CODE INPUT FILES

Table B.1 contains the integer variables for the starting solution input file OGISBIN.

Table B.1. Integer Input Variables for OGISBIN

VARIABLE	T/C #1	T/C #2	T/C #3	T/C #4	T/C #5
JS	0	0	0	0	0
JMAX	0800	0800	0800	0800	0800
KMAX	19	19	19	19	19
LMAX	060	060	060	060	060
IBODY	0	0	0	0	0
ICONIC	1	1	1	1	1
ICROSS	0	0	0	0	0
ICYL	1	1	1	1	1
IDAPT	0	0	0	0	0
IDPDX	3	3	3	1	1
IFIT	1	1	1	1	1
IFORM	1	1	1	1	1
IGRID	0	0	0	0	0
IHYBRD	0	0	0	0	0
INCHES	1	1	1	1	1
INVIS	0	0	0	0	0
IPER	0	0	0	0	0
IPRT	1	1	1	1	1
IRAY	-1	-1	-1	-1	-1
IREAL	0	0	0	0	0
ISEG	0	0	0	0	0
ISLIP	1	1	1	1	1
ISMTH	0	0	0	0	0
ISPLIN	0	0	0	0	0
ISTEP	0	0	0	0	0
ISTORE	0500	0500	0500	0500	0500
ISTRCH	0	0	0	0	0
KPRT	19	19	19	19	19
LADD	6	6	6	6	6
LAMIN	-1	-1	-1	0	0
LBLP	045	045	045	045	045
METHOD	0	0	0	1	1
METRC	0	0	0	0	0
MOMENT	0	0	0	0	0
NCNBR	0	0	0	0	0
NPOINT	0	0	0	0	0
NPRTBB	350	350	350	350	350
NPRTBL	350	350	350	350	350
NPRTFF	350	350	350	350	350
NPRTSL	350	350	350	350	350
NXPRT	0	0	0	0	0

Table B.2 contains the real input variables used for the starting solution input file OGISBIN.

Table B.2. Real Input Variables for OGISBIN

VARIABLE	T/C #1	T/C #2	T/C #3	T/C #4	T/C #5
ZOB	0.0	0.0	0.0	0.0	0.0
X	0.3	0.3	0.3	0.3	0.3
DX	0.01	0.01	0.01	0.01	0.01
CNBR	0.0	0.0	0.0	0.0	0.0
XEND	15.0	15.0	15.0	15.0	15.0
DS	+0.00005	+0.00005	+0.00001	+0.00001	+0.00001
SMU	0.20	0.20	0.20	0.20	0.20
SMUIM	0.40	0.40	0.40	0.40	0.40
EPSA	0.50	0.50	0.50	1.00	1.00
EPSB	0.50	0.50	0.50	1.00	1.00
ALPHA	0.0	0.0	0.0	0.0	0.0
BETA	0.0	0.0	0.0	0.0	0.0
FSMACH	5.76	5.78	5.79	5.86	5.90
GAMMA	1.4	1.4	1.4	1.4	1.4
RE	133333.3	387500.0	883333.3	1750000.	2541667.
TINF	128.9	128.9	128.9	128.9	128.9
TWALL	560.0	560.0	560.0	560.0	560.0
DQINF	0.0	0.0	0.0	0.0	0.0
XTRANS	0.0	0.0	0.0	0.0	0.0
PER	0.0	0.0	0.0	0.0	0.0
PERMIN	0.0	0.0	0.0	0.0	0.0
PERMAX	0.0	0.0	0.0	0.0	0.0
DSYPLUS	0.0	0.0	0.0	0.0	0.0
CHI1	46.0	46.0	46.0	46.0	46.0
CHI2	46.0	46.0	46.0	46.0	46.0
AOVERB	1.0	1.0	1.0	1.0	1.0
SIGMA	23.0910	23.0910	23.0910	23.0910	23.0910
XOB	-0.008	-0.008	-0.008	-0.008	-0.008
XOS	-0.008	-0.008	-0.008	-0.008	-0.008
AB	0.0	0.0	0.0	0.0	0.0
ALENGT	0.0	0.0	0.0	0.0	0.0
DIAB	0.0	0.0	0.0	0.0	0.0
SAX	0.0	0.0	0.0	0.0	0.0
SN	0.0	0.0	0.0	0.0	0.0
SS	0.0	0.0	0.0	0.0	0.0
SMPP	0.0	0.0	0.0	0.0	0.0
SMR	0.0	0.0	0.0	0.0	0.0
SMY	0.0	0.0	0.0	0.0	0.0
XCG	0.0	0.0	0.0	0.0	0.0
XREF	0.0	0.0	0.0	0.0	0.0

Table B.3 contains the integer input variables used for the marching solution input file OGIVIN.

Table B.3. Integer Input Variables for OGIVIN

VARIABLE	T/C #1	T/C #2	T/C #3	T/C #4	T/C #5
JS	0	0	0	0	0
JMAX	1500	1500	1500	1500	1500
KMAX	19	19	19	19	19
LMAX	120	120	120	120	120
IBODY	0	0	0	0	0
ICONIC	0	0	0	0	0
ICROSS	0	0	0	0	0
ICYL	1	1	1	1	1
IDAPT	0	0	0	0	0
IDPDX	3	3	3	3	3
IFIT	1	1	1	1	1
IFORM	1	1	1	1	1
IGRID	0	0	0	0	0
IHYBRD	0	0	0	0	0
INCHES	1	1	1	1	1
INVIS	0	0	0	0	0
IPER	0	0	0	0	0
IPRT	1	1	1	1	1
IRAY	-1	-1	-1	-1	-1
IREAL	0	0	0	0	0
ISEG	0	0	0	0	0
ISLIP	0	0	0	0	0
ISMTH	0	0	0	0	0
ISPLIN	0	0	0	0	0
ISTEP	0	0	0	0	0
ISTORE	0100	0100	0100	0100	0100
ISTRCH	1	1	1	1	1
KPRT	19	19	19	19	19
LADD	4	4	4	4	4
LAMIN	-1	-1	-1	0	0
LBLP	090	090	090	090	090
METHOD	0	0	0	0	0
METRC	0	0	0	0	0
MOMENT	0	0	0	0	0
NCNBR	0	0	0	0	0
NPOINT	0	0	0	0	0
NPRTBB	050	050	050	050	050
NPRTBL	050	050	050	050	050
NPRTFF	100	100	100	100	100
NPRTSL	050	050	050	050	050
NXPRT	0	0	0	0	0

Table B.4 contains the real input variables used for the marching solution input file OGIVIN.

Table B.4. Real Input Variables for OGIVIN

VARIABLE	T/C #1	T/C #2	T/C #3	T/C #4	T/C #5
ZOB	0.0	0.0	0.0	0.0	0.0
X	0.0	0.0	0.0	0.0	0.0
DX	0.01	0.01	0.01	0.01	0.01
CNBR	0.0	0.0	0.0	0.0	0.0
XEND	15.0	15.0	15.0	15.0	15.0
DS	+0.00005	+0.00005	+0.00001	+0.00001	+0.00001
SMU	0.10	0.10	0.10	0.10	0.10
SMUIM	0.20	0.20	0.20	0.20	0.20
EPSA	0.30	0.30	0.30	0.30	0.30
EPSB	0.30	0.30	0.30	0.30	0.30
ALPHA	0.0	0.0	0.0	0.0	0.0
BETA	0.0	0.0	0.0	0.0	0.0
FSMACH	5.76	5.78	5.79	5.86	5.90
GAMMA	1.4	1.4	1.4	1.4	1.4
RE	133333.3	387500.0	883333.3	1750000.	2541667.
TINF	128.9	128.9	128.9	128.9	128.9
TWALL	560.0	560.0	560.0	560.0	560.0
DQINF	0.0	0.0	0.0	0.0	0.0
XTRANS	0.0	0.0	9.3	0.0	0.0
PER	0.5	0.5	0.5	0.5	0.5
PERMIN	0.0	0.0	0.0	0.0	0.0
PERMAX	0.0	0.0	0.0	0.0	0.0
DSYPLUS	0.0	0.0	0.0	0.0	0.0
CHI1	00.0	00.0	00.0	00.0	00.0
CHI2	00.0	00.0	00.0	00.0	00.0
AOVERB	0.0	0.0	0.0	0.0	0.0
SIGMA	23.0910	23.0910	23.0910	23.0910	23.0910
XOB	00.000	00.000	00.000	00.000	00.000
XOS	00.000	00.000	00.000	00.000	00.000
AB	0.0	0.0	0.0	0.0	0.0
ALENGT	00.0	00.0	00.0	00.0	00.0
DIAB	0.0	0.0	0.0	0.0	0.0
SAX	0.0	0.0	0.0	0.0	0.0
SN	0.0	0.0	0.0	0.0	0.0
SS	0.0	0.0	0.0	0.0	0.0
SMPP	0.0	0.0	0.0	0.0	0.0
SMR	0.0	0.0	0.0	0.0	0.0
SMY	0.0	0.0	0.0	0.0	0.0
XCG	0.0	0.0	0.0	0.0	0.0
XREF	0.0	0.0	0.0	0.0	0.0

Input variables from groups 6 and 7:

Group 6. Output Parameters

IPRT	Starting solution output option
KPRT	Increments the printing of circumferential rays
NXPRT	Axial printout option
NPRTBB	Frequency of printout for body and outer boundary
NPRTBL	Frequency of printout for boundary layer
NPRTFF	Frequency of printout for flow field
NPRTSL	Frequency of printout for sonic layer
ISTORE	Flow field storage to TAPE4
IFORM	Flow field output format option

Group 7. Force and Moment Parameters

MOMENT	Force and moment option
AB	Initial surface area
ALENGT	Reference length to calculate static margin
DIAB	Reference body diameter
SAX	Initial axial force
SN	Initial normal force
SS	Initial side force
SMPP	Initial pitching moment
SMR	Initial rolling moment
SMY	Initial yawing moment
XCG	Axial location of center of gravity
XREF	Axial location of moment reference

APPENDIX C. SURFACE PRESSURE RATIO AND STANTON NUMBER DATA

The following tables contain the results of the comparisons between the PNS predictions and the experimental data for test conditions #1, #3 and #4.

Table C.1. Surface Pressure Ratio Error Band - T/C #1

Pressure Tap #	Experimental Data (Error Band)	PNS Code
1	5.867 - 7.734	7.676
2	5.091 - 6.711	6.594
3	4.285 - 5.647	5.642
4	3.518 - 4.637	4.739
5	3.024 - 3.985	3.762
6	2.732 - 3.602	3.175
7	2.107 - 2.777	2.672
8	1.925 - 2.537	2.242
9	1.291 - 1.701	1.876
10	1.462 - 1.927	1.568
11	0.988 - 1.302	1.310
12	1.159 - 1.528	1.094
13	0.977 - 1.288	0.935
14	1.028 - 1.355	0.859
15	0.876 - 1.155	0.839
16	0.947 - 1.248	0.834
17	0.635 - 0.836	0.833
18	0.816 - 1.076	0.834
19	0.595 - 0.785	0.836
20	0.867 - 1.142	0.838
21	0.968 - 1.275	0.841
22	0.917 - 1.208	0.843
23	0.886 - 1.169	0.845

Table C.2. Surface Pressure Ratio Error Band - T/C #3

Pressure Tap #	Experimental Data (Error Band)	PNS Code
1	6.058 - 6.799	7.718
2	5.219 - 5.858	6.632
3	4.368 - 4.903	5.673
4	3.753 - 4.212	4.711
5	3.193 - 3.584	3.776
6	2.672 - 2.998	3.183
7	2.236 - 2.509	2.674
8	1.884 - 2.115	2.241
9	1.521 - 1.708	1.873
10	1.306 - 1.465	1.563
11	1.053 - 1.181	1.302
12	0.899 - 1.010	1.084
13	0.772 - 0.866	0.930
14	0.752 - 0.844	0.861
15	0.738 - 0.829	0.842
16	0.743 - 0.833	0.834
17	0.730 - 0.819	0.833
18	0.737 - 0.827	0.835
19	0.684 - 0.768	0.837
20	0.735 - 0.825	0.840
21	0.778 - 0.874	0.843
22	0.778 - 0.874	0.846
23	0.782 - 0.877	0.849

Table C.3. Surface Pressure Ratio Error Band - T/C #4

Pressure Tap #	Experimental Data (Error Band)	PNS Code
1	6.403 - 6.841	7.855
2	5.582 - 5.964	6.743
3	4.627 - 4.944	5.761
4	3.851 - 4.115	4.811
5	3.341 - 3.569	3.819
6	2.807 - 2.999	3.213
7	2.316 - 2.475	2.692
8	1.933 - 2.065	2.250
9	1.587 - 1.696	1.875
10	1.346 - 1.439	1.559
11	1.122 - 1.198	1.295
12	0.924 - 0.987	1.075
13	0.780 - 0.834	0.920
14	0.749 - 0.800	0.852
15	0.727 - 0.776	0.835
16	0.725 - 0.775	0.830
17	0.804 - 0.859	0.830
18	0.722 - 0.772	0.833
19	0.719 - 0.768	0.836
20	0.743 - 0.794	0.838
21	0.758 - 0.809	0.842
22	0.754 - 0.806	0.844
23	0.756 - 0.808	0.847

The following tables present the results of the comparison between the PNS predictions and the experimental data for the local Stanton number for test conditions #1, #3 and #4. In each table, the experimental data is given in terms of its error band.

Table C.4. Stanton Number Error Band - T/C #1

Coax Gauge #	Experimental Data St # (x 1000)	PNS Code St # (x1000)
1	0.285 - 0.393	0.142
2	0.246 - 0.339	0.203
3	0.227 - 0.314	0.241
4	0.221 - 0.305	0.257
5	0.211 - 0.291	0.265
6	0.202 - 0.278	0.268

Table C.5. Stanton Number Error Band - T/C #3

Coax Gauge #	Experimental Data St # (x 1000)	PNS Code St # (x1000)
1	0.105 - 0.128	0.059
2	0.088 - 0.108	0.096
3	0.086 - 0.105	0.111
4	0.092 - 0.112	0.126
5	0.143 - 0.175	0.173
6	0.282 - 0.344	0.233

Table C.6. Stanton Number Error Band - T/C #4

Coax Gauge #	Experimental Data St # (x 1000)	PNS Code St # (x1000)
1	0.450 - 0.536	0.339
2	0.421 - 0.502	0.319
3	0.407 - 0.485	0.320
4	0.403 - 0.481	0.321
5	0.393 - 0.468	0.322
6	0.386 - 0.460	0.322

VITA

Captain Richard H. Byers was born on 30 May 1958 in Galliano, Louisiana. He graduated from Viola High School in Viola, Arkansas in 1976, and enlisted in the USAF the same year. He attended Auburn University from which he received a degree of Bachelor of Aerospace Engineering in March 1984. Upon graduation from OTS, he received his Air Force commission and was assigned to the Munitions Division of the AF Armament Laboratory, Eglin AFB, Florida. He served as an exterior ballistician responsible for the development of ammunition for 9mm handguns through 105mm cannons. Later, he was chosen to manage the development of non-electric, hypervelocity launchers within the Strategic Defense Initiative's Hypervelocity Launcher Complex. He entered the School of Engineering, Air Force Institute of Technology, in May 1989.

Permanent Address: HCR 69 Box 15
Gepp, Arkansas 72538

REPORT DOCUMENTATION PAGE

Form Approved
OMB No 0704-0188

1. AGENCY USE ONLY (Leave blank)	2. REPORT DATE	3. REPORT TYPE AND DATES COVERED
	December 1990	Master's Thesis

4. TITLE AND SUBTITLE
Skin Friction and Heat Transfer Predictions for Hypersonic Turbulent Flow Over an Ogive-Cylinder

5. FUNDING NUMBERS

6. AUTHOR(S)
Richard H. Byers, Captain, USAF

7. PERFORMING ORGANIZATION NAME(S) AND ADDRESS(ES)
Air Force Institute of Technology
WPAFB OH 45433-6583

8. PERFORMING ORGANIZATION REPORT NUMBER
AFIT/GAE/ENY/90D-4

9. SPONSORING/MONITORING AGENCY NAME(S) AND ADDRESS(ES)
WRDC/FIMG
WPAFB OH 45433

10. SPONSORING/MONITORING AGENCY REPORT NUMBER
WRDC-TM-90-335-FIMG

11. SUPPLEMENTARY NOTES

12a. DISTRIBUTION/AVAILABILITY STATEMENT
Approved for public release; distribution unlimited

12b. DISTRIBUTION CODE

13. ABSTRACT (Maximum 200 words)

The WRDC/FIMG Parabolized Navier-Stokes (PNS) Code is used to numerically predict both laminar and turbulent hypersonic flows over an ogive-cylinder body at zero angle of attack. A parametric study is conducted to determine the effects of selected code input variables on heat transfer and skin friction predictions. Comparisons are made between the PNS predictions and experimental data from the WRDC/Mach 6 High Reynolds Number Test Facility. Various problems encountered while obtaining PNS starting and marching solutions and corrective steps taken are discussed. A mesh resolution study indicates the minimum radial grid density sufficient for obtaining reasonable heat transfer results. As expected, surface property characteristics are shown to be sensitive to the placement of the first radial grid point away from the surface. Predicted values for surface pressure ratios, local Stanton numbers and local skin friction coefficients are compared with experimental data along the body for laminar through fully developed turbulent flows. Good agreement between the predictions and the experimental data is shown for all flow conditions.

14. SUBJECT TERMS	15. NUMBER OF PAGES
PNS Code, Hypersonic flow, Ogive-Cylinder Body, Heat Transfer, Skin Friction Prediction	135
	16. PRICE CODE

17. SECURITY CLASSIFICATION OF REPORT	18. SECURITY CLASSIFICATION OF THIS PAGE	19. SECURITY CLASSIFICATION OF ABSTRACT	20. LIMITATION OF ABSTRACT
Unclassified	Unclassified	Unclassified	UL